University of Southampton

Faculty of Physical Sciences and Engineering

Optoelectronics Research Centre

Nonlinear, Sensing and Switching Functionalities of Nano-optomechanical Metamaterials

by

Dimitrios Papas

Thesis for the degree of Doctor of Philosophy

March 2022

University of Southampton

Abstract

Faculty of Physical Sciences and Engineering

Optoelectronics Research Centre

Doctor of Philosophy

Nonlinear, Sensing and Switching Functionalities of Nano-optomechanical Metamaterials

by

Dimitrios Papas

This Thesis reports on the study of hybrid nano-optomechanical metamaterials, and their sensing, nonlinear and switching functionalities.

- I have constructed a dedicated apparatus for optical measurements of photonic metamaterials in vacuum during acoustic excitation. It is based on a fiberized inverted microscope setup operating at the wavelength of 1310 nm in both reflection and transmission modes.
- I have provided the first observation of fluctuations of optical properties of metamaterials due to thermal motion. In a plasmonic nanomechanical metamaterial thermal motion of mechanical components with an amplitude of a few hundreds of picometers leads to reflectivity fluctuations of the order of 0.1%.
- I have demonstrated the first tuning of mechanical eigenfrequencies of plasmonic nanomechanical metamaterials with light. Controlling the internal stress of the structure via light illumination allows tuning of the mechanical frequencies at which it can be efficiently driven. Eigenfrequency shifts of up to 19.5 % are measured for 7 μW of incident optical power.
- I have developed the first nanomechanical, metamaterial-based nanobolometer. Non-contact optical detection of infrared radiation is based on the detection of light scattered by two optically coupled nanomechanical beams providing spatial resolution of 400 nm, eigenfrequency shift per unit of incident optical power (responsivity) of 2-3%/μW with a noise equivalent power of 3-5 nW/Hz$^{1/2}$.
- I have demonstrated a new type of volatile optical bistability in a resonant hybrid nano-optomechanical device. The bistable function has been demonstrated on a pair of anchored beams decorated with plasmonic metamolecules. The nonlinearity resides in the mechanical properties of the beams that can be driven to a bistable response by acoustic signals modulated at their natural mechanical resonances. Optical switching between the two mechanically stable states is demonstrated with 6 μW of incident optical power and the bistable states are sustained and controllable by about a pW of mechanical power delivered to a beam.

Overall, hybridization of mechanically and optically resonant structures can provide sensing and switching functionalities based on their mechanical properties and nonlinear response.

Table of Contents

Table of Contents ..... **i**

Table of Tables ..... **v**

Table of Figures ..... **vii**

List of Accompanying Materials ..... **xi**

Research Thesis: Declaration of Authorship ..... **xiii**

Acknowledgements ..... **xv**

Chapter 1 Introduction **1**

1.1 Nanophotonic metamaterials 2

1.2 Reconfigurable nanophotonic metamaterials 4

1.2.1 Hybridization with functional materials 4

1.2.2 Mechanically reconfigurable metamaterials 6

1.3 Optical detection of thermal motion 14

1.4 Thesis overview 16

Chapter 2 Mechanics of nanomechanical metamaterials **19**

2.1 The Euler-Bernoulli beam model 19

2.1.1 Mechanical resonances of doubly-clamped beams 20

2.1.2 Mechanical resonances of doubly-clamped beams under tensile stress 21

2.2 Mechanical analysis of metamaterial beams 22

2.3 Thermal motion in nanomechanical structures 25

2.3.1 Power spectral density 26

2.3.2 Effective mass 27

2.4 Conclusions 28

Chapter 3 Detection of thermal motion in nanomechanical plasmonic metamaterials **31**

3.1 Experimental setup 32

3.2 Fabrication of nanomechanical metamaterials 34

3.3 Modulation of optical properties of nanomechanical metamaterials due to thermal motion 36
3.3.1 Optical properties of nanomechanical metamaterials 38
3.3.2 Detection of thermal motion in nanomechanical metamaterials 41
3.4 Conclusions 44

Chapter 4 Photothermal tuning of nanomechanical plasmonic metamaterials 45

4.1 Thermal tuning of mechanical eigenfrequencies 46
4.2 Metamaterial optical properties 48
4.3 Sample and effective material parameters 49
4.4 Tuning of mechanical resonances of metamaterial beams with light 51
4.4.1 Temperature increase in the beams 53
4.4.2 Tuning of eigenfrequencies by ambient temperature changes 55
4.5 Optomechanical metamaterial nanobolometer 56
4.6 Frequency tuning in a metamaterial array 58
4.7 Conclusions 61

Chapter 5 Bistable nanomechanical metamaterials 63

5.1 Bistability in MEMS/NEMS 64
5.1.1 Bistability due to geometric nonlinearity 65
5.2 Concept of bistable metamaterial 67
5.3 Experimental details 68
5.3.1 Metamaterial excitation and experimental setup 68
5.3.2 Design of freestanding membranes for nonlinear metamaterials 69
5.4 Bistability in nanomechanical metamaterials 71
5.4.1 Acoustically controlled bistability 73
5.4.2 Optically controlled bistability 78
5.4.3 Dynamics of optical switching 81
5.5 Membrane-based bistability 84
5.6 Conclusions 89

Chapter 6 Conclusions 91

6.1 Summary 91
6.2 Outlook 92

Appendix A Focused ion beam milling 95
Appendix B Microspectrophotometer 97
Appendix C Publications 99
Bibliography 103

Table of Tables

Table 2.1 Mechanical properties of silicon nitride and gold.....23

Table 3.1 Fundamental mechanical eigenfrequencies and effective masses of the plasmonic metamaterial without tensile stress. 43

Table 4.1 Thermal properties of silicon nitride and gold. 51

Table 4.2 Effective Young's modulus E_{eff}, density ρ_{eff}, thickness t_{eff}, thermal expansion coefficient α_{eff} and mass $\mathrm{m}_{\mathrm{eff}}$ of the two metamaterial beams. 51

Table 5.1 Calculated mechanical eigenfrequencies of a 100 µm x 100 µm membrane consisting of a 50 nm-thick silicon nitride coated with 50 nm-thick gold. 86

Table of Figures

Figure 1.1 The split ring resonator. 3

Figure 1.2 Reconfigurable, phase change-based metamaterials. 5

Figure 1.3 Reconfigurable, liquid crystal-based metamaterials. 6

Figure 1.4 Stretchable metamaterials. 7

Figure 1.5 Thermally actuated nanomechanical metamaterials. 9

Figure 1.6 Electric and magnetic control of nanomechanical metamaterials. 11

Figure 1.7 Optically reconfigurable nanomechanical metamaterials. 13

Figure 1.8 Nanomechanical addressable metamaterials. 14

Figure 1.9 Detection of thermal motion of a plasmonic nanomechanical system. 15

Figure 2.1 Schematic illustration of a uniform, doubly-clamped beam. 20

Figure 2.2 Stress dependence of mechanical eigenfrequencies. 23

Figure 2.3 Schematic representation of the simulated nanomechanical metamaterial beams. 24

Figure 2.4 Simulated mechanical modes of the nanomechanical metamaterial beams. 24

Figure 3.1 Schematic of the experimental setup for thermal motion detection of nanomechanical metamaterials. 33

Figure 3.2 Photographs of the experimental setup for thermal motion detection. 33

Figure 3.3 Schematic illustration of the fabrication procedure. 34

Figure 3.4 Fabrication and characterization of nanomechanical metamaterials. 35

Figure 3.5 Unsuccessful fabrication attempts. 36

Figure 3.6 Thermal fluctuations of optical properties of a nanomechanical metamaterial. 37

Figure 3.7 Plasmonic nanomechanical metamaterial. 39

Figure 3.8 Optical properties and displacement sensitivity of the nanomechanical metamaterial. 40

Figure 3.9 PSD spectrum of the nanomechanical metamaterial. 41

Figure 3.10 Thermal fluctuation of the reflectivity of the nanomechanical metamaterial. 42

Figure 4.1 Concept of thermal tuning of mechanical eigenfrequencies. 46

Figure 4.2 Optical properties of the double beam optical nano-mechanical system..... 49

Figure 4.3 Stress-tuning of nanomechanical beam resonators. 50

Figure 4.4 Power dependence of thermal vibrations of the metamaterial beam pair. 52

Figure 4.5 Optical control of mechanical resonances and stress. 53

Figure 4.6 Temperature and quality factors of the metamaterial beams. 54

Figure 4.7 Ambient temperature control of mechanical resonances. 55

Figure 4.8 Polarization and spectral dependence of absorption of the metamaterial unit cell.56

Figure 4.9 Concept of frequency tuning and bolometry in a metamaterial array..... 58

Figure 4.10 Nanomechanical metamaterial bolometer array. 60

Figure 5.1 Schematic illustration of a bent, doubly-clamped beam. 65

Figure 5.2 Membrane-based nanomechanical metamaterial for mechanical memory. 67

Figure 5.3 The piezoelectric chip used to drive the nanomechanical metamaterial..... 69

Figure 5.4 Experimental setup for bistability measurements. 69

Figure 5.5 Finalized Norcada design for rectangular membrane windows. 70

Figure 5.6 Silicon frame supporting rectangular silicon nitride membranes..... 70

Figure 5.7 Fabrication results on rectangular membrane windows. 71

Figure 5.8 Metamaterial based nanomechanical system for detection of nonlinear and bistable response. 72

Figure 5.9 Calibration procedure for optical property modulation measurements..... 73

Figure 5.10 Nonlinearity and acoustically controlled bistability of light scattered by the metamaterial beams. 75

Figure 5.11 Impedance measurement of the piezoelectric element. 76

Figure 5.12 Light modulation by metamaterial beams at different illumination power levels.77

Figure 5.13 Optical control of the hysteresis cycle. 78

Figure 5.14 Optically induced nanomechanical bistability. 79

Figure 5.15 Back and forward scattered light hysteresis curves. 80

Figure 5.16 Back scattered light hysteresis cycles obtained at different fixed acoustic frequencies. 82

Figure 5.17 Back scattered light hysteresis cycles obtained for fixed acoustic frequency of 2 MHz and increasing laser modulation frequency. 83

Figure 5.18 Metamaterial array for bistability experiments. 84

Figure 5.19 Optical detection of the metamaterial array's mechanical resonances. 85

Figure 5.20 Modulation of optical properties of the membrane-metamaterial system under piezoelectric drive. 87

Figure 5.21 Nonlinear response and bistability of the membrane-metamaterial system. 88

List of Accompanying Materials

The research data presented in this Thesis can be found as:

D. Papas (2021), Dataset for Nonlinear, Sensing and Switching Functionalities of Nano-optomechanical Metamaterials. DOI: 10.5258/SOTON/D2070

Research Thesis: Declaration of Authorship

Print name: Dimitrios Papas

Title of thesis: Nonlinear, Sensing and Switching Functionalities of Nano-optomechanical Metamaterials

I declare that this thesis and the work presented in it are my own and has been generated by me as the result of my own original research.

I confirm that:

1. This work was done wholly or mainly while in candidature for a research degree at this University;
2. Where any part of this thesis has previously been submitted for a degree or any other qualification at this University or any other institution, this has been clearly stated;
3. Where I have consulted the published work of others, this is always clearly attributed;
4. Where I have quoted from the work of others, the source is always given. With the exception of such quotations, this thesis is entirely my own work;
5. I have acknowledged all main sources of help;
6. Where the thesis is based on work done by myself jointly with others, I have made clear exactly what was done by others and what I have contributed myself;
7. Parts of this work have been published as journal papers and conference contributions listed in Appendix C.

Signature: ..... Date: 21/3/2022

Acknowledgements

First of all I would like to thank my supervisors, Professor Nikolay Zheludev, Dr. Eric Plum and Dr. Jun-Yu Ou for their guidance and support during my studies. Prof. Zheludev for giving me the opportunity to work on such an exciting research topic and always pushing me to do better. Dr. Plum for his constant, unwavering support and valuable insights into many aspects of my research, his advice really helped me in establishing a more critical thinking of my work. Dr. Ou for his training, fruitful discussions and for teaching me everything I now know about an optics lab. His expertise was vital to the successful completion of my experiments.

I further acknowledge my collaborators and friends, Jinxiang Li and Tongjun Liu for our collaboration and discussions not only in the office and in the labs but during trips and in the pubs as well. Our exchanges of ideas were a huge motivation for me.

I would like to thank all the people of the Nanophotonics and Metamaterials group for their help during my studies and the great time we had during these four years. Particularly my colleagues and friends, Apostolos Zdagkas, Hao Li and Jie Xu. Moreover, I want to thank Dr. Oleksandr Buchnev for training me in the use of focused ion beam milling. I also want to thank all the staff at the ORC for their help. Mostly, Neil Sessions for his cleanroom training and Glen Topley.

Finally, I would like to thank the people that supported me during my stay in a foreign country. First of all, my partner Maria for supporting me and putting up with me spending long hours in the lab or in front of my computer screen. Without her emotional support I would not have made it this far. I am also grateful to my family and particularly to my sister Sophia who made my staying far from home much more joyous.

Chapter 1

Introduction

The study of light and its interaction with matter has revolutionized modern societies. Nowadays photonic and optoelectronic technologies underpin an ever increasing number of technological advancements spanning numerous disciplines from telecommunications and medicine to manufacturing and metrology. Some of the most notable being optical fibre telecommunications, the basis of the Internet, and optical data storage that now form a part of everyday life. More recently, advances in the fields of artificial intelligence and programmable photonics aim to overcome limitations of current electronics-based technologies such as operational speed and energy consumption.

In order for optics-based technologies to compete with their electronic counterparts miniaturization and compactness of the devices is crucial. Advances in nanofabrication technologies have made it possible to structure matter in the nanoscale which has led to the emergence of fields such as optomechanics, plasmonics and metamaterials.

The field of metamaterials has greatly benefited from such advances. Initially studied in the microwave regime, metamaterials quickly led to the demonstration of novel physical phenomena that could not be attained by conventional optical media. Soon after, intensive research was focused on scaling down dimensions to access the optical part of the spectrum. Nowadays, metamaterials can be utilized to obtain a number of functionalities across the electromagnetic spectrum ranging from simpler functions, such as intensity modulation, to more complex operations of light manipulation e.g. beam steering, focusing.

Scaling down the dimensions of microelectromechanical systems (MEMS) has also led to the emergence of nanoelectromechanical systems (NEMS) with geometric characteristics ranging from few to hundreds of nanometres. This allows access to operational frequencies potentially in the GHz range while providing very high quality factor resonances and low masses that are being exploited for a number of sensing applications such as mass, temperature and force sensing.

Combination of mechanically tunable and resonant elements with optically resonant structures such as photonic metamaterials aims to introduce structural tunability over metamaterials and their optical properties.

1.1 Nanophotonic metamaterials

The term “metamaterials”, from the Greek word meta (μετά) meaning “after”, was coined at the turn of the millennium in order to describe the behaviour of a new range of composites [1]. Metamaterials can be described as composite, artificial media exhibiting properties not found in natural materials. While the electromagnetic properties of natural materials are derived from their molecular structure, metamaterial properties result from their structuring on a sub-wavelength scale. Thus, an artificial structure can be called a metamaterial as long as the dimensions of the unit cell, called the “metamolecule”, are smaller than the wavelength it interacts with. Then the impinging electromagnetic wave interacts with a homogeneous effective medium for which effective material properties can be determined [2]. These can then be tailored by adjusting the dimensions and constituent materials of the metamaterial’s building blocks.

In 1968 Victor Veselago was the first to theoretically describe a medium with simultaneously negative values of permittivity ε and permeability μ and showed that such a medium should have a negative refractive index [3]. The first experimental demonstration of a metamaterial with simultaneously negative ε and μ was realized in 2000 for the microwave regime [4] and negative refraction was demonstrated experimentally a year later [5]. These results along with the works of Pendry on superlensing [6] and light bending [7] through transformation optics sparked intensive metamaterial research and very quickly research focused on demonstrating such phenomena at optical frequencies.

The split-ring resonator (SRR) is perhaps the most iconic metamolecule so far, owing to its initial suggestion by Pendry [8] and the subsequent experimental realization in the microwave regime [4, 5]. In its simplest form, it consists of a metallic ring structure with a gap (Figure 1.1 (a)). Such a structure acts as an LC circuit with the gap playing the role of the capacitor and the metallic part forming the inductor (Figure 1.1 (b)). Therefore, it acts as an LC oscillator with a resonance frequency [2, 9]:

$$\omega = 1/\sqrt{LC} \tag{1.1}$$

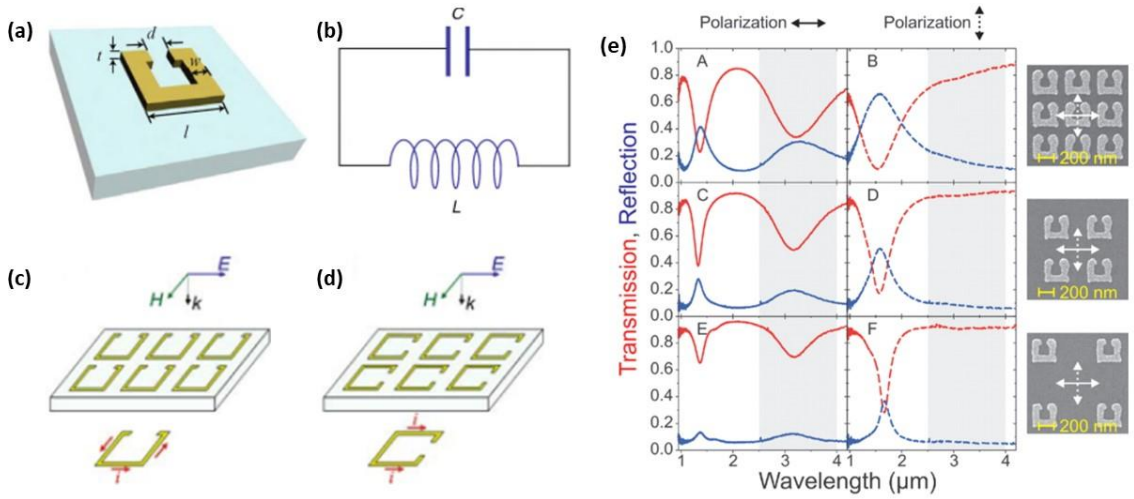

Figure 1.1 The split ring resonator. (a) A split-ring resonator metamolecule [2]. (b) Equivalent LC circuit [2]. (c,d) An SRR array excited by a normally incident electromagnetic field with the electric field polarized (c) parallel and (d) perpendicular to the gap [2]. (e) Experimentally measured transmission and reflection spectra of SRR arrays of different periodicity and for both polarization directions. For light polarized parallel to the ring gap, an LC resonance appears in the spectra at a wavelength of around 3μm. When the polarization direction is rotated by 90 degrees, the resonance disappears [9].

The values of inductance and capacitance are determined by the geometric parameters. When a planar array of such metamolecules is excited by a normally incident electromagnetic wave with the electric field polarized parallel to the gap (Figure 1.1 (c)), due to the asymmetry of the structure, an asymmetric current mode is supported that gives rise to a magnetic dipole oriented perpendicular to the metamaterial plane. In the case that the polarization is normal to the gap (Figure 1.1 (d)), symmetric currents are excited that give rise to an electric dipole (parallel to the currents) but no magnetic dipole. This was experimentally demonstrated in 2004 by Linden in the IR part of the spectrum using gold-based SRRs (Figure 1.1 (e)).

The resonant response of such structures will depend on their material properties and moreover, the resonant wavelength will scale with their size [10]. Therefore, miniaturization of metamaterial structures leads to resonant behaviour at shorter wavelengths, with nanostructures having resonances in the optical part of the spectrum. The LC resonant approach works in the low frequency regime (below ~100 THz) where metals have very large permittivity and are considered to be perfect electric conductors [10]. However, at optical frequencies their finite conductivity has to be taken into account. Therefore, the behaviour of metallic sub-wavelength structures is more precisely described by plasmons which are collective oscillations of the free electrons of the material. Plasmonics has significantly impacted metamaterial research and vice versa, however, the performance of plasmonics-based metamaterials is still limited due to ohmic losses of metals and heating. Such effects can be negated by the use of high index dielectric metamaterials [11, 12] that can provide larger quality factor resonances [13].

1.2 Reconfigurable nanophotonic metamaterials

A metamaterial is essentially a collection of optical resonators. As such, its functionality is usually limited to a narrow area of the spectrum. In other words, the bandwidth of metamaterials is normally limited due to the resonant nature of the metamolecules [14]. Therefore, introducing tunability, in an otherwise narrowband metamaterial, can extend the operation range of the device and offer the potential for dynamic control over light on the sub-wavelength scale.

In general, there are two major strategies of obtaining a tunable metamaterial response. One is to change the parameters of the materials constituting the device, thus changing its effective electromagnetic response. This is achieved by using other functional materials in conjunction with the metamaterial array such as phase-change materials and liquid crystals, usually referred to as hybrid metamaterials. The second one is to structurally rearrange the metamolecule array, i.e. change its initial geometric configuration since the optical response depends on characteristics such as unit cell dimensions and spacing. This is particularly effective in coupled metamolecules where the unit cell consists of more than one element in proximity.

1.2.1 Hybridization with functional materials

Initial work on tunable metamaterials was carried out in the microwave regime. Mainly, integration of metamaterials with nonlinear electrical elements such as varactor diodes was used to obtain a tunable response by allowing tuning of individual metamolecules [15]. However, such an approach could not be scaled down to the optical spectral range.

Hybridization of metamaterials with other functional materials such as phase-change materials [16-22] and liquid crystals [23-30] has been widely explored as they can provide switching functionalities at optical frequencies. Heat, electrical or even optical signals can be used to initiate phase transitions of materials such as VO_2 [16, 17] between different solid phases, modifying the overall optical response of the hybrid metamaterial structure (Figure 1.2 (a)). $Ge_2Sb_2Te_5$ (GST) chalcogenide glass, a material that has been widely used in optical disk storage applications, has been used to demonstrate an all optically controlled, non-volatile and bidirectional metamaterial [19] (Figure 1.2 (b)). In 2016, Wang et al. demonstrated a platform for writing, erasing and rewriting of photonic structures with light demonstrating planar focusing devices, holograms and a dielectric metamaterial [21] (Figure 1.2 (c)) while all-chalcogenide nano-gratings have also been demonstrated [22] (Figure 1.2 (d)). Gallium [20] and Gallium Lanthanum Sulfide (GLS) [18] based switchable metamaterials have been proposed as well (Figure 1.2 (e)). The main advantage of using phase change materials is that they can provide all-optical control over the metamaterial's properties and non-volatile switching/memory functionalities, i.e. information is stored in the

absence of input energy (signal). Moreover, switching can be fast, with response times in the nanosecond range [31].

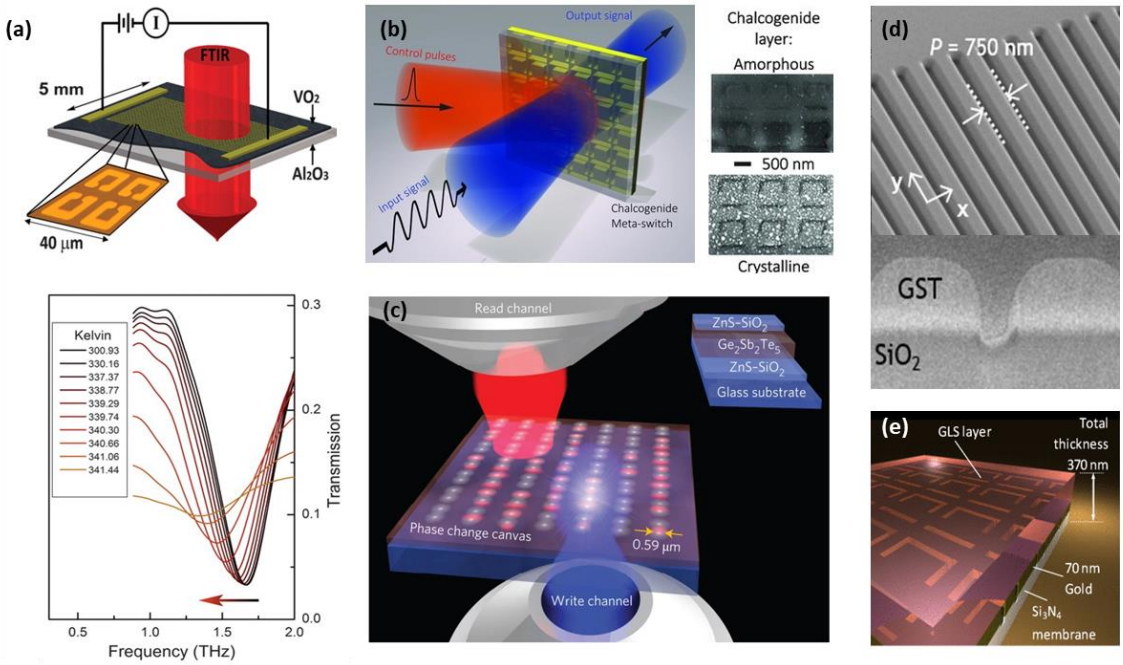

Figure 1.2 Reconfigurable, phase change-based metamaterials. (a) Temperature controlled, gold-based SRR metamaterial array fabricated on top of a VO_2 film operating in the near-IR (top panel). Increase of temperature leads to shifts of the structure's resonance frequency (bottom panel) [17]. (b) Illustration of a non-volatile, all-optically controlled chalcogenide based metamaterial switch of nanoscale thickness. Control pulses are used to convert a thin layer of GST back and forth between its amorphous and crystalline states modifying the transmission and reflection of the structure [19]. (c) Illustration of apparatus used for writing and erasing various optical components, on a thin layer of GST using femtosecond pulses. Lenses, diffractive elements and resonant metamaterials, can be written by modifying the refractive index of the chalcogenide glass [21]. (d) Scanning electron microscope (SEM) image and cross-section of a chalcogenide based nano-grating fabricated on SiO_2 where phase transitions in the GST layer, mediated by laser illumination, change the spectral dispersion of the grating [22]. (e) Illustration of a GLS based electro-optic metamaterial switch on a 100 nm thick silicon nitride membrane [18].

Similarly, hybridization with liquid crystals (LC) can allow electric control of metamaterial properties since liquid crystals are sensitive to external fields and can provide large optical anisotropy. Figure 1.3 (a) illustrates an example of how liquid crystals can be incorporated in a metamaterial based device to provide light modulation and switching functionalities [25]. Here, the authors demonstrated a cell with a layer of nematic LC confined between a V-shaped metamaterial and an indium tin oxide (ITO) layer. Application of voltage results in realignment of the LC molecules which led to fivefold modulation of a transmitted 1550 nm laser beam for 7 volts of applied voltage. Similar schemes can be found in [26] and [27]. Moreover, metamaterials hybridized with LC have been proposed as spatial light modulators (SLM) of subwavelength thickness, for wavefront manipulation by modulating the phase of transmitted light [29, 30] (Figure 1.3 (b)). Compared with phase-change metamaterials, they can be significantly slower since the response time of typical liquid crystals is in the millisecond range [32].

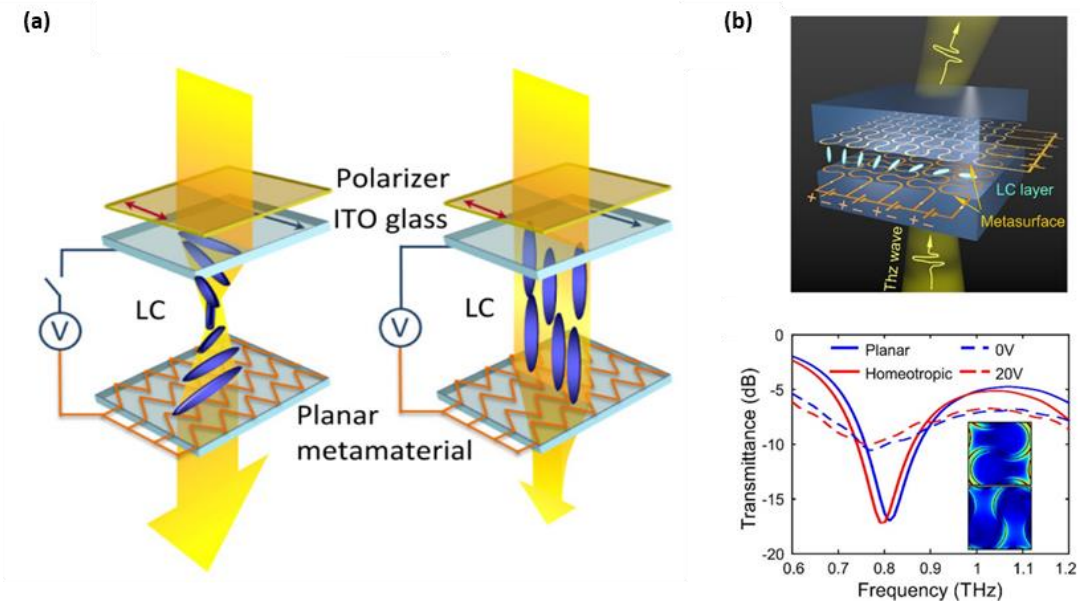

Figure 1.3 Reconfigurable, liquid crystal-based metamaterials. (a) Illustration outlining the design and operation of a liquid crystal cell sandwiched between a planar plasmonic metamaterial at the bottom and a transparent electrode on top. The planar metamaterial plays the role of liquid crystal alignment layer, transparent electrode and polarizer at the same time. On the left, the orientation of the liquid crystals is set by the top and bottom surfaces leading to optical activity. On the right, the application of voltage leads to realignment of the LC so that the incident polarization is not rotated, leading to reduced transmission through the metamaterial structure [25]. (b) The top panel illustrates a hybrid spatial light modulator (SLM) based on two metasurfaces with a layer of LC between them. The meandering pattern of the metasurfaces results in spatially addressable electrodes. The bottom panel shows simulation (solid lines) and measurement (dashed lines) of the SLM's transmission for 0 V (blue) and 20 V (red) of applied voltage [30].

1.2.2 Mechanically reconfigurable metamaterials

Reversible changes of the light-matter interaction of mechanically reconfigurable metamaterials result from repositioning the metamolecules of the arrays, or their components, with respect to each other. A number of tuning schemes have been developed, aiming at controlling the spatial arrangement of the metamolecules at a subwavelength level. In 2009 Lapine et al. suggested an array of parallel plates supporting split rings where laterally displacing every second layer resulted in shifts of its transmission resonance based on the degree of displacement and demonstrated this in the microwave regime [33]. However, with scaling down of the dimensions control over the spatial arrangement of metamolecules becomes increasingly challenging and more sophisticated solutions are needed.

Since the response of a metamaterial depends on geometric characteristics such unit cell dimensions and spacing, perhaps the most straightforward route to obtain tunable optical properties in the IR and visible part of the spectrum is through the use of stretchable substrates (Figure 1.4). In [34] the authors demonstrated the first mechanically reconfigurable optical metamaterial. They fabricated a tunable metamaterial based on various plasmonic split ring designs supported by flexible PDMS substrates, operating in the IR part of the spectrum, where straining of

the substrate by 50% resulted in shifting of the metamaterial's resonant wavelength by 60% (Figure 1.4 (a)). A similar work was reported in [35] based on an array of bow-tie metamolecules supported by a flexible substrate (Figure 1.4 (b)). More recently, in [36] the authors demonstrated dielectric metasurfaces embedded in a PDMS matrix operating at visible wavelengths (Figure 1.4 (c)) and a stretchable plasmonic metasurface operating as a tunable flat lens at 632 nm has also been realized [37] (Figure 1.4 (d)). However, the response of such structures is usually slow and dictated by the elastic properties of the supporting polymer.

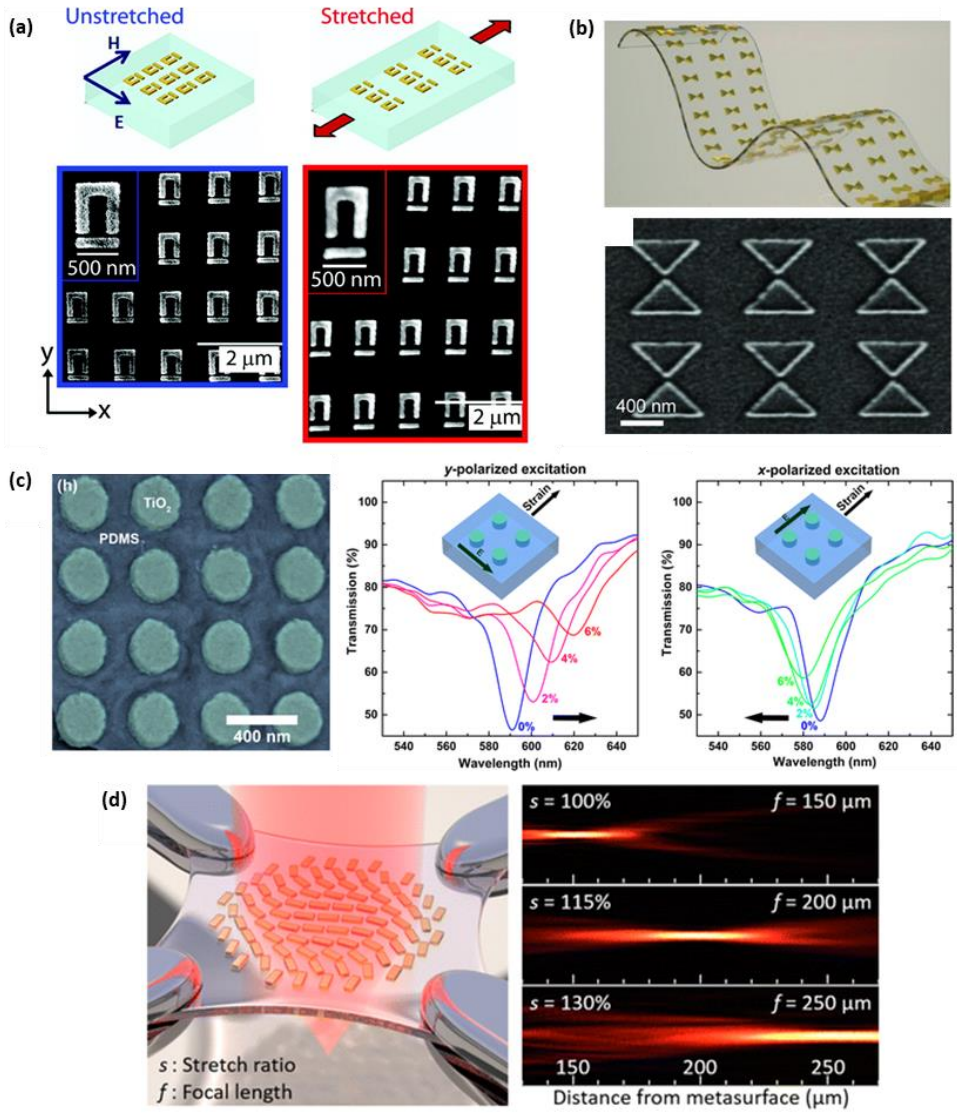

Figure 1.4 Stretchable metamaterials. (a) Gold based metamolecules consisting of a split ring and a horizontal bar supported by a PDMS substrate prior to and after stretching (top panel). Environmental scanning electron microscopy images of the structure before (blue) and after stretching (red) where the gap between the split ring and the bar has increased (bottom panel). (b) Flexible substrate supporting a bow-tie array of gold metamolecules (top panel) and SEM image of the plasmonic bow-tie array (bottom panel) [35]. (c) SEM image of cylindrical TiO_2 dielectric resonators (green) with a diameter of 190 nm and thickness of 102 nm, embedded in an elastomeric matrix (blue) (left panel). Transmission spectra of the dielectric metasurface with increasing applied strain for light polarized perpendicular (central panel) and parallel (right panel) to the direction of the applied strain [36]. (d) Illustration of a tunable plasmonic metasurface consisting of gold nanorods with width of 100 nm, height of 70 nm and different orientation angle modifying the wavefront of transmitted light (left panel). Longitudinal profiles of the transmitted beam for, 100% (unstretched structure), 115% and 130% stretch ratios (right panel). The focal length, f increases from 150 µm up to 250 µm [37].

A promising route of obtaining mechanically reconfigurable optical properties of nanoscale metamaterials is their integration with microelectromechanical (MEMS) and nanoelectromechanical (NEMS) systems. To fabricate such structures, ultra-thin, free-standing dielectric or semiconducting membranes have been widely used due to their high mechanical quality factor and commercial availability. They can support metallic or dielectric films deposited on top and can be patterned to form free-standing metamolecules or strips of them that can be actuated by external stimuli [21].

External control over individual metamolecules, or strips of them can be facilitated by harnessing a number of physical phenomena at the nanoscale. For instance, taking advantage of the different thermal expansion coefficients of different constituting materials, heat actuation of nanomembrane-based nanomechanical metamaterials can be achieved. Tao et al. reported the first mechanically reconfigurable metamaterial operating in the terahertz regime [38]. This was fabricated out of a bilayer silicon nitride (Si_3N_4)/gold (Au) membrane forming an array of cantilever supported split ring resonators that increasingly deformed with rapid thermal annealing (Figure 1.5 (a)). In the optical part of the spectrum, Ou et al. demonstrated a thermally actuated metamaterial consisting of silicon nitride/gold bridges [39]. In their design every second bridge of the array can be deformed when heated due to differential heating expansion, leading to modulated optical properties of the array (Figure 1.5 (b)). More recent works on thermally actuated metamaterials report further functionalization of the structures with materials such as shape-memory alloys [40] and mechanochromic thin films [41]. In [40] Nagasaki et al. used gold covered nickel-titanium (NiTi) alloy nanowires supported by silicon nitride beams where heating and cooling of the device, resulted in a hysteretic transition between two solid phases of the NiTi alloy, demonstrating a rewritable memory functionality (Figure 1.5 (c)). Karvounis et al., taking advantage of differential thermal expansion of different materials, demonstrated a mechanochromic reconfigurable metamaterial where strain-induced refractive index changes of a thin molybdenum disulphide (MoS_2) layer on top of the structure resulted in more than 190 % relative transmission change for a strain level of 2% (Figure 1.5 (d)) [41]. However, the reaction time of such structures will depend on their conductive cooling timescale, usually at tens of microseconds, but more importantly, the rate at which the ambient temperature can be changed [21]. Tuning through resistive heating as demonstrated in [42] can result in faster response times down to 10 μs dictated only by the conductive cooling of the nanostructure.

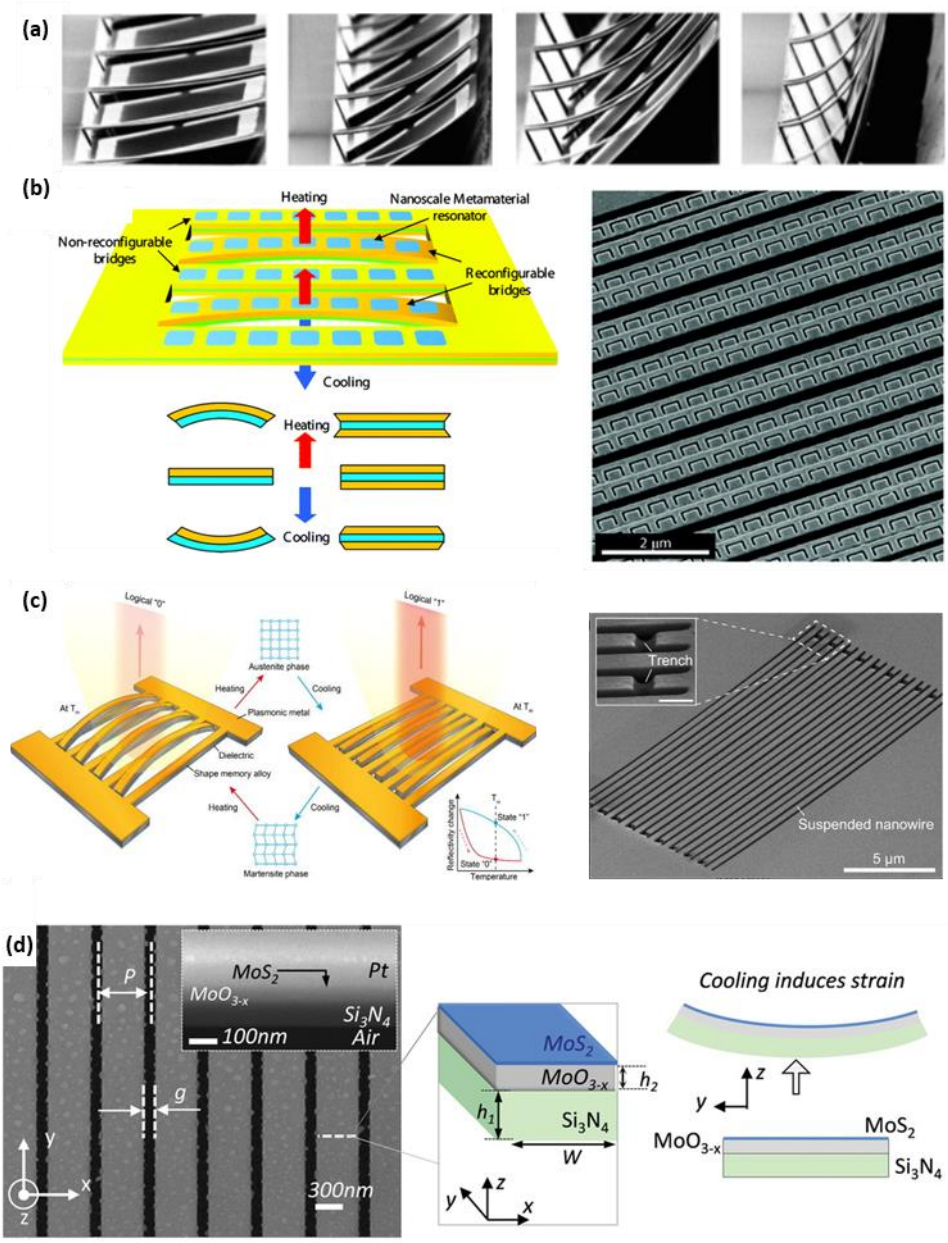

Figure 1.5 Thermally actuated nanomechanical metamaterials. (a) Thermally actuated terahertz metamaterial [38]. (b) The left panel illustrates the working principle of a thermally reconfigurable nanomechanical metamaterial. The structure consists of alternating bridges consisting of Si_3N_4 (blue)/Au (yellow) (reconfigurable beams) and Au/Si_3N_4/Au (non-reconfigurable beams). Due to the larger thermal expansion coefficient of gold, the reconfigurable beams bend upon heating and cooling of the device resulting in modulated optical properties. The right panel shows an SEM image of the fabricated free-standing metamaterial [39]. (c) Shape memory nanomechanical metamaterial. For a given temperature, the structure supports two stable mechanical configurations depending on the phase of the NiTi alloy (martensite or austenite phase). Trenches cut at the edges of every second beam (see right panel) allow for increased deformation upon temperature variations changing the structure's plasmonic response [40]. (d) SEM image of a mechanochromic reconfigurable nanomechanical metamaterial consisting of 22 μm long, 400 nm wide (W), 90 nm thick (h_1) Si_3N_4 beams supporting 60 nm (h_2) of molybdenum oxide (MoO_{3-x}) with a thin layer of 6 nm of MoS_2 on top. P: 500 nm, gap between beams, g: 100 nm (left panel). Strain induced in the beams upon cooling of the nanostructure leads to deformation due to a large thermal expansion mismatch between Si_3N_4 and MoO_{3-x} (right panel). This deformation leads to a stress-induced modification of the MoS_2 layer's optical properties. [41].

The reduced physical dimensions of such membrane-based metamaterial systems also leads to increased electromagnetic interactions between the constituent elements that can overcome the elastic response of the supporting membrane [21]. Therefore, electrostatic, magnetic and

optical forces can be harnessed to provide control over (rows of) metamolecules providing faster switching rates of up to hundreds of MHz.

Electrostatic and magnetic actuation can be realized by engaging the Coulomb and Lorentz force, respectively. Electro-optic modulation through field induced displacements can be realized by voltage application across the constituent beams of a metamaterial array. Attractive or repulsive Coulomb forces between neighbouring beams cause beam displacements that change the field distribution around the metamolecules. Similarly, a magneto-electro-optical effect can be observed in the presence of a magnetic field, where current-bearing nanowires are subject to the Lorentz force that can be used for out-of-plane displacement of the metamaterial beams. The first electrostatically actuated membrane-based optical nanomechanical metamaterial was demonstrated by Ou et al. [43] (Figure 1.6 (a)). Their structure consisted of alternating wire and meander patterns fabricated from a gold covered silicon nitride membrane, where beams with tapered ends allow for increased flexibility. By applying voltage across the device terminals, attractive Coulomb forces arising from opposite charges in the wires modified the initial gap separating them (125 nm, in the OFF state) thus tuning the plasmonic response and achieving up to 8% relative reflection change at wavelengths around 1500 nm. Similarly, deformation of dielectric metamaterial beams has been demonstrated via the phenomenon of electrostriction i.e. the deformation of dielectric materials under the application of an electric field [44], see Figure 1.6 (b). Static, in-plane deformation of the metamaterial beams led to 7% relative transmission change around 1500 nm for an applied voltage of 2 volts. Moreover, dynamic modulation of the applied field, leading to in-plane oscillations of the beam structures, reached 3.5 % relative transmission modulation at a frequency of 6 MHz and 500 mV driving amplitude. An issue with in-plane motion outlined in both aforementioned works is the irreversible switching that occurs when the beams get too close. For large enough bias, the attractive electrostatic forces overcome the elastic restoring force, the gap between adjacent nanostructures closes and remains so due to van der Waals forces. This results in profound but irreversible changes of the structures' optical properties, see right panel of Figure 1.6 (b). Magnetic actuation of similarly designed nanomechanical structures can be used to induce out-of-plane displacement of the metamaterial nanowires by engaging the Lorentz force (Figure 1.6 (c)). In their works [42, 45], Valente et al. used a plasmonic nanomechanical metamaterial, based on V-shaped nanowires cut from a gold-coated silicon nitride membrane of 100 nm thickness. Currents flowing through every second nanowire modulate the structure's optical properties due to deformation caused by thermal

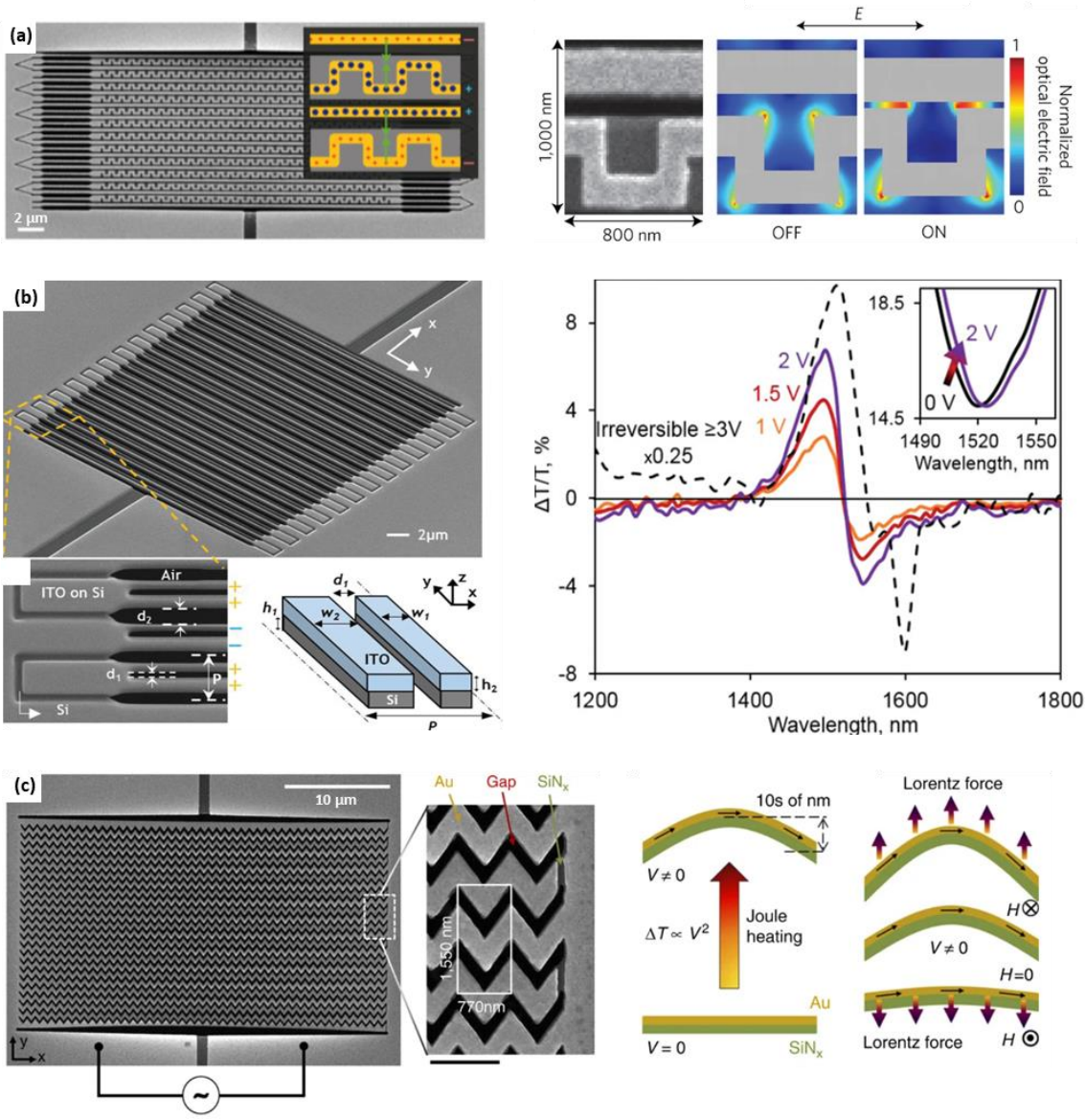

Figure 1.6 Electric and magnetic control of nanomechanical metamaterials. Left panel: SEM image of the electrostatically actuated plasmonic metamaterial reported by Ou et al. The inset shows oppositely charged nanowires giving rise to attractive Coulomb forces (shown as green arrows). Right panel: Unit cell and simulated field distribution of the structure when it is in the OFF (0 V of applied voltage) and ON states for incident light of 1600 nm wavelength polarized parallel to the nanowires [43]. (b) Left panel: SEM images and schematic of a dielectric nanomechanical metamaterial controlled through electrostriction. It consists of silicon (Si)/ indium tin oxide (ITO) bilayer beams of alternating width. P: 800 nm, h_1:100 nm, h_2:70 nm, w_1:200 nm, w_2: 300 nm, d_1:100 nm, d_2:200 nm. Right panel: Relative transmission change of the structure for different applied voltage for light polarized parallel to the beams. The dashed line corresponds to the optical response of the structure (scaled vertically) when the metamaterial beams are irreversibly stuck together, past 3 V. The inset shows the transmission of the structure around its resonance for 0 V and 2 V of applied bias [44]. (c) Left panel: SEM image of a plasmonic nanomechanical metamaterial actuated by the Lorentz force. Right panel: Joule heating in the conducting nanowires, induced by current flow, leads to differential thermal expansion and initial out-of-plane deformation of the nanowires. Application of a magnetic field gives rise to the Lorentz force that leads to displacement of the nanowires perpendicular to the applied field [45].

expansion. In the presence of a magnetic field, this initial thermal displacement can be enhanced or suppressed due to the Lorentz force. Using static magnetic field they demonstrated 25 % relative transmission change for an applied magnetic field of 130 mT and a constant 4 mA current [42], and

while applying alternating currents they achieved up to 2.5 % transmission modulation depth of a 1550 nm laser beam around 200 kHz modulation frequency [45].

Low mass systems employed in nanophotonic structures can be driven by optical forces [46, 47]. Therefore, the combination of nanophotonic and nanomechanical systems can provide all-optical operation and control. Indeed, light driven nanomechanical structures have been used to demonstrate functionalities such as optical control of optomechanical filters [48], optomechanically induced bistability [49, 50] and to perform logic functions in photonic circuits [51]. Additionally, in a more recent development, it was demonstrated that optical forces generated from illumination of nanoantenna arrays can be the driving force for linear and rotational motion of micro-scale objects [52]. Metamaterials are an ideal candidate to explore and exploit optical forces due to the strong field strengths that can arise from high field confinement. Zhao et al. presented an early theoretical study of optical forces in plasmonic nanorods arrays [53] while Zhang et al. performed similar studies based on asymmetric dielectric rods arguing that the magnitude of optical forces in dielectric structures can be an order of magnitude larger than in plasmonic ones due to lower Joule losses and higher quality factor optical response [54, 55]. The first demonstration of a nanomechanical reconfigurable metamaterial driven by optical forces was provided by Ou et al. [56], based on a plasmonic Π-shaped metamolecule array, well studied for its Fano-resonances [57-60], supported by free-standing silicon nitride beams. As seen in the left panel of Figure 1.7 (a), the structure consisted of two types of silicon nitride beams of alternating widths, supporting different parts of the optical resonators. In their experiment, a 1550 nm pump laser was used to drive mechanical oscillations of the system at its mechanical resonance frequencies while a 1310 nm probe laser beam was used to detect the modulated transmission of the structure. Their results showed increasing transmission modulation as a function of the pump optical power, achieving modulation depths of the order of 1 % at mechanical frequencies of around 1 MHz, for sub-milliwatt pump power levels (Figure 1.7 (a), right panel). Much higher operational mechanical frequencies were demonstrated in nano-cantilever, dielectric metamaterials by Karvounis et al [61] (Figure 1.7 (b)). Their structure was fabricated out of a 100 nm thick, free-standing, polycrystalline silicon membrane and a 1550 nm modulated laser beam was used to excite the fundamental oscillation mode of the nano-cantilevers at mechanical frequencies of around 150 MHz. The transmission of the structure was probed at 1310 nm where a maximum modulation of 0.2 % was recorded (Figure 1.7 (b), right panel). It should be noted that the achievable modulation amplitude of such structures will be limited by the optical damage threshold of the constituting materials.

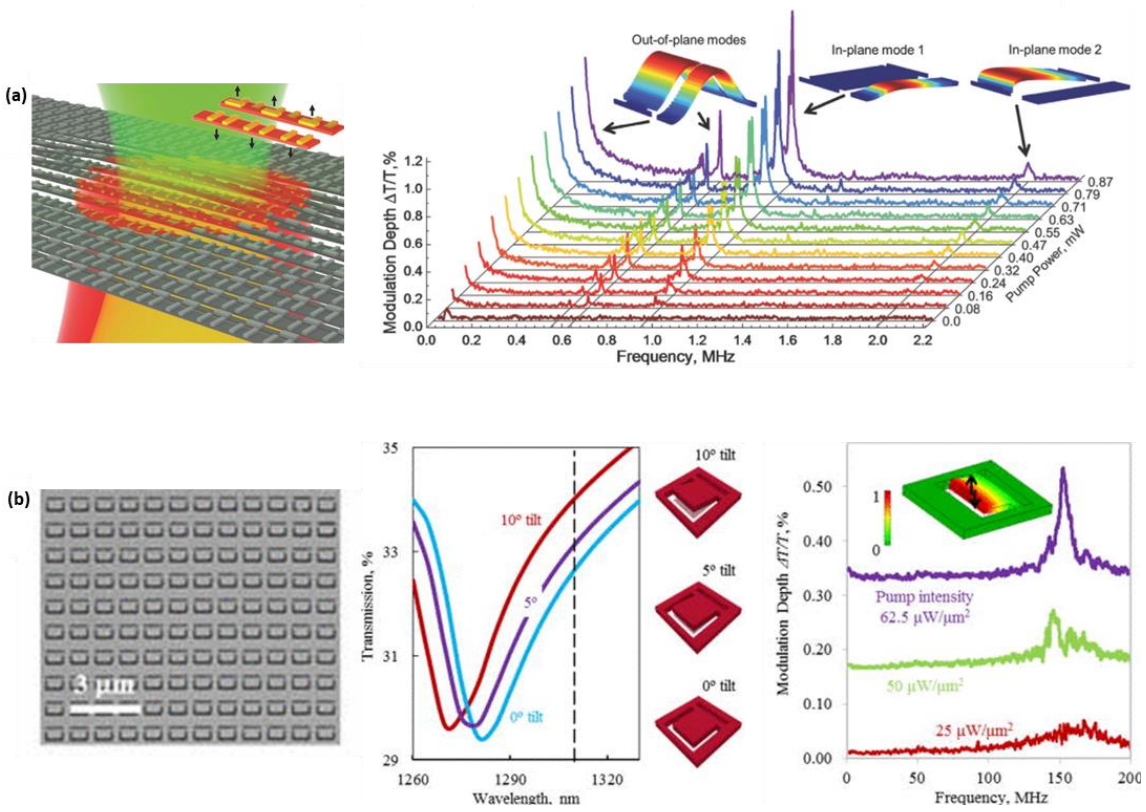

Figure 1.7 Optically reconfigurable nanomechanical metamaterials. (a) Left panel: Illustration of a plasmonic nanomechanical metamaterial where alternating narrow and wide silicon nitride beams support an array of Π-shaped, gold metamolecules. A 1550 nm modulated pump laser beam (red) excites the mechanical resonances of the structure changing its plasmonic response and a 1310 nm probe beam (green) detects the modulated transmission through the structure. Right panel: Measured transmission modulation depth as a function of pump laser modulation frequency for different power levels. Insets show simulation results of the first out-of-plane and in-plane mechanical eigenmodes of the two types of beams [56]. (b) Left panel: SEM image of an all-dielectric nanomechanical metamaterial. Central panel: Simulated transmission of the structure for different tilt angles of the cantilever-based unit cell. The dashed line indicates the probe wavelength of 1310 nm. Right panel: Measured transmission modulation depth as a function of pump laser modulation frequency for three different intensity levels. The inset shows the fundamental out-of-plane mechanical mode of a nano-cantilever unit cell according to numerical modelling [61].

As illustrated by the above examples, nanomechanical metamaterials can provide a range of tuning solutions. Apart from light modulation functionalities discussed here, tunable nanomechanical metamaterials have been used to demonstrate several other effects such as birefringence [62], polarization [63] and colour [64] modulation, as well as dynamic lensing [65] among others.

A further advantage of such metamaterials is that they can be fabricated to provide not only homogeneous, tunable response over the entirety of the surface, but also to provide control over individual metamolecules, or groups of them [66]. This concept of addressable metamaterials was initially introduced in a so-called optofluidic metamaterial [67] i.e. a metamaterial combined with cavities that can be filled with liquid metal. In nanomechanical metamaterials, this principle is illustrated in the work of Cencillo-Abad et al. where they demonstrated an electrothermally driven nanomechanical metamaterial controlled by 13 electrodes and contact pads that allowed tuning of

individual metamaterial nanowires [68] (Figure 1.8 (a)). As suggested by the same authors, such level of position control can provide tunable gratings and lenses all on the same device [69]. An optically reconfigurable addressable metamaterial was demonstrated by Ou et al. [70] (Figure 1.8 (b)). It was based on the Π-shaped plasmonic metamaterial array reported in their earlier work [56], the difference being that the nanomechanical beams supporting the plasmonic resonators had varying length. Since the mechanical eigenfrequency of a beam structure has an inverse dependence on the square of its length, this results in a spatially addressable structure that can be actuated selectively by varying the modulation frequency of the pump laser beam.

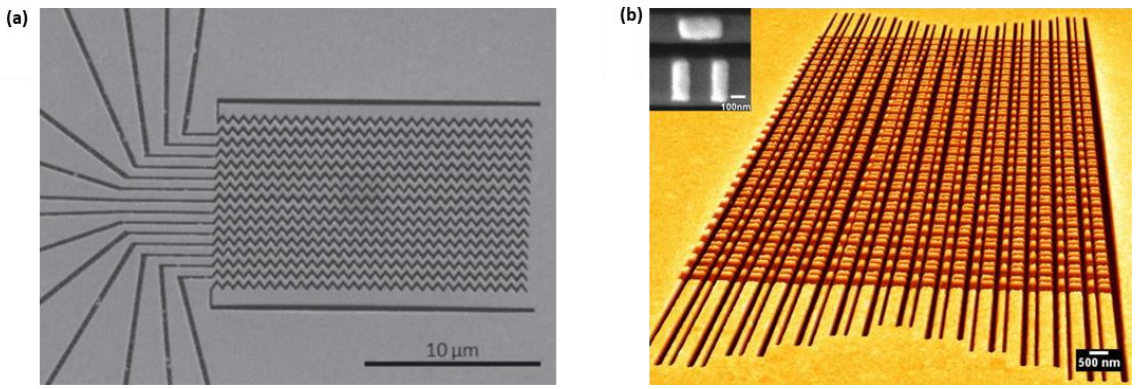

Figure 1.8 Nanomechanical addressable metamaterials. (a) SEM image of an addressable, electrothermally controlled nanomechanical metamaterial fabricated from a gold covered silicon nitride membrane [68]. (b) False coloured SEM image of an optically addressable nanomechanical metamaterial. Red: silicon nitride, yellow: gold. The inset shows an SEM image of the metamaterial unit cell [70].

1.3 Optical detection of thermal motion

Nano- and opto-mechanics offer high sensitivity for optical detection of displacements, masses or forces through motion. In their simplest form, such systems consist of a Fabry-Perot type cavity in which a mechanical element can be introduced, for instance, a thin membrane [71] or a carbon nanotube [72] placed inside the cavity. Other cavity based examples can be found in integrated photonic systems, where the optomechanical part of the system can take the form of disk microresonators cavities [47] or photonic crystals [73]. Another implementation is the use of deformable waveguides as can be found in [74] where the thermal motion of two free-standing, end-to-end coupled waveguides in close proximity, modulates the light transmitted through the circuit.

Similar optomechanical systems can also be fabricated in freestanding membranes. For example, Thijssen et al. demonstrated a plasmonic nanomechanical system consisting of two free-standing, gold-covered silicon nitride beams in close proximity to optically transduce their thermal motion [75] (Figure 1.9 (a)). Optical illumination of the structure with light polarized parallel to the beams resulted in the generation of metal-insulator-metal (MIM) plasmons in the gap separating

the beams, which is highly dependent on the gap width. Optical excitation of the structure and measurement of the thermomechanical signal was performed in a simple microscope configuration (Figure 1.9 (b)). By monitoring the transmission through the structure they were able to detect several of its mechanical modes (Figure 1.9 (c)) and report a displacement sensitivity of the order of tens of fm/Hz$^{-1/2}$. Similar works by the same authors can be found in [76] and [77]. Contrary to integrated optomechanical systems that require complex fabrication procedures, such membrane-based systems can be formed with a one-step focused ion beam (FIB) milling process following a metal deposition procedure. A further advantage is that the method is based on free-space coupling only.

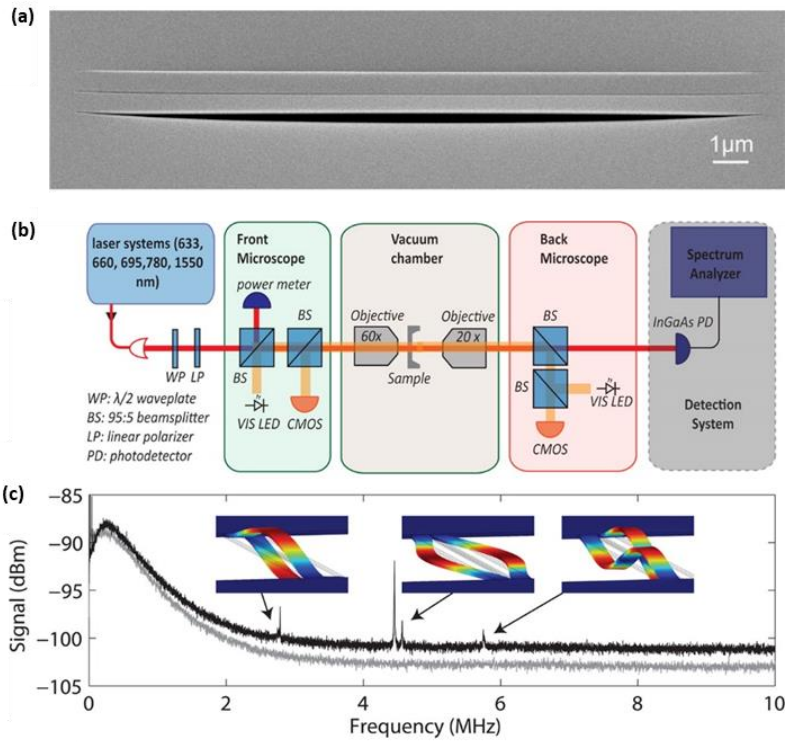

Figure 1.9 Detection of thermal motion of a plasmonic nanomechanical system. (a) SEM image of two free-standing, gold covered silicon nitride beams fabricated via focused ion beam milling. The gap between the beams is 25 nm. (b) Schematic of the experimental setup for detection of thermal motion of the plasmonic, nanomechanical system. (c) Thermomechanical spectrum recorded by a spectrum analyser where four mechanical modes are detected. Insets: finite element method simulations of the respective modes. [75]

The use of free-standing string or beam structures is of great interest for sensing applications. For instance, string resonators are well known to be extremely sensitive to temperature variations [78] and therefore pose an ideal structure to detect such changes by monitoring their natural frequencies. Silicon nitride membranes are widely used for fabrication of such structures due to their availability and the high quality factors they offer. 2D materials are also favoured since they can offer large sensitivities due to their exceptionally low mass [79, 80]. However, the optical detection instrumentation in such applications is usually based on interferometric or vibrometric techniques that offer great displacement sensitivity but are limited by diffraction. Therefore, free-

standing, membrane-based optomechanical systems for motion transduction can lead to further miniaturization of sensing devices.

Nanomechanical metamaterials based on free-standing membrane substrates are ideally suited for detecting the thermal motion of their components since their electromagnetic response depends on the relative positioning of their metamolecules. Therefore, they can not only provide light modulation capabilities but could also serve as sensing elements. Moreover, identification of the natural resonances of such complex mechanical systems through their thermal motion would be beneficial for a complete mechanical characterization of their constituent elements, for instance, fabrication inconsistencies or stress variations could be readily identified.

1.4 Thesis overview

To summarize, nanomechanical metamaterials are a promising platform for light modulation applications. Several tuning schemes have been developed over the years aiming at providing increasing control over their mechanical response, however, a more thorough study of their mechanical properties is still lacking. This thesis aims to fill this gap by demonstrating that such metamaterials are ideally suited to transduce the thermal motion of their mechanical components into fluctuations of their optical properties, allowing identification of the mechanical frequencies at which they can be efficiently driven. Moreover, it is demonstrated that their mechanical resonances can be tuned by light illumination. This introduces further sensing functionalities and expands their operation regime. Additionally, a novel and simple mechanical excitation scheme is introduced based on a piezoelectric element that can allow dynamic operation of nanomechanical metamaterials in the nonlinear regime where mechanical bistability of the system is translated to bistability of its optical properties. These findings are organized in the next five chapters.

Chapter 2 provides theoretical background on beam mechanics and thermomechanical motion of a resonator. The Euler-Bernoulli beam model is introduced and the eigenfrequencies of a doubly-clamped beam resonator are derived, together with the effects of tensile stress on the resonator. Thermal motion in nanomechanical structures is then described by the use of the equipartition theorem and the procedure by which the amplitude of thermally driven motion can be calculated is presented.

Chapter 3 deals with the detection of thermal motion of a plasmonic nanomechanical metamaterial. The experimental setup used in this work is introduced, together with the basic metamaterial design and fabrication techniques used throughout this Thesis. It is experimentally demonstrated that the thermal motion of a plasmonic metamaterial's mechanical elements leads to fluctuations of its reflectivity, allowing identification of its mechanical resonances. It is shown

that the mechanical resonances supported by the metamaterial system are largely dependent on the tensile stress present in the beam elements.

Chapter 4 proposes optical heating as a means of controlling the natural oscillation frequencies of nanomechanical metamaterials. It is shown that in a plasmonic nanomechanical metamaterial system consisting of two doubly-clamped beams, continous tuning of laser illumination power results in continuous tuning of the natural oscillation frequencies of the beams through stress modulation. This constitutes a type of nanomechanical bolometer with optical readout. This is also demonstrated in an addressable metamaterial structure that supports many mechanical resonances leading to an extended operational range of the device.

In Chapter 5 the nonlinear operational regime of nanomechanical metamaterials when driven by a piezoelectric element is examined. To do so, a new design of free-standing silicon nitride membranes was introduced that allows clamping of the metamaterial beams directly on the silicon frame of the supporting chip. It is shown that nonlinear excitations of the metamaterial beams lead to a bistable response of the structure at its mechanical resonances depending on the direction of frequency excitation. Optically induced stress modulation in the structure allows optical control of the bistable response enabling switching between mechanical states with just a few μW of optical power.

Lastly, a summary of this Thesis is presented in Chapter 6, together with possible future research directions.

Chapter 2

Mechanics of nanomechanical metamaterials

A wide variety of geometries and configurations of nanomechanical structures can be utilized in optomechanical systems. The simplest and most widely used are membranes, cantilevers, beams and strings. Free-standing, thin dielectric membranes are commercially available and can be easily patterned to form free-standing cantilevers or beams. Apart from ease of fabrication, a further advantage of such ideal structures is that analytical models can be readily used to examine the effects of material parameters and geometry on the structure's resonant behaviour.

The nanomechanical metamaterials studied in this Thesis consist of doubly-clamped beams formed out of thin, free-standing silicon nitride membranes. Therefore, this chapter starts by introducing the Euler-Bernoulli beam model which is then used to derive the eigenfrequencies of the mechanical modes of doubly-clamped beams. Additionally, the effect of tensile stress on a beam resonator is examined. Next, a typical design of a nanomechanical metamaterial is introduced in Section 2.2. This essentially consists of two beam resonators with fixed ends that together support an array of optical resonators. The eigenfrequencies of various mechanical modes of the metamaterial structure are calculated from mechanical simulations. Finally, in Section 2.3, thermal motion in nanomechanical structures is discussed. Nanoscale structures with picogram scale mass are expected to undergo thermal oscillations at their mechanical resonances due to thermal forces acting on them. The theoretically expected amplitude of motion of a resonator at a given temperature is derived based on the equipartition theorem and the procedure by which the motion of a nanomechanical structure can be calibrated from its power spectral density spectrum is detailed. This last part forms the basis on which the analysis of the experimental results presented in Chapter 3 is performed.

2.1 The Euler-Bernoulli beam model

The Euler-Bernoulli beam model is used to model the bending behaviour of slender beams (ratio of length to thickness of more than ten, $L/h > 10$) under the assumption that the beam has no shear deformation and rotational inertia. Then, following [78], for a beam composed of linear elastic material and constant cross-section along its length, its equation of motion will be given by the differential equation

$$\rho A \frac{\partial^2 u(x,t)}{\partial t^2} + EI \frac{\partial^4 u(x,t)}{\partial x^4} = 0 \tag{2.1}$$

where, ρ is the density of the material, A is the cross-section area, E is the material's Young modulus, I is the geometric moment of inertia and $u(x,t)$ is the displacement. Its solution can be separated into a position and time-dependent term

$$u(x,t) = \sum_{n=1}^{\infty} U_n(x) cos(\omega t) \tag{2.2}$$

where n is the vibrational mode number, ω is the structure's angular frequency of motion and $U_n(x)$ is its displacement function that has a general solution of the form

$$U_n(x) = a_n cos\beta_n x + b_n sin\beta_n x + c_n cosh\beta_n x + d_n sinh\beta_n x \tag{2.3}$$

where β_n is the wavenumber. The first two terms of the above equation describe standing waves in the beam and the last two terms represent the effects of clamping of the beam's ends. Equation (2.1) then becomes

$$-\rho A\omega^2 u(x,t) + EI\beta_n^4 u(x,t) = 0 \tag{2.4}$$

Solving for ω gives the angular eigenfrequencies

$$\omega_n = \beta_n^2 \sqrt{\frac{EI}{\rho A}} \tag{2.5}$$

2.1.1 Mechanical resonances of doubly-clamped beams

The boundary conditions for a beam that is fixed at both ends (doubly-clamped beam), as in Figure 2.1, are

$$U_n(0) = 0, \qquad U_n(L) = 0, \qquad \frac{\partial U_n(0)}{\partial x} = 0, \qquad \frac{\partial U_n(L)}{\partial x} = 0 \tag{2.6}$$

In other words, the beam ends experience zero displacement and bending.

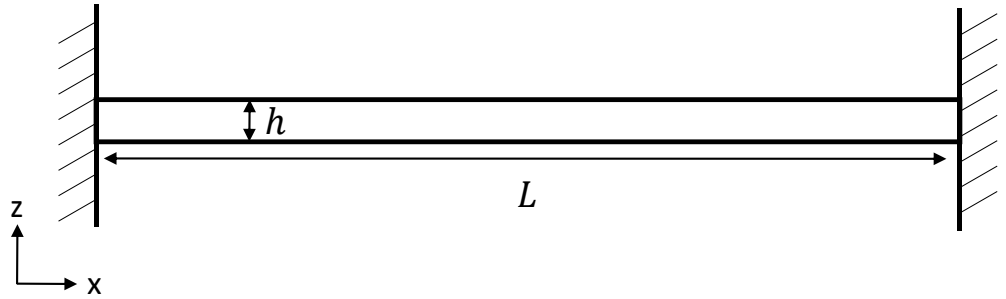

Figure 2.1 Schematic illustration of a uniform, doubly-clamped beam. L: Length of the beam, h: thickness of the beam.

Equations (2.3) and (2.6) result in a system of equations

$$\begin{bmatrix} 1 & 0 & 1 & 0 \\ 0 & 1 & 0 & 1 \\ -sin(\beta_n L) & cos(\beta_n L) & sinh(\beta_n L) & cosh(\beta_n L) \\ cos(\beta_n L) & sin(\beta_n L) & cosh(\beta_n L) & sinh(\beta_n L) \end{bmatrix} \begin{Bmatrix} a \\ b \\ c \\ d \end{Bmatrix} = \begin{Bmatrix} 0 \\ 0 \\ 0 \\ 0 \end{Bmatrix} \quad (2.7)$$

Setting the determinant to zero gives

$$cos(\beta_n L)\, cosh(\beta_n L) - 1 = 0 \quad (2.8)$$

which can be used to determine β_n. Setting $\lambda_n = \beta_n L$, for n = 1, 2, 3, $n > 3$ $\lambda_n$takes the values λ_n = 4.7300, 7.8532, 10.9956, $(2n+1)\pi/2$ respectively [78]. The angular eigenfrequency of a doubly-clamped beam can now be written as

$$\omega_n = \frac{\lambda_n^2}{L^2}\sqrt{\frac{EI}{\rho A}} \quad (2.9)$$

For a beam with rectangular cross-section the moment of inertia is $I = Ah^2/12$, where h is the thickness of the beam and $A = wh$, where w is the width. Equation (2.9) then becomes

$$\omega_n = \frac{\lambda_n^2}{L^2} h \sqrt{\frac{E}{12\rho}} \quad (2.10)$$

For the first vibrational mode (n = 1) and since $\omega = 2\pi f$ the eigenfrequency is given by

$$f_1 = 1.03\frac{h}{L^2}\sqrt{\frac{E}{\rho}} \quad (2.11)$$

Equation (2.11) gives the eigenfrequency of the fundamental vibrational mode in the thickness direction i.e. in the out-of-plane direction. Substituting the beam thickness, h, with the width of the beam, w, gives the eigenfrequency of the first in-plane vibrational mode.

2.1.2 Mechanical resonances of doubly-clamped beams under tensile stress

The simple case described in the previous section assumes that there is no stress in the beam. However, thin films and membranes used in beam fabrication are usually pre-stressed either as a consequence of their fabrication procedure or by design. In free-standing membranes for instance, high stress is favoured as it enhances the quality factor of their mechanical resonances. In beam structures, increase of tensile stress leads to higher resonance frequencies.

Following [78] the presence of tensile stress σ in a beam results in an additional restoring force $N = \sigma A$ which modifies equation (2.1) resulting in

$$\rho A \frac{\partial^2 u(x,t)}{\partial t^2} + EI \frac{\partial^4 u(x,t)}{\partial x^4} - N \frac{\partial^2 u(x,t)}{\partial x^2} = 0 \tag{2.12}$$

Solving this equation results in the dispersion relation

$$\omega_n = \sqrt{\frac{EI}{\rho A}\beta_n^4 + \frac{\sigma}{\rho}\beta_n^2} = \beta_n^2 \sqrt{\frac{EI}{\rho A}} \sqrt{1 + \frac{\sigma A}{EI\beta_n^2}} \tag{2.13}$$

which is Equation 2.5 multiplied by a term that increases with stress.

Again, as for the unstressed beam, taking the first vibrational mode (n = 1) and $\omega = 2\pi f$ we can write

$$f_1 = 1.03 \frac{h}{L^2} \sqrt{\frac{E}{\rho}} \sqrt{1 + \frac{\sigma L^2}{3.4Et^2}} \tag{2.14}$$

Therefore, the eigenfrequency of a stressed beam is the eigenfrequency of the beam under zero stress multiplied by the term $\sqrt{1 + \frac{\sigma L^2}{3.4Et^2}}$. This shows that an increase of tensile stress in a beam will increase its resonance frequency. Therefore, tuning of the internal stress in a nanomechanical structure can provide tunable frequency response.

2.2 Mechanical analysis of metamaterial beams

The metamaterial structures studied in this Thesis consist of silicon nitride beams supporting gold-based metamolecules. Such structures have varying cross-section and therefore, finite element modelling (FEM) is used to calculate their mechanical resonances. We use COMSOL Multiphysics (version 5.3a) to simulate the mechanics of the metamaterial structures. The material parameters used in modelling can be found in Table 2.1 and were obtained from [81].

A comparison between the analytical formulas and simulations can be performed for the simple case of a uniform beam with clamped edges. Considering a silicon nitride beam with length L= 15.8 μm, thickness h= 50 nm, width w= 150 nm, Young's modulus E= 260 GPa, density ρ= 3100 kg/m^3 and using Equation (2.11) we can calculate its mechanical eigenfrequencies analytically. For the first out-of-plane and in-plane modes we find 1.889 MHz and 5.667 MHz respectively. These values are in good agreement with those obtained from FEM modelling, 1.886 MHz and 5.654 MHz respectively.

Using finite element modelling we can also simulate the structure's mechanical resonances in the presence of tensile stress. To do so, tensile stress is added along the length of the beam and

the eigenvalue problem is solved for every input stress value. This is illustrated in Figure 2.2 for stress values ranging from 0 to 100 MPa in steps of 5 MPa. Comparing the simulation results with the analytical solution provided by Equation (2.14) it can be seen that for the out-of-plane mode the simulated eigenfrequencies at stresses above 30 MPa are underestimated. In contrast, there is good agreement between simulated and analytical solutions for the in-plane mode up to 100 MPa. This has been attributed to the number of mesh elements in the bending direction [82]. Since the thickness of the structure is three times smaller than its width, the number of mesh elements in the thickness direction is three times lower. These results indicate that by modelling the more complex geometry of metamaterial beams at low stresses we can obtain the stress-dependent eigenfrequencies of their fundamental mode. This will be examined further in Chapter 4.

Table 2.1 Mechanical properties of silicon nitride and gold.

Material	Young's modulus (E)	Density (ρ)	Poisson's ratio (ν)
Silicon nitride (Si_3N_4)	260 GPa	3100 kg/m^3	0.23
Gold (Au)	77 GPa	19300 kg/m^3	0.44

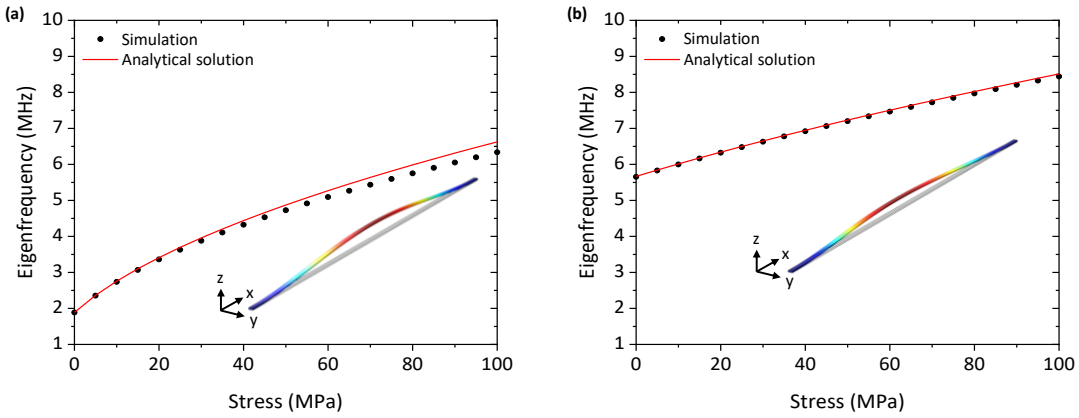

Figure 2.2 Stress dependence of mechanical eigenfrequencies. Mechanical eigenfrequencies of a 15.8 µm long silicon nitride beam as a function of its tensile stress for the (a) first out-of-plane and (b) first in-plane mode. Black dots are values obtained from simulations. Red lines are analytical solutions based on Equation (2.14). Insets show the simulated mechanical modes.

The metamaterial structures used in this Thesis are based on the plasmonic Π-shaped design introduced in [56]. An illustration of such a structure can be seen in Figure 2.3. The simulated structure consists of two silicon nitride beams, a narrower one with a width of 230 nm and a wider one with a width of 280 nm. Both beams have a thickness of 50 nm and each one supports a different part of an array of gold metamolecules that are also 50 nm thick. The narrow beam supports a row of horizontal gold bars, 350 nm in length with a periodicity of 800 nm. The wide beam supports a row of vertical gold bar pairs, also with a periodicity of 800 nm. Each pair consists

of two bars, 110 nm in width, separated by 185 nm. The total length of the beams is 14.43 µm and together they support 14 metamaterial unit cells. The outer part of the beams is left unstructured and the edges are fixed. The simulation results for the first six mechanical modes of the structure can be seen in Figure 2.4. The fundamental (first order out-of-plane) mechanical modes of the structure can be found at 1.7 MHz and 1.87 MHz. Due to different gold coverage the two beams have slightly different mechanical eigenfrequencies. The larger gold coverage of the narrow beam results in a lower eigenfrequency.

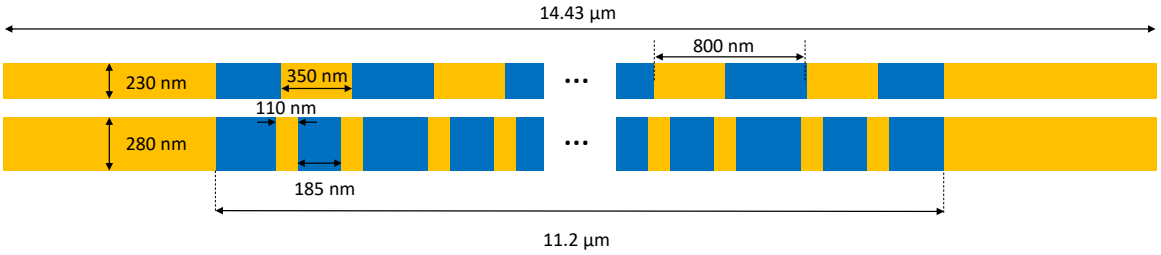

Figure 2.3 Schematic representation of the simulated nanomechanical metamaterial beams.

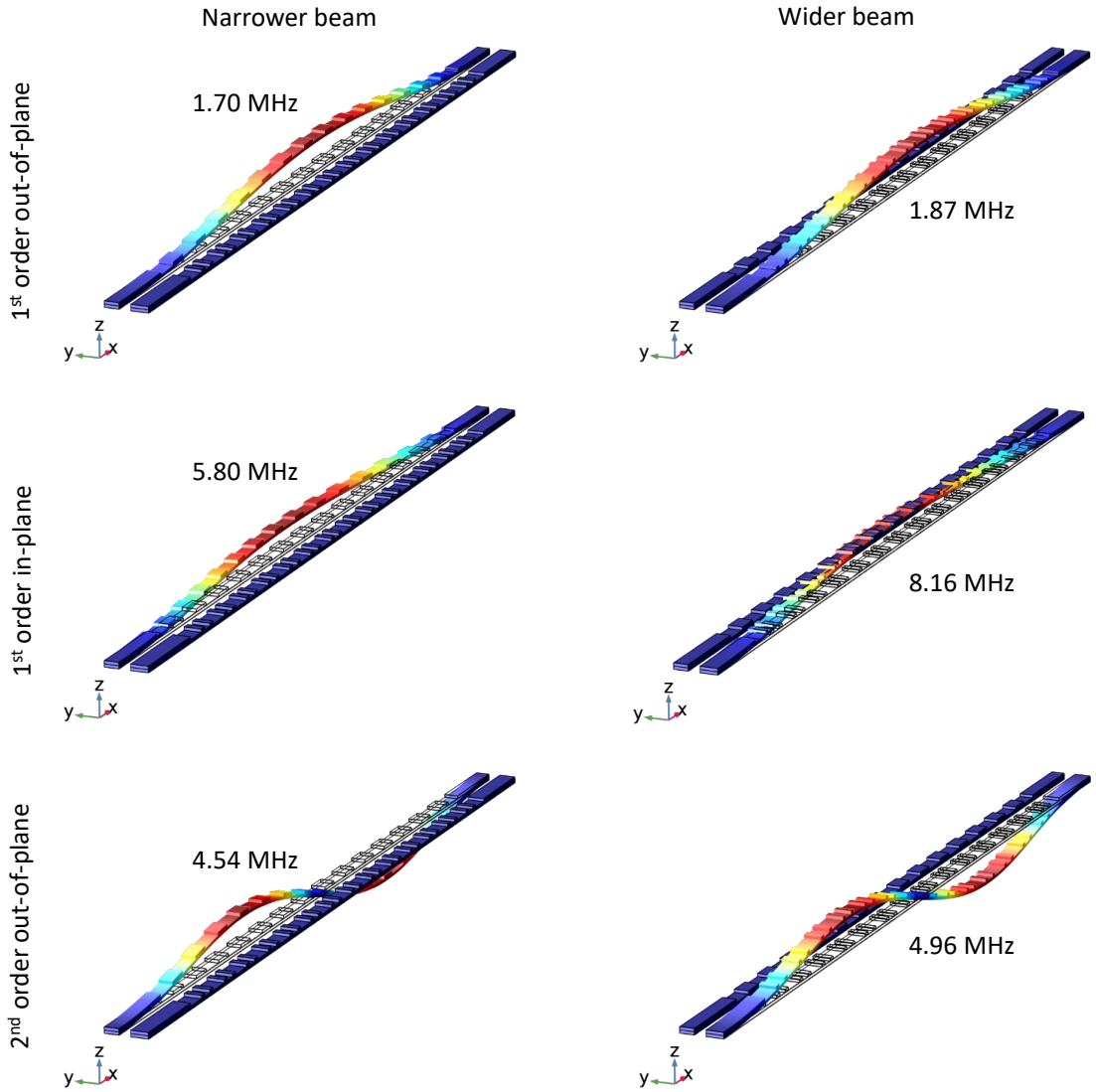

Figure 2.4 Simulated mechanical modes of the nanomechanical metamaterial beams.

2.3 Thermal motion in nanomechanical structures

The displacement of a simple one-dimensional resonator can be expressed as

$$u(x,t) = \sum_n u_n(x,t) = \sum_n z_n(t) U_n(x) \tag{2.15}$$

where $U_n(x)$ is the vibrational mode shape and $z_n(t)$ is determined from mapping each mechanical mode to a damped harmonic oscillator described by [83]

$$m_{\text{eff}}\ddot{z} + m_{\text{eff}}\gamma\dot{z} + m_{\text{eff}}\omega_0^2 z = F(t) \tag{2.16}$$

Here, m_{eff} is the effective mass of the structure, $\omega_0 = 2\pi f_0 = \sqrt{(k_{\text{eff}}/m_{\text{eff}})}$ is the natural angular frequency of oscillation, f_0 is the natural frequency and k_{eff} is the spring constant. The resonance quality factor is $Q = {}^{f_0}/_{\gamma}$.

The majority of nanomechanical metamaterials are constructed from cantilevers or doubly-clamped beam structures of microscopic length and nanoscale cross-section. Such structures are subjects to thermal forces giving rise to their thermal motion. This thermal motion is driven internally, by momentum transfer resulting from the annihilation and creation of phonons in the mode. Nanostructures such as beams and cantilevers can be modelled as damped mechanical oscillators driven by a time dependent thermal force F_{th}

$$m_{\text{eff}}\ddot{z} + m_{\text{eff}}\gamma\dot{z} + m_{\text{eff}}\omega_0^2 z = F_{\text{th}}(t) \tag{2.17}$$

The thermal energy of a structure can be related to its time-averaged motion through the equipartition theorem according to which, every degree of freedom that contributes a quadratic term to the total energy of the structure will have an average energy equal to $k_B T/2$ [83] with k_B being the Boltzmann constant and T the temperature. The mean energy $\langle E \rangle$ of an oscillator is given by

$$\langle E \rangle = \frac{1}{2} m_{\text{eff}} \langle \dot{z}^2 \rangle + \frac{1}{2} k_{\text{eff}} \langle z^2 \rangle \tag{2.18}$$

and according to the equipartition theorem, we can write [83, 84]

$$\frac{1}{2} m_{\text{eff}} \langle \dot{z}^2 \rangle = \frac{1}{2} k_{\text{eff}} \langle z^2 \rangle = \frac{1}{2} m_{\text{eff}} {\omega_0}^2 \langle z^2 \rangle = \frac{1}{2} k_B T \tag{2.19}$$

From here the theoretical root-mean-squared (RMS) amplitude of a resonator's motion can be calculated as

$$\delta_{rms} = \sqrt{\langle z^2 \rangle} = \sqrt{\frac{k_B T}{m_{\text{eff}} {\omega_0}^2}} = \sqrt{\frac{k_B T}{m_{\text{eff}} (2\pi f_0)^2}} \tag{2.20}$$

2.3.1 Power spectral density

Any method used to detect a resonator's motion will pick up a time-varying signal such as voltage that, in the frequency domain, provides a spectral representation of its motion. The square of that signal divided by the resolution bandwidth of the instrument gives the power spectral density (PSD), $S_{zz}(\omega)$, of the signal. Following [83], a resonator's mean-square amplitude of motion is related to its PSD as

$$\langle z^2(t) \rangle = \frac{1}{2\pi} \int_0^\infty S_{zz}(\omega) d\omega \tag{2.21}$$

Taking the Fourier transform, $\mathcal{F}$, of Equation (2.17) yields

$$\mathcal{F}\{z(t)\} = \chi(\omega) \mathcal{F}\{F_{th}(t)\} \tag{2.22}$$

where $\chi(\omega)$ is the frequency response function

$$\chi(\omega) = \frac{\mathcal{F}\{z(t)\}}{\mathcal{F}\{F_{th}(t)\}} = \frac{1}{m_{\text{eff}}(\omega_0^2 - \omega^2 + i\omega\, \omega_0/Q)} \tag{2.23}$$

Then the spectral densities of mean-square amplitude and force are related through the transfer function $|\chi(\omega)|^2$

$$S_{zz}(\omega) = |\chi(\omega)|^2 S_{th}(\omega) \tag{2.24}$$

Combining Equations (2.21), (2.23), (2.24) and since $S_{th}(\omega)$ is a constant thermal force noise $S_{th}(\omega) = S_{th}$, we can write for the mean-square amplitude of motion

$$\langle z^2(t) \rangle = \frac{S_{th}}{2\pi m_{\text{eff}}^2} \int_0^\infty \frac{1}{(\omega^2 - \omega_0^2)^2 + (\omega\omega_0/Q)^2} d\omega = \frac{S_{th} Q}{4\omega_0^3 m_{\text{eff}}^2} \tag{2.25}$$

Combining with the equipartition theorem (2.19) yields

$$S_{th} = \frac{4 k_B T \omega_0 m_{\text{eff}}}{Q} \tag{2.26}$$

Then the PSD of the resonator can be written in terms of angular frequency ω as

$$S_{zz}(\omega) = \frac{4 k_B T \omega_0}{m_{\text{eff}} Q[(\omega^2 - \omega_0^2)^2 + (\omega\omega_0/Q)^2]} \tag{2.27}$$

And in terms of frequency f as

$$S_{zz}(f) = \frac{k_B T f_0}{2\pi^3 m_{\text{eff}} Q[(f^2 - f_0^2)^2 + (f f_0/Q)^2]} \tag{2.28}$$

with units of m^2/Hz.

Since a detection system will typically measure the signal arising from a resonator's motion in terms of voltage, we can express the PSD of the recorded voltage signal in terms of the PSD of the resonator's motion as

$$S_{VV}(V) = S_{VV}^{noise} + a S_{zz}(f) \tag{2.29}$$

Here, S_{VV}^{noise} is an offset that is constant due to noise from the detection system and the term a has units of V^2/m^2. Therefore, a allows conversion of the resonator's displacement PSD to the measured voltage PSD and depends on experimental parameters such as the detection system and the ability of the measured structure to transduce its motion in some voltage variations for instance, by varying its optical properties that are then detected as light intensity variations and converted to voltage by a photodetector. By fitting an experimentally measured PSD of a resonator that exhibits a thermal motion resonance around a frequency f_0 with Equation (2.29), the offset noise S_{VV}^{noise}, its resonance frequency f_0 and quality factor Q as well as the conversion factor a can be determined. Converting the PSD spectrum to displacement spectral density via the conversion factor a and integrating over the entire width of the resonance, the experimental RMS displacement of the resonator can be determined from Equation (2.21).

2.3.2 Effective mass

In the previous section, the effective mass of a resonator is used instead of its total mass m. Since the displacement of a resonator is not constant along its length, a correction must be introduced that takes into account the extent of the displacement along the entire structure. Therefore, the effective mass is used in order to account for the varying degree of the structure's displacement while leaving the motion amplitude uncorrected. Assuming a resonator with n number of modes, the effective mass of the n^{th} mode can be determined through its potential energy. Following [83] and partitioning the resonator into elements of volume dV and mass $dm = \rho\, dV$, the potential energy of the elements can be written as

$$\frac{1}{2}\, dm\, \omega_n^2 \boldsymbol{u}(x,t)^2 = \frac{1}{2}\rho\, dV\, \omega_n^2 |z_n(t)\boldsymbol{U}_n(\boldsymbol{x})|^2 \tag{2.30}$$

Here, ρ is the density of the element and $\boldsymbol{U}_n(\boldsymbol{x})$ is the normalized three-dimensional mode shape such that the maximum value of $|\boldsymbol{U}_n(\boldsymbol{x})|$ is unity. Integration over the volume of the structure will give

$$\frac{1}{2}\omega_n^2|z_n(t)|^2 \int \rho\,|\boldsymbol{U}_n(\boldsymbol{x})|^2 dV = \frac{1}{2}\omega_n^2|z_n(t)|^2 m_{\mathrm{eff},n} \tag{2.31}$$

where

$$m_{\mathrm{eff},n} = \int \rho\,|\boldsymbol{U}_n(\boldsymbol{x})|^2 dV \tag{2.32}$$

For the simplest case of one-dimensional motion of a resonator with uniform density and cross-sectional area A the above expression simplifies to

$$m_{\mathrm{eff},n} = \rho A \int_0^L |U_n(x)|^2 dx \tag{2.33}$$

However, since the metamaterial beam structures described in Section 2.2 have varying cross-section and consist of materials with different densities, we use FEM to calculate the effective masses associated with the mechanical modes of the structures based on the general expression (2.32). To do so, the mode shape of each beam is normalized with respect to the maximum displacement of its central part in order to obtain the effective masses associated with the fundamental mechanical mode. For instance, for the fundamental modes of the narrow and wide metamaterial beams discussed in Section 2.2 we calculate effective masses of 0.69 pg and 0.6 pg respectively. From Equation (2.20) the theoretical RMS amplitude of the metamaterial mechanical resonators can be calculated. Using the above effective masses, the mechanical eigenfrequencies of the fundamental out-of-plane modes ($f_{0,narrow} = 1.70$ MHz, $f_{0,wide} = 1.87$ MHz) and assuming operation at room temperature, T= 300 K, we calculate δ_{rms}= 230 pm for the narrow and δ_{rms}= 223 pm for the wide metamaterial beam.

2.4 Conclusions

In this chapter, we introduced the basics of beam theory and derived the eigenfrequency equation of a uniform doubly-clamped beam. Additionally, it has been shown that tensile stress in a beam resonator increases its mechanical eigenfrequency. Here, there is good agreement between the analytical solution and the modelling results. We also introduced a typical metamaterial design and identified its mechanical eigenfrequencies though simulations. As it will become clear in the following chapters, mechanical stress in metamaterial structures greatly influences their mechanical resonances.

Moreover, thermal motion in nanomechanical structures has been described. Considering that the metamaterial nanomechanical beams have picogram-scale masses, they are expected to oscillate at their fundamental mode by 100s of picometers at room temperature. We also described

the procedure by which a PSD spectrum of a nanomechanical structure can be used to calibrate its thermally driven motion. In the next chapters this procedure is applied to nanomechanical metamaterials. It will be shown that such metamaterials effectively transduce the thermal motion of their components to modulation of their optical properties allowing identification of the mechanical resonances at which they can be effectively driven.

Chapter 3

Detection of thermal motion in nanomechanical plasmonic metamaterials

The thermal vibration frequencies of components of nanomechanical devices increase as objects decrease in size and the amplitude of such oscillations becomes increasingly important. In nanomechanical devices, they are of picometric scale, in the mega- to gigahertz range and result in small fluctuations of optical properties. Optomechanical transduction of natural oscillations has been observed in cantilevers [85, 86], single plasmomechanical dimer antenna [77] and metal-insulator-metal [75, 76] resonators as well as other optomechanical systems [87], and exploited in atomic force microscopy [88]. While optical resonances can be characterized in routine transmission and reflection experiments, mapping the high frequency mechanical resonances of complex metamaterial structures is challenging. In this chapter, it is shown that high-frequency time-domain fluctuations of the optical reflection of nano-opto-mechanical metamaterials are directly linked to the thermal motion of their components and can give information on the fundamental mechanical frequencies and damping of the mechanical modes.

The experimental results presented in this chapter are part of a publication by me and Jinxiang Li where we report on the detection of reflectivity and transmission fluctuations in a plasmonic and dielectric nanomechanical metamaterial, respectively. The studies were performed independently, using dedicated experimental setups with different types of metamaterials that were developed and fabricated independently. My results, presented here, consist of the fabrication, simulation and reflectivity fluctuation detection of a plasmonic nanomechanical metamaterial.

In Section 3.1 I introduce the experimental measurement setup I used for probing the reflectivity of the plasmonic metamaterial structure. It is based on an inverted microscope setup that is used for the rest of the experimental results presented in this Thesis. Section 3.2 describes the fabrication steps of the plasmonic nanomechanical metamaterials via focused ion beam milling. Section 3.3 presents the theoretical description of optical property fluctuations due to thermal motion in a metamaterial array and their experimental detection. The theoretical description was mostly developed by Tongjun Liu. Experimentally, I show that at room temperature the magnitude of reflection fluctuations of nanomechanical metamaterials is on the scale of 0.1% but may reach 1.5% at optical resonances.

3.1 Experimental setup

In order to detect reflectivity modulation of the nanomechanical metamaterials the experimental setup illustrated in Figure 3.1 was used. The setup consists of an inverted optical microscope (Nikon Ti) where continuous wave (CW) laser light is introduced from the top, see also Figure 3.2 (a), (b). For the experimental measurements, a 1310 nm fibre-coupled laser (Thorlabs, FPL1053S) was used. The laser beam is initially split using a 99:1 fibre beam splitter. 1% of the laser beam is directed towards a power meter in order to monitor the power levels of the laser. The 99% of the beam is collimated and directed towards two polarizers. Polarizer P2 controls the polarization of the beam while polarizer P1 is used to adjust the laser power incident on the sample (Figure 3.2 (b)). The laser beam then enters the microscope and is directed towards the sample by a 45:55 beam-splitter before being focused on the sample surface using a 20x objective (N.A. 0.4). The reflected light is collected from the objective and encounters the 8:92 beam-splitter where the small percentage of the reflected light (8%) is directed towards an infrared CCD camera used to image the sample. The remainder of the reflected beam is collimated with a micro-collimator and guided to a photodiode (New Focus Inc., 1811-FC) using a multimode optical fibre. An electrical spectrum analyser (Zurich Instruments, UHFLI) is used to detect any modulation of the sample's reflectivity.

The metamaterial samples are placed inside a vacuum chamber (Linkam) and pumped down to around 4 x 10^{-3} mbar pressure. The vacuum chamber sits on an X-Y translation stage to control the position of the sample with respect to the incident laser beam (Figure 3.2 (c)). The vacuum chamber is also equipped with electrical connections to actively drive the metamaterial sample as will be demonstrated in Chapter 5.

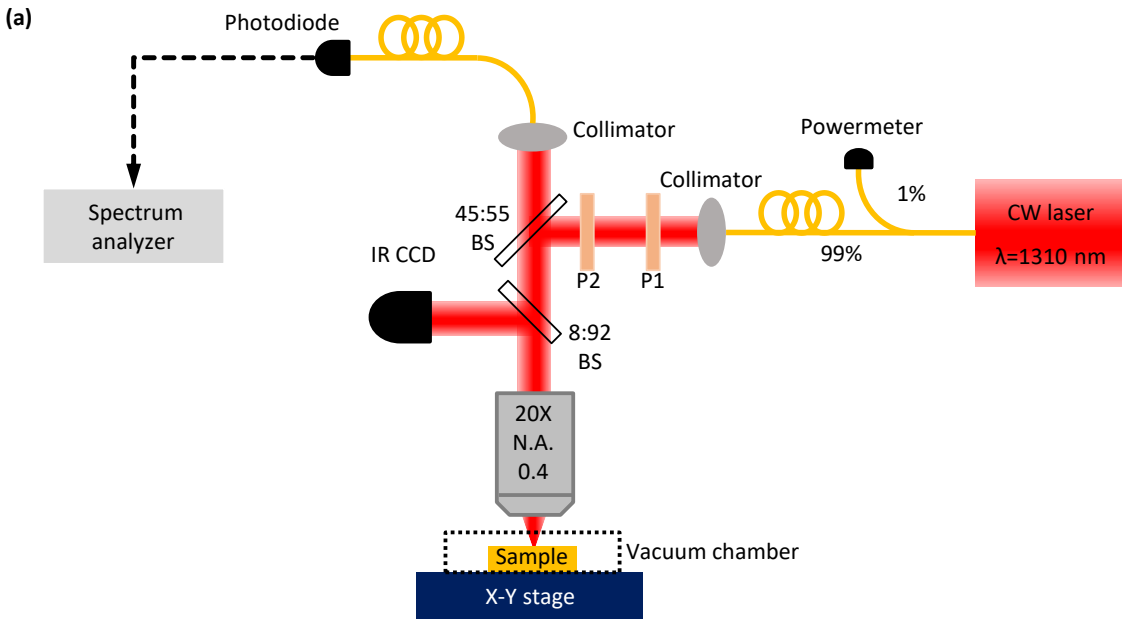

Figure 3.1 Schematic of the experimental setup for thermal motion detection of nanomechanical metamaterials. P1, P2: Polarizers, BS: Beam-splitter, IR CCD: Infrared charged coupled device N.A.: Numerical aperture.

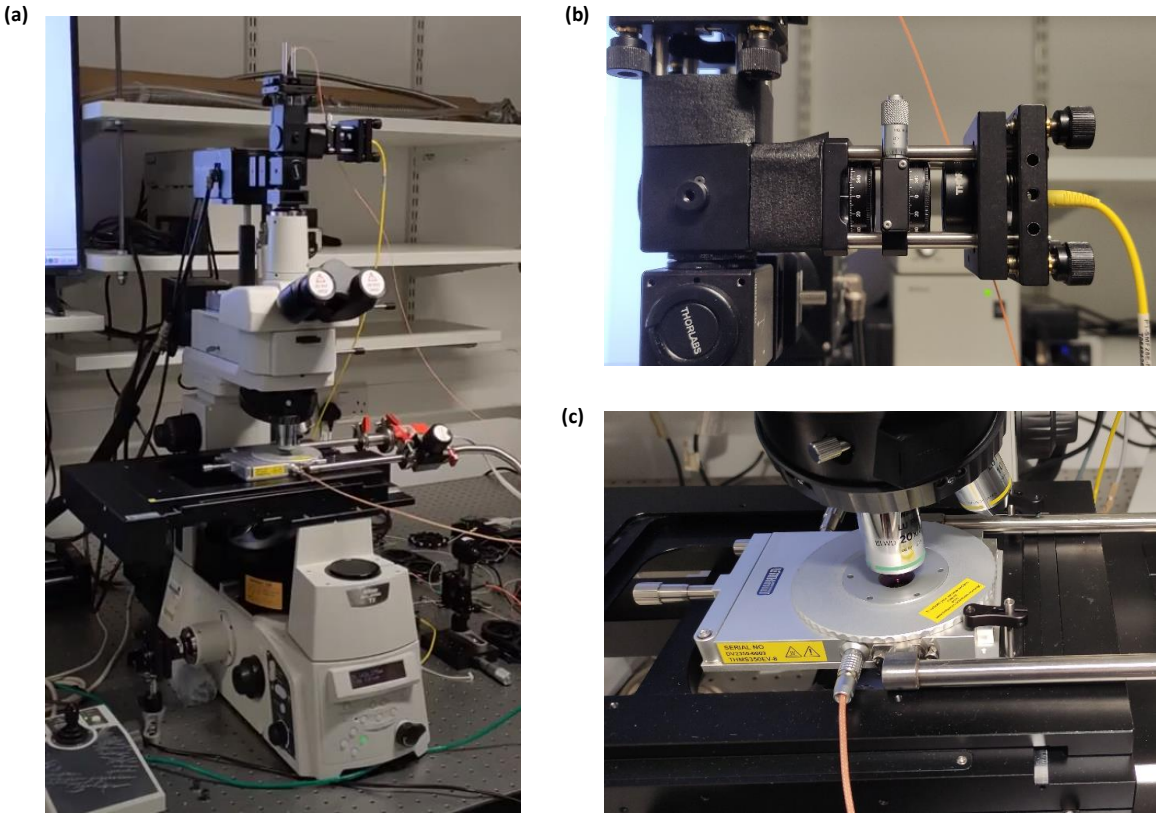

Figure 3.2 Photographs of the experimental setup for thermal motion detection. (a) The Nikon inverted microscope. (b) Input laser port. Two polarizers are used to control the polarization and intensity of the laser beam before entering the microscope. (c) Linkam vacuum chamber.

3.2 Fabrication of nanomechanical metamaterials

Similar to other membrane-based metamaterials [39-45, 56, 70], the structures employed in this Thesis consist of optical resonators supported by silicon nitride membranes of nanometre-scale thickness. The nanomechanical metamaterials were fabricated by focused ion beam (FIB) milling of gold (Au) covered free-standing membranes. The main advantage of FIB milling compared to other nanofabrication techniques is that it does not require the use of resist materials that have to be chemically removed since the process is based on physical sputtering [89, 90]. Moreover, it offers reasonable fabrication times with good flexibility in the structure shapes that can be realized [89]. A dual beam FIB-SEM system (Helios 600 Nanolab) equipped with a gallium liquid metal ion source was used for the fabrication of the metamaterial samples. More details on the operation principle of FIB can be found in Appendix A.

The membranes used were commercially available, low stress (< 250 MPa) silicon nitride (Si_3N_4) membranes with a thickness of 50 nm, supported by a silicon frame, 200 µm thick (Norcada Inc.). For all samples, 50 nm of gold were deposited on top of the Si_3N_4 membranes using thermal evaporation prior to FIB milling. The milling consists of two steps. First, the gold-based optical resonators are partially formed by milling through the gold layer and in a second step the Si_3N_4 beams are formed by milling through the Au/Si_3N_4 bilayer. The fabrication procedure is illustrated in Figure 3.3.

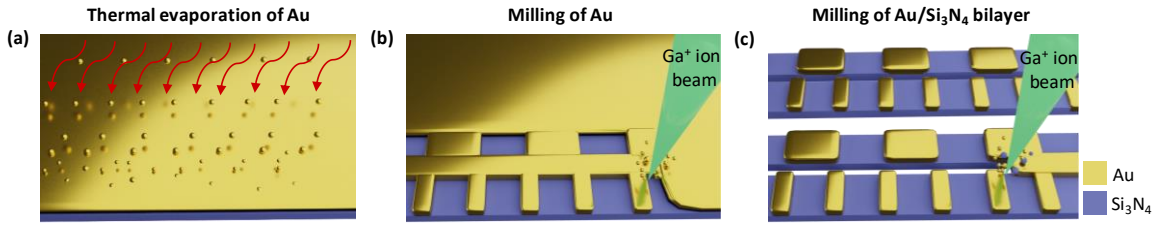

Figure 3.3 Schematic illustration of the fabrication procedure. (a) Thermal evaporation of 50 nm thick Au film on top of a 50 nm thick Si_3N_4 membrane. (b) First step of the FIB milling process: Optical resonators are formed by partially patterning the gold film. (c) Second step of the FIB milling process: The nanomechanical beam resonators are formed by milling through the Au/Si_3N_4 bilayer.

The fabrication system also allows SEM imaging. Figure 3.4 (a), (b) show SEM images of a nanomechanical metamaterial array fabricated on a 500 µm x 500 µm low stress Si_3N_4 membrane together with simulated and measured optical properties of the structure. In this example, the milled array consists of 17 pairs of Si_3N_4 beams with a length of 19 µm and each beam pair supports 21 unit cells of the plasmonic metamolecule with a periodicity of 700 nm. Characterization of the array with a microspectrophotometer (CRAIC) reveals a plasmonic absorption resonance around 1200 nm wavelength (Figure 3.4 (c)). The measured optical properties of the array for incident light polarized parallel to the beams are in qualitative agreement with the simulation results shown in

Figure 3.4 (d). Broadening of the resonances and generally weaker resonances are a consequence of imperfections introduced by the fabrication process. FIB milling inevitably leads to gallium ion implantation in the patterned structure i.e. implanted metal atoms in the dielectric supporting beams. Also, structural imperfections and surface roughness of the milled metallic blocks cause scattering of plasmons, which reduce the excitation strength of the resonances [91]. Surface roughness can be caused by re-deposition of a portion of the sputtered material leading to distortions of the local geometry.

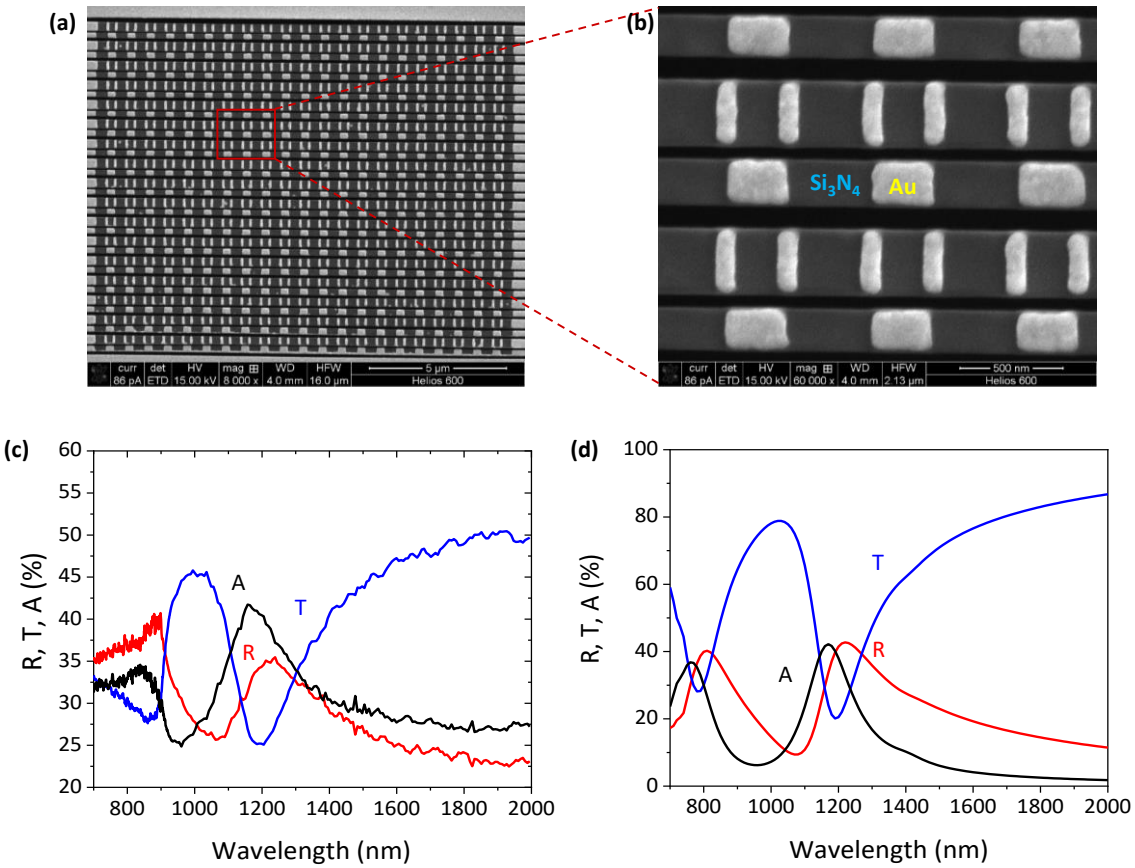

Figure 3.4 Fabrication and characterization of nanomechanical metamaterials. (a) SEM image of a plasmonic nanomechanical metamaterial array. (b) Magnified view of the array. (c) Measured and (d) simulated reflection R, transmission T and absorption A spectra of the plasmonic metamaterial for light polarized along the Si_3N_4 beams.

Successful fabrication of such structures is not without challenges. First of all, the optimum Ga^+ ion dosage (in mC/cm^2) for milling through the membrane in order to form the supporting Si_3N_4 beams (Figure 3.3 (c)) has to be determined. One cannot simply use a relatively high dosage as this would end up milling the surrounding gold bars too. The dosage has to be high enough to mill through the material while leaving the Au bars as intact as possible. For the sample of Figure 3.4, a Ga^+ ion dose of 5.5 mC/cm^2 was selected for milling of the Au layer and 17.5 mC/cm^2 for milling through the Au/Si_3N_4 bilayer. However, milling of material at the edges of the gold bars is unavoidable. Therefore, the dimensions of the array's unit cell have to be adjusted in order to account for that Au removal. Another major challenge in fabricating structures out of free-standing

membranes is the release of membrane stresses during milling. The membrane can locally deform resulting in deviations in the dimensions of unit cells. During sample fabrication it was found that near the edges of the membrane, close to the Si frame, this effect was less pronounced, resulting in better fabrication results. Figure 3.5 shows examples of such challenges affecting earlier fabrication attempts.

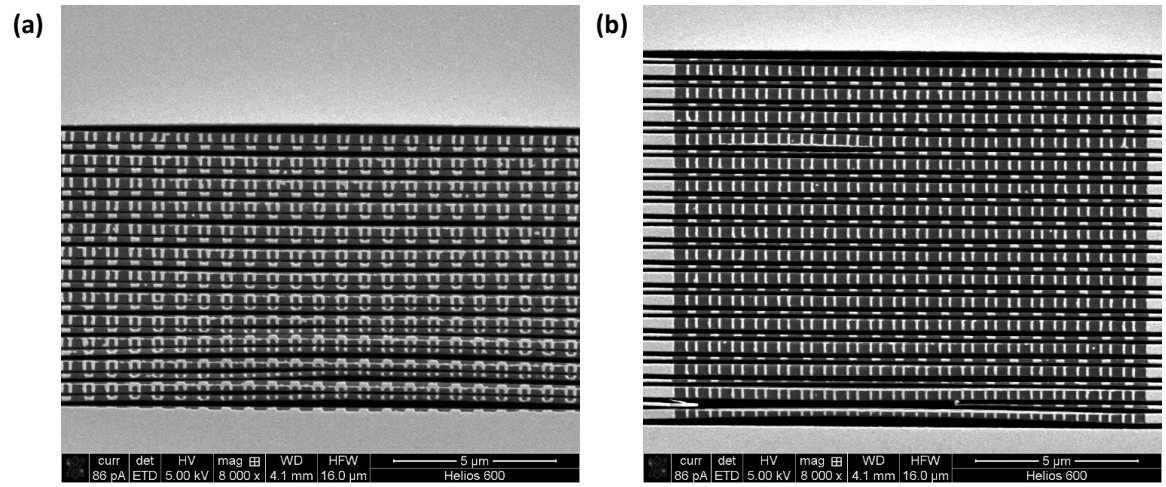

Figure 3.5 Unsuccessful fabrication attempts. (a) Arrays fabricated using a low dosage, not enough to mill through the Au/Si_3N_4 bilayer everywhere. (b) Inconsistencies in unit cell dimensions due to membrane deformations during milling.

3.3 Modulation of optical properties of nanomechanical metamaterials due to thermal motion

Thermomechanical fluctuations of a component's position $z(t)$ are transduced to fluctuations of intensity of light scattered on the component, $\delta I(t) = \frac{\partial \mu(z,\lambda)}{\partial z} \cdot I_0 \cdot \delta z(t)$, where I_0 and $I = \mu(z,\lambda) I_0$ are the intensities of the incident and scattered light, and $\mu(z,\lambda)$ is, generally, a nonlinear function of the component's displacement *z* and wavelength λ. In accordance with Equations (2.28), (2.29) the scattered light amplitude spectral density $s(f)$ resulting from small thermomechanical fluctuations in position $\delta z(t)$ is (considering that the amplitude spectral density is the square root of power spectral density $s(f) = \sqrt{S_{zz}(f)}$)

$$s(f) = \frac{\delta I}{\sqrt{\delta f}} = \left(\frac{\partial \mu(z,\lambda)}{\partial z}\bigg|_{z=0} \cdot I_0 \right) \times \sqrt{\frac{k_B T f_0}{2\pi^3 m_{\text{eff}} Q[(f_0^2 - f^2)^2 + (f f_0/Q)^2]}} \qquad (3.1)$$

where δf is the bandwidth. In a metamaterial, the same formula will describe the spectra of fluctuations of the intensity of light reflected I^r and transmitted I^t through the metamaterial as illustrated in Figure 3.6. Fluctuations $s^{r,t}$ of the metamaterial's reflectance/transmittance correspond to the ratio between the amplitudes of fluctuating and non-fluctuating components of

the transmitted/reflected light, that is Equation (3.1) divided by the incident intensity I_0 and optical reflectance/transmittance of the metamaterial without displacement, $\mu_0^{r,t}(\lambda) = \mu^{r,t}(0,\lambda)$.

$$s^{r,t}(f) = \frac{\delta I^{r,t}/I^{r,t}}{\sqrt{\delta f}} = \frac{1}{\mu_0^{r,t}(\lambda)} \times \left.\frac{\partial \mu^{r,t}(z,\lambda)}{\partial z}\right|_{z=0} \times \sqrt{\frac{k_B T f_0}{2\pi^3 m_{\text{eff}} Q[(f_0^2 - f^2)^2 + (f f_0/Q)^2]}} \tag{3.2}$$

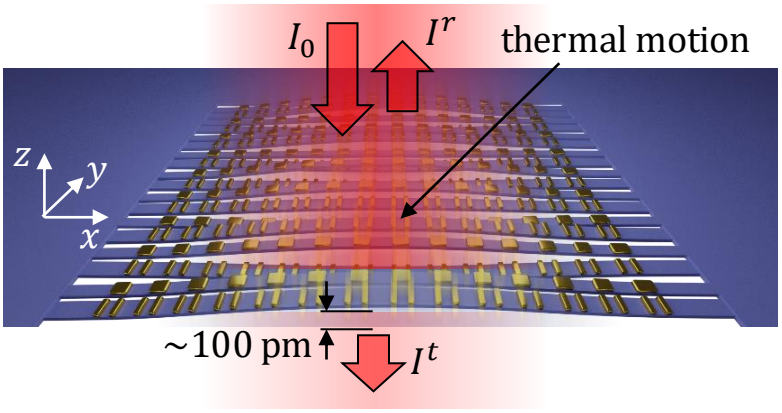

Figure 3.6 Thermal fluctuations of optical properties of a nanomechanical metamaterial.

At the mechanical resonance, $f = f_0$, this modulation depth spectral density reaches a peak value of

$$s^{r,t}(f_0) = \frac{1}{\mu_0^{r,t}(\lambda)} \times \left.\frac{\partial \mu^{r,t}(z,\lambda)}{\partial z}\right|_{z=0} \times \sqrt{\frac{k_B T\, Q}{2\pi^3 m_{\text{eff}} f_0^3}} \tag{3.3}$$

Reflectance/transmittance fluctuations over a range of mechanical frequencies can be calculated by integration over the power spectral density of the fluctuations

$$\begin{aligned} \delta I^{r,t}/I^{r,t} &= \sqrt{\int \left(S^{r,t}(f)\right)^2 df} \\ &= \frac{1}{\mu_0^{r,t}(\lambda)} \times \left.\frac{\partial \mu^{r,t}(z,\lambda)}{\partial z}\right|_{z=0} \times \sqrt{\frac{k_B T}{2\pi^3 m_{\text{eff}}}} \sqrt{\int \frac{f_0/Q}{\left(f_0^2 - f^2\right)^2 + \left(f f_0/Q\right)^2} df} \end{aligned} \tag{3.4}$$

Integration from 0 to ∞, or at least over the whole resonance, gives the root-mean-square (RMS) fluctuations

$$\delta I_{rms}^{r,t}/I^{r,t} = \frac{1}{\mu_0^{r,t}(\lambda)} \times \left.\frac{\partial \mu^{r,t}(z,\lambda)}{\partial z}\right|_{z=0} \times \sqrt{\frac{k_B T}{4\pi^2 m_{\text{eff}} f_0^2}} \tag{3.5}$$

where the final term corresponds to the RMS beam displacement, as in Equation (2.20), of

$$\delta z_{rms} = \sqrt{\frac{k_B T}{4\pi^2 m_{\text{eff}} f_0^2}} \tag{3.6}$$

From here it is apparent that fluctuations of transmission and reflection will be largest at high temperatures, in metamaterials constructed from very light (low m_{eff}) building blocks, and at optical frequencies where transmission and reflection depend strongly on displacements of said building blocks. Largest fluctuations over a narrow spectral range δf will be seen at high quality mechanical resonances, see Equation (3.3). As such, thermal fluctuations of optical properties should be strongest in highly optically dispersive nano-opto-mechanical metamaterials.

Assuming metamaterial beams, such as those shown by Figure 3.6, with an effective mass m_{eff} = 1 pg and mechanical quality factor of Q = 1000 moving at a damped frequency f_0 = 2 MHz, and a typical change in optical properties with beam displacement of $\partial\mu/(\mu_0\partial z) \sim 1$ %/nm, one may expect to observe an RMS thermomechanical displacement amplitude of $\delta z_{rms} = 160$ pm at the centre of the beams at room temperature, resulting in a 0.16% RMS fluctuations of optical properties. At the mechanical resonance, the corresponding spectral densities of displacement and optical property modulation reach peak values of 3 pm/$\sqrt{\text{Hz}}$ and 3 × 10^{-5}/$\sqrt{\text{Hz}}$, respectively.

Thus, in nanomechanical metamaterials, thermal fluctuations are transduced to fluctuations of optical properties that determine the functional noise floor and dynamic range of nanomechanical photonic metadevices. At the same time, observation of the spectra of thermal oscillations will give direct access to the resonant frequencies of natural mechanical modes at which the metamaterial will be most responsive to external stimuli. This information on fluctuation and responsivity of the mechanical sub-system can help in the design of highly efficient metadevices.

3.3.1 Optical properties of nanomechanical metamaterials

The plasmonic metamaterial used for the detection of thermal motion was fabricated based on the geometric parameters introduced in Section 2.2 (also shown in Figure 3.7 (a)). The structure consists of silicon nitride beams of alternate width (230 nm for the narrow and 280 nm for the wide beam) supporting plasmonic resonators with a periodicity of 800 nm. Here, the horizontal and the pair of vertical gold bars are separated by a distance of 100 nm. In total, the fabricated structure, seen in the SEM image of Figure 3.7 (b), consists of 30 mechanical resonators.

Measured and simulated reflection, transmission and absorption of the structure for incident light polarized parallel to the silicon nitride beams can be seen in Figure 3.8 (a), (b). The measurement was performed in a CRAIC microspectrophotometer using an aperture of 10 µm. Details regarding the microspectrophotometer operation can be found in Appendix B. For the

simulated optical properties, a single unit cell was simulated using a 3D finite element Maxwell solver (COMSOL 5.3a) with periodic boundary conditions. The array was excited by a normally

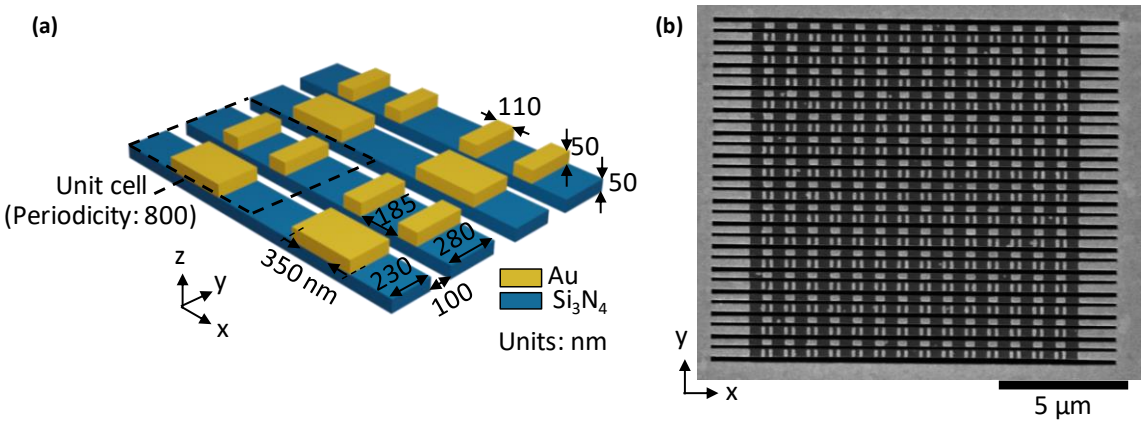

Figure 3.7 Plasmonic nanomechanical metamaterial. (a) Structure and (b) SEM image of the plasmonic metamaterial used for detection of fluctuations of optical properties due to thermal motion.

incident plane wave. A Drude-Lorentz model with three oscillators [92, 93] was used to model the electric permittivity of gold with a plasma frequency of ω_p = 1.365 x 10^{16} rad/s and a damping constant Γ_p = 3.18 x 10^{14} rad/s. The damping constant used in the model is about three times larger than in bulk gold in order to account for plasmon scattering due to gallium ion implantation and surface structure imperfections [59, 92]. Si_3N_4 was assumed to be lossless with a refractive index of 2 [93]. The simulations reveal that the structure supports a Fano-type resonance [57-60, 94-98] based upon interference between a "bright" dipole mode excited in the horizontal gold bars and an antisymmetric, "dark" magnetic mode induced in the pair of smaller bars. This interaction is illustrated in the inset of Figure 3.8 (b) which shows the E_z field distribution at 10 nm above the plasmonic bars at the measurement wavelength of 1310 nm. The optical properties of the metamaterial are sensitive to motion around its optical resonances, whose strength changes significantly upon beam displacement due to the coupling between the plasmonic elements. Figure 3.8 (c) shows the simulated relative reflectivity, $\Delta R/R_0$ of the structure for displacement of the narrow beams with respect to the wide in the out-of-plane direction (z-direction). $\Delta R/R_0$ corresponds to the quantity $\partial\mu/\mu_0$ for displacements ∂z in Equations (3.2)-(3.5). The simulations were performed by displacing the narrow silicon nitride beam along with the horizontal gold bar, up to 40 nm in steps of 10 nm. At the measurement wavelength of 1310 nm the reflectivity of the structure has a linear dependence on the displacement amplitude (inset of Figure 3.8 (c)), meaning that $\frac{\partial \mu^r}{\partial z}$ is constant. From the linear fit, a value of $\partial\mu/(\mu_0\partial z)$=0.275%/nm for the structure's reflectivity modulation per nm of displacement is extracted.

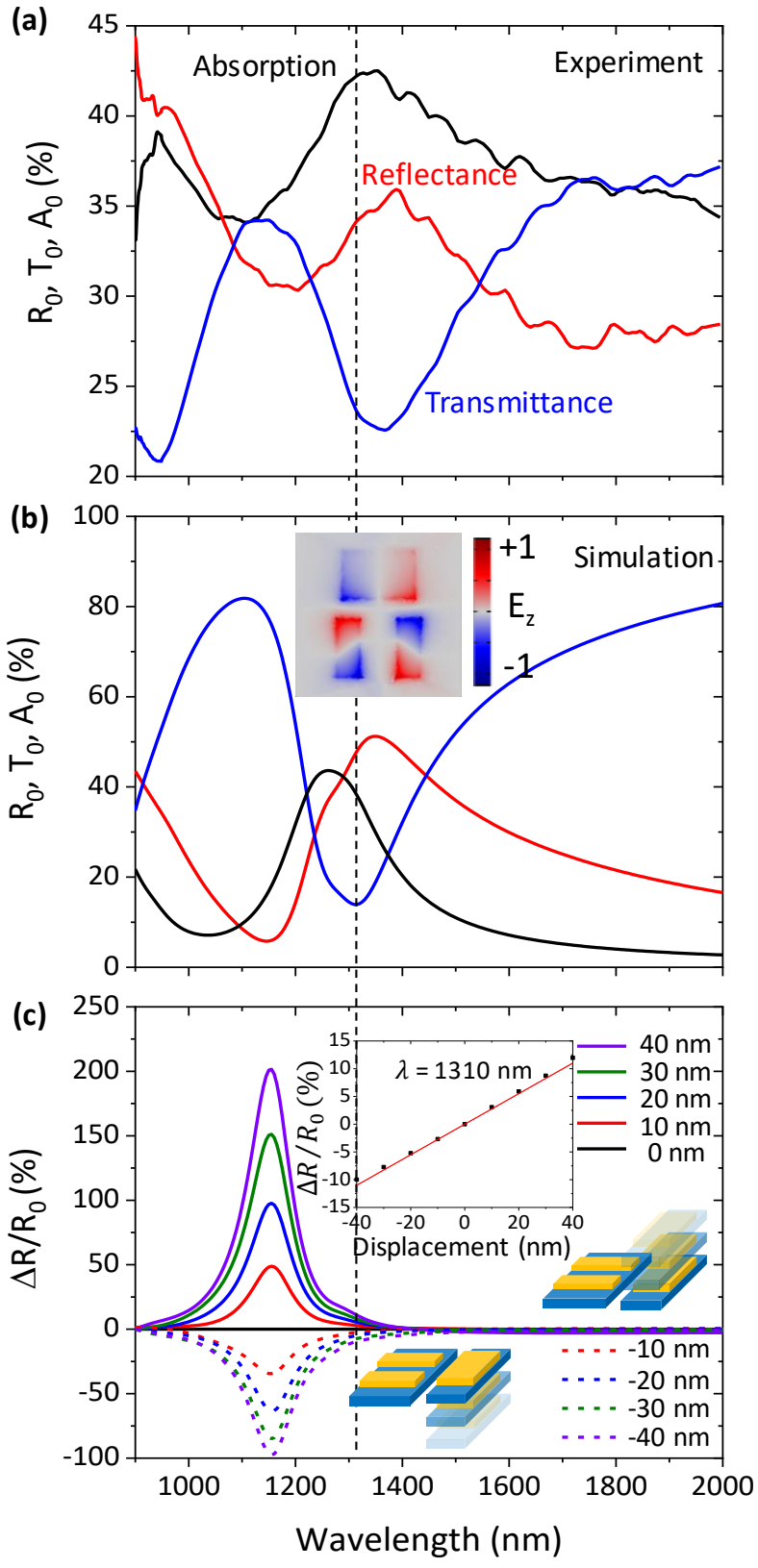

Figure 3.8 Optical properties and displacement sensitivity of the nanomechanical metamaterial. (a) Measured and (b) simulated reflection, transmission and absorption of the nanomechanical metamaterial. The dashed line indicates the measurement wavelength of 1310 nm. The inset in (b) shows the E_z field distribution 10 nm above the gold bars for illumination at 1310 nm wavelength. (c) Relative reflectivity modulation of the array for relative displacement of neighbouring beams along z at different levels of displacement. Positive displacement corresponds to movement of narrower beams along *+z* relative to wider beams. The inset graph shows the dependence of $\Delta R/R_0$ on displacement at the wavelength of 1310 nm. All results are for light polarized parallel to the beams (*x*-polarized).

3.3.2 Detection of thermal motion in nanomechanical metamaterials

To detect the metamaterial's reflectivity fluctuations arising from oscillations of its mechanical components, the sample was placed in the vacuum chamber and pumped down to a pressure of around 4 x 10^{-3} mbar to reduce air damping. A 1310 nm laser beam with a power of 48 μW was directed towards the centre of the structure and the reflected light was directed to a photodetector, see Section 3.1. Figure 3.9 presents the measured PSD spectrum recorded with a spectrometer (black line) together with the noise floor signal i.e. with the laser turned off (red line). The measurement bandwidth here was 53 Hz. For recording of each spectrum an averaging of 100 was selected. Thermomechanical oscillations of the metamaterial's beams are revealed as sharp peaks in the frequency spectrum, around 2.5 MHz. Peaks that appear in both curves are due to the detection system, considering that they do not depend on laser illumination.

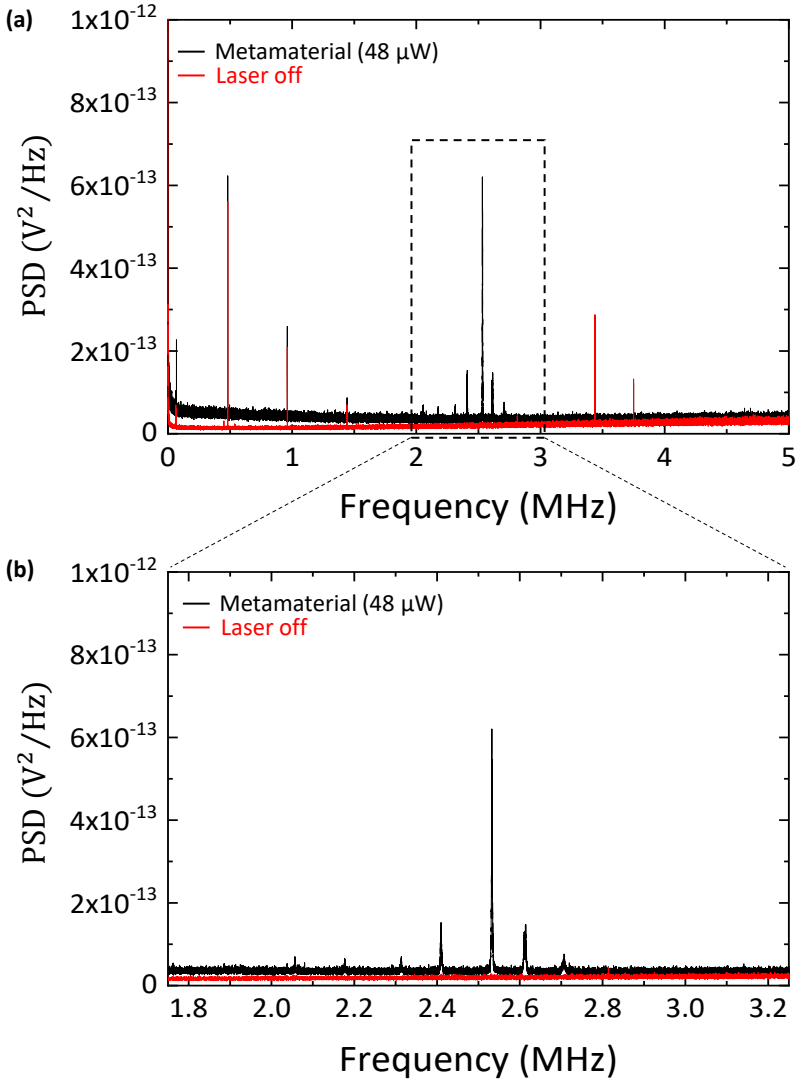

Figure 3.9 PSD spectrum of the nanomechanical metamaterial. (a) Signal arising from the light reflected by the metamaterial array when probed by a 1310 nm laser beam with a power of 48 μW shown as a black line. The red line corresponds to a measurement taken with the laser source turned off. (b) Zoomed-in view of (a).

The above PSD graphs can then be converted to relative spectral density of reflectance modulation $s^{r,t}(f) = \frac{\delta I^{r,t}/I^{r,t}}{\sqrt{\delta f}}$ in the metamaterial. This is done by using the PSD signals at zero frequency (DC) for the two measurements (with the laser on at 48 μW and off) as the voltage difference between them corresponds to 100% reflectivity change. The spectrum of the structure's reflectivity fluctuations s^r, can be seen in Figure 3.10 (a).

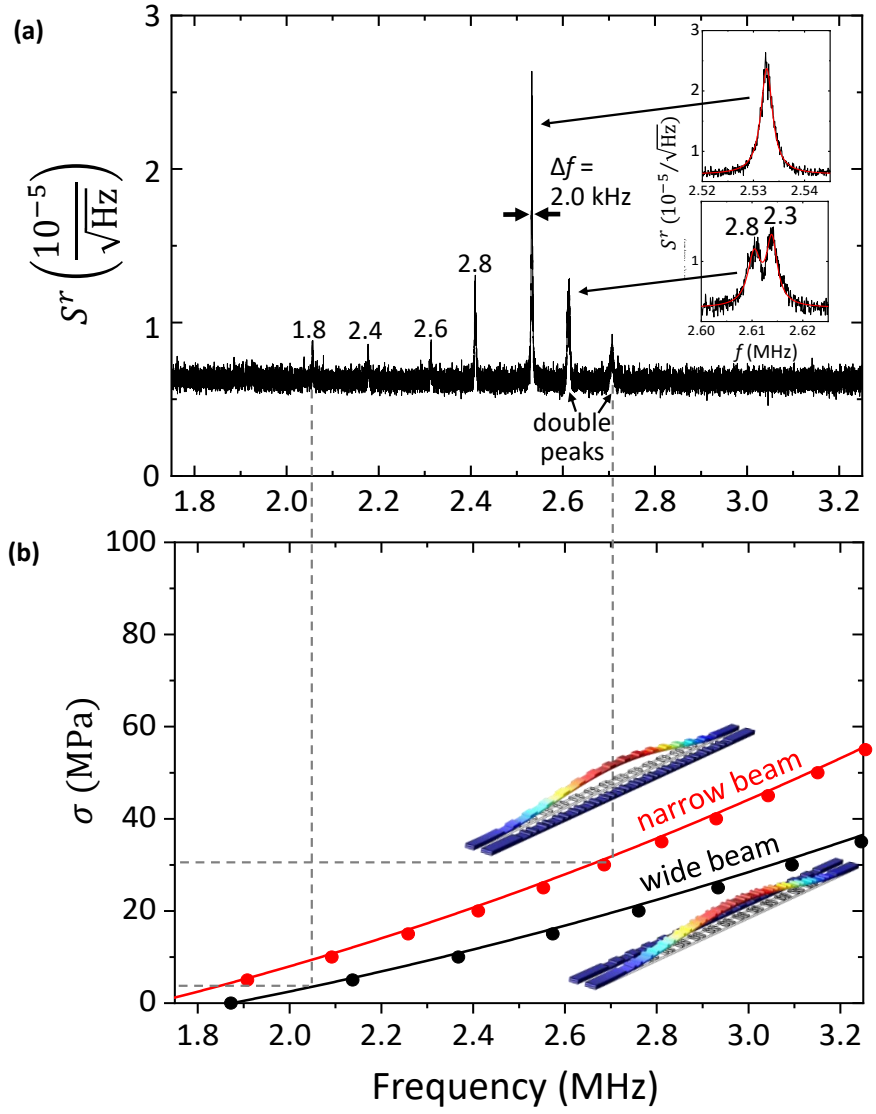

Figure 3.10 Thermal fluctuation of the reflectivity of the nanomechanical metamaterial. (a) Measured spectral density of reflectance modulation s^r by the plasmonic metamaterial. Resonant peak widths Δ*f* are labelled in kHz and insets show enlarged examples of single (double) resonant peaks with single (double) Lorentzian fits. (b) Frequencies of the fundamental out-of-plane resonances of the plasmonic metamaterial beams for different levels of tensile stress σ. Simulated resonance frequencies of the nanostructured beams (data points) are shown with a fit according to Equation (2.14) (lines).

The range of sharp peaks observed are linked to the frequencies of thermal movements of the silicon nitride beams at their natural frequencies in the megahertz range. We see an isolated group of several peaks with Lorentzian profiles that overlap in the case of closely-spaced resonances (insets of Figure 3.10 (a)) with an average quality factor of around 1000. The Lorentzian line shape indicates that different peaks are related to different beams within the structure. Thus,

the collective mechanical response of the metamaterial is the sum of the individual responses of its mechanical elements. Considering the geometric parameters of Figure 2.3 it is clear that the structure's mechanical resonances are detected at significantly higher frequencies than the results presented in Figure 2.4 (1.7 MHz and 1.87 MHz for the narrower and wider beam respectively), indicating the presence of tensile stress in the beams. Table 3.1 summarizes the simulated eigenfrequencies of the first out-of-plane mechanical modes of the two beams for zero stress along with their effective masses. Variations between the resonance frequencies of individual, nominally identical beams are most likely caused by disparities in beam tension across the sample as a consequence of the fabrication procedure and initial stress in the membrane, rather than variations of their physical dimensions. These variations in tensile stress across the metamaterial, leading to the spread of individual peak frequencies, can be evaluated from Euler-Bernoulli beam theory, see Equation (2.14). The mechanical eigenfrequencies of the metamaterial beams under stress were obtained by simulating the structure of Figure 2.3 for different values of tensile stress in the silicon nitride layer, along the length of the beams.

Table 3.1 Fundamental mechanical eigenfrequencies and effective masses of the plasmonic metamaterial without tensile stress.

	Narrow beam	**Wide beam**
Mechanical eigenfrequency, f_0	1.7 MHz	1.87 MHz
Effective mass, m_{eff}	0.69 pg	0.6 pg

Figure 3.10 (b) illustrating the relationship between stress and fundamental frequency for the two types of metamaterial beams, shows that the observed variation of the fundamental mechanical resonance frequencies of the beams are explainable by tensile stress variations from beam to beam of around 30 MPa. Inhomogeneous illumination of several beams within the optical spot profile can also contribute to inhomogeneous shifts of beam frequencies through thermal expansion of the beam length, which reduces stress: $\sigma = \sigma_0 - \alpha E \langle \Delta T \rangle$, where σ_0 is the initial tensile stress, α the thermal expansion coefficient of the material and $\langle \Delta T \rangle$ the average temperature change. This temperature dependence of the internal stress will be discussed in more detail in Chapter 4.

To evaluate the root-mean-square of relative fluctuation of optical properties $\delta I^{r,t}_{\mathrm{RMS}} / I^{r,t}$ resulting from thermomechanical fluctuations we need to integrate, as shown by Equation (3.4), over the entire frequency range. If only fundamental mechanical modes of the metamaterial beams are taken into account, this integral can be approximated as $s_0\sqrt{N\Delta f}$, where N is the number of peaks/modes and s_0 and Δf are average amplitude and width of the peaks. From the

data presented in Figure 3.10 (a), we can evaluate that the level of reflection fluctuation is in the order of $\frac{\delta I^r_{\mathrm{RMS}}}{I^r} = 0.1\%$ at 1310 nm. This value could increase to about $\frac{\delta I^r_{\mathrm{RMS}}}{I^r} = 1.5\%$ at the plasmonic resonance where the reflectivity modulation per displacement is largest, see Figure 3.8 (c).

3.4 Conclusions

In conclusion, we can observe the natural vibrations of nanomechanical metamaterials as high-frequency time-domain fluctuations of their optical properties. Thermal oscillation of metamaterial structures modulates the relative position of their coupled optical resonators by a fraction of a nanometre, causing detectable intensity modulation of reflected light. This enables optical characterization of their mechanical resonances.

Chapter 4

Photothermal tuning of nanomechanical plasmonic metamaterials

Vibrations of micro- and nanostructures underpin NEMS/MEMS technology and applications such as mass detection [80, 99-102] and mass spectrometry [103-105], force sensing [106-108], temperature [109-111] and radiation [112-115] sensing and studies of nonlinear and coupled systems [116-118], amongst others. In nanomechanical metamaterials, such vibrations allow dynamic control over their optical properties [21]. Detection of the natural oscillations of such systems identifies the frequencies at which they might be driven, while control over the mechanical response can increase bandwidth, performance and operation modes. Temperature changes, either by environmental heating or through absorption of light, perturb a mechanical system through thermal expansion and thermal variations of its mechanical properties. In particular, beams and strings are highly responsive to environmental changes due to their frequency dependence on tensile stress [78, 110] and have led to the demonstration of temperature sensors [110, 111], photothermal spectroscopic techniques [105] and tuning of the frequency response of nanostructures [119]. Combination of such systems with plasmonic structures has been proposed for the realization of novel imaging [120] and parallel detection schemes [76] that can find application in gas sensing, mechanical mode mapping of nanostructures [121] as well as thermoplasmonics [122].

In this chapter, it is demonstrated that nanomechanical metamaterials are ideally suited not only for detection of their natural frequencies but also for tuning them simply by controlling the power of the illumination impinging on them. Heating of the metamaterial beams by light absorption shifts their mechanical resonances by 100s of kHz, achieved by μW levels of optical power. The same phenomenon was studied, independently, by my colleague Jinxiang Li, the studies were performed independently, using dedicated experimental setups with different types of metamaterials that were developed and fabricated independently. The experimental structure presented here consists of 2 beams supporting a row of plasmonic resonators. Section 4.1 describes the eigenfrequency dependence on stress and temperature for beam nanomechanical resonators analytically. Section 4.2 describes the optical properties of the structure while in Section 4.3 effective mechanical parameters of the metamaterial beams are derived that allow analytical description of the structures' mechanical resonances. In Section 4.4 the experimental results of tuning the mechanical eigenfrequencies of a two beam structure are presented. Absorption

induced mechanical frequency shifts detected optically allow not only detection of infrared light but also calculation of the structure's temperature increase. Section 4.5 discusses the use of our structure as a nanomechanical bolometer. In Section 4.6 the concept of a nanomechanical bolometer is expanded in a metamaterial array that can support multiple mechanical resonances that can detect irradiation with subwavelength resolution.

4.1 Thermal tuning of mechanical eigenfrequencies

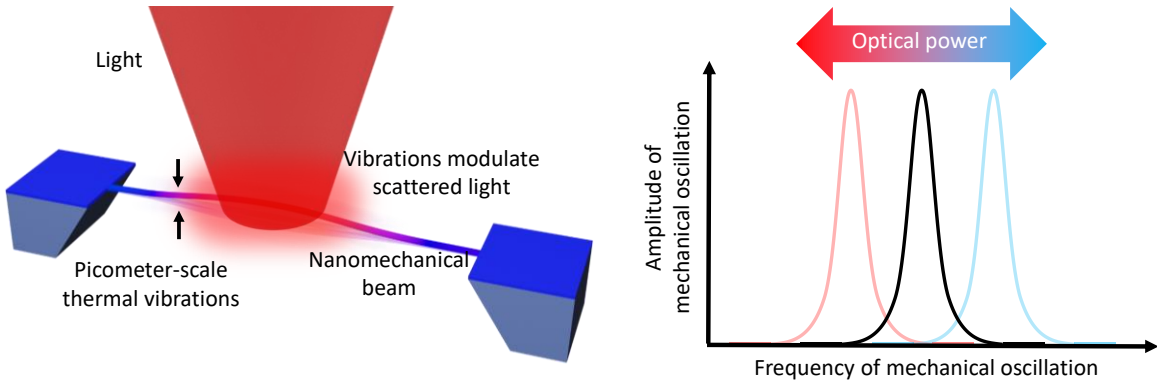

Figure 4.1 Concept of thermal tuning of mechanical eigenfrequencies. Incident light heats a nanomechanical oscillator, causing a shift of its mechanical resonance frequency. The resonance may be detected as modulation of light, enabling the detection of the incident power from the resonance frequency shift.

Fabrication of beam resonators from a pre-stressed membrane results in beams with residual tensile stress. Illumination of such beams increases their temperature through absorption of light. If a beam resonator, such as the doubly-clamped beams described in Section 2.2, is subjected to an average temperature change $\langle \Delta T \rangle$ induced by radiation absorption and assuming that its endpoints do not move, its internal stress will be modified by thermal expansion according to [78, 119]

$$\sigma = \sigma_0 - aE\langle \Delta T \rangle \tag{4.1}$$

where σ is the stress at the increased temperature T, σ_0 is the initial stress at the initial temperature T_0, α is the thermal expansion coefficient, E is its Young's modulus and $\langle \Delta T \rangle = \frac{T-T_0}{2}$. Therefore, heating modifies the stress-dependent eigenfrequencies of the beam. We repeat here Equation (2.14)

$$f_1(\sigma) = 1.03\frac{h}{L^2}\sqrt{\frac{E}{\rho}}\sqrt{1+\frac{\sigma L^2}{3.4Et^2}} \tag{4.2}$$

This concept is illustrated in Figure 4.1 where a light beam incident on a beam resonator shifts its mechanical eigenfrequency depending on the power absorbed by the resonator. Combining Equations (4.1) (4.2), the relative frequency shift $\delta f = \big(f_1(\sigma) - f_1(\sigma_0)\big)/f_1(\sigma_0)$ in the limit of small temperature changes can be approximated as

$$\delta f \approx -\frac{1}{2}\left(\frac{aEL^2\langle\Delta T\rangle}{3.4Et^2+\sigma_0 L^2}\right) \tag{4.3}$$

This can be simplified to

$$\delta f \approx -\beta\langle\Delta T\rangle \tag{4.4}$$

where

$$\beta = \frac{\alpha EL^2}{6.8Et^2+2\sigma_0 L^2} \tag{4.5}$$

Therefore, the relative frequency shift increases with increased temperature, thermal expansion coefficient and length while it decreases for increased thickness and initial tensile stress σ_0.

At this point it is useful to study the effect of heating in a one dimensional structure such as a string to give insight as to what affects the temperature increase of nanomechanical metamaterial nanostructures. Assuming a string of length L, illuminated at its central part, the energy absorbed, P_{abs}, in the centre is in equilibrium with the heat flow through the material out into the supports that have a constant temperature T_0. Following [78], the temperature distribution is described as

$$T(x) = T_0 + 2(T_{max}-T_0)\frac{x}{L} \tag{4.6}$$

for $0 \le x \le \frac{L}{2}$, where T_{max} is the temperature at the centre. The heat flux, Q_T through one half of the structure can be described by the one-dimensional Fourier's law as

$$Q_T = -\kappa A\frac{\partial T}{\partial x} \tag{4.7}$$

where A is the string's cross section and κ is the material's thermal conductivity. The total power absorbed in the string must be equal to the total energy flowing from the centre to the supports

$$P_{abs} = 2|Q_T| \tag{4.8}$$

Combination with Equations (4.6) and (4.7) gives

$$\Delta T_{max} = T_{max} - T_0 = \frac{P_{abs}L}{4\kappa A} \tag{4.9}$$

The average temperature increase of the structure becomes

$$\langle\Delta T\rangle = \frac{\Delta T_{max}}{2} = \frac{P_{abs}L}{8\kappa A} \tag{4.10}$$

From here it can be seen the temperature increase of an illuminated string-like structure will be higher for increased absorbed power and a long, slender geometry with low thermal conductivity

κ. Nanomechanical metamaterials provide a means of tailoring optical absorption (and therefore their temperature increase) by virtue of the geometric characteristics of their optical resonators.

4.2 Metamaterial optical properties

As already described in Chapter 3, the combination of beam structures with optically resonant elements results in nanomechanical metamaterial structures supporting optical and mechanical resonances in a single nm-thick structure. Such structures can have absorption maxima near their optical resonances providing spectral selectivity while their mechanical resonances can be characterized by exploiting that, at non-zero temperatures, the natural vibration of mechanical oscillators will be driven by thermal energy.

To demonstrate thermo-optical control over the fundamental mechanical resonances of the metamaterial beams, a mechanical system consisting of two Si_3N_4 beams decorated with gold, Π-shaped optical resonators that support a Fano-type resonance was used. Figure 4.2 (a) contains segments of two 250 nm wide silicon nitride micro-beams, one supporting a single, large plasmonic dipole resonator (single dipole beam) and the other a pair of smaller dipole plasmonic resonators (double dipole beam). The silicon nitride beams and the gold structures are 50 nm thick, each. Figure 4.2 (b) shows the simulated optical response of an array of such unit cells with a periodicity of 800 nm, for normally incident light polarized along the silicon nitride beams, revealing an absorption resonance at about 1250 nm wavelength. Here, the structure operates in a “bright”-“dark” mode configuration where a “bright” dipole mode is directly excited by the incident radiation and a “dark” quadrupole mode is induced by the dipole. The measurement wavelength of 1310 nm, indicated by the dashed line, is close to the peak of the absorption resonance ensuring large absorption, and therefore heating, of the nanomechanical structures for thermo-optical control of their fundamental resonances. High reflectivity at this wavelength ensures strong scattering of the incident radiation that can be picked up to detect reflectivity fluctuations of the structure due to the thermal motion of its components. The motion of one beam relative to the other will change the coupling between the plasmonic elements, which leads to a change in their optical properties as illustrated in Figure 4.2 (c). While the structure exhibits the same qualitative behaviour as the one considered in Chapter 3, its geometry and optical properties are slightly different and the simulations have been adjusted to match the geometry of the fabricated structure.

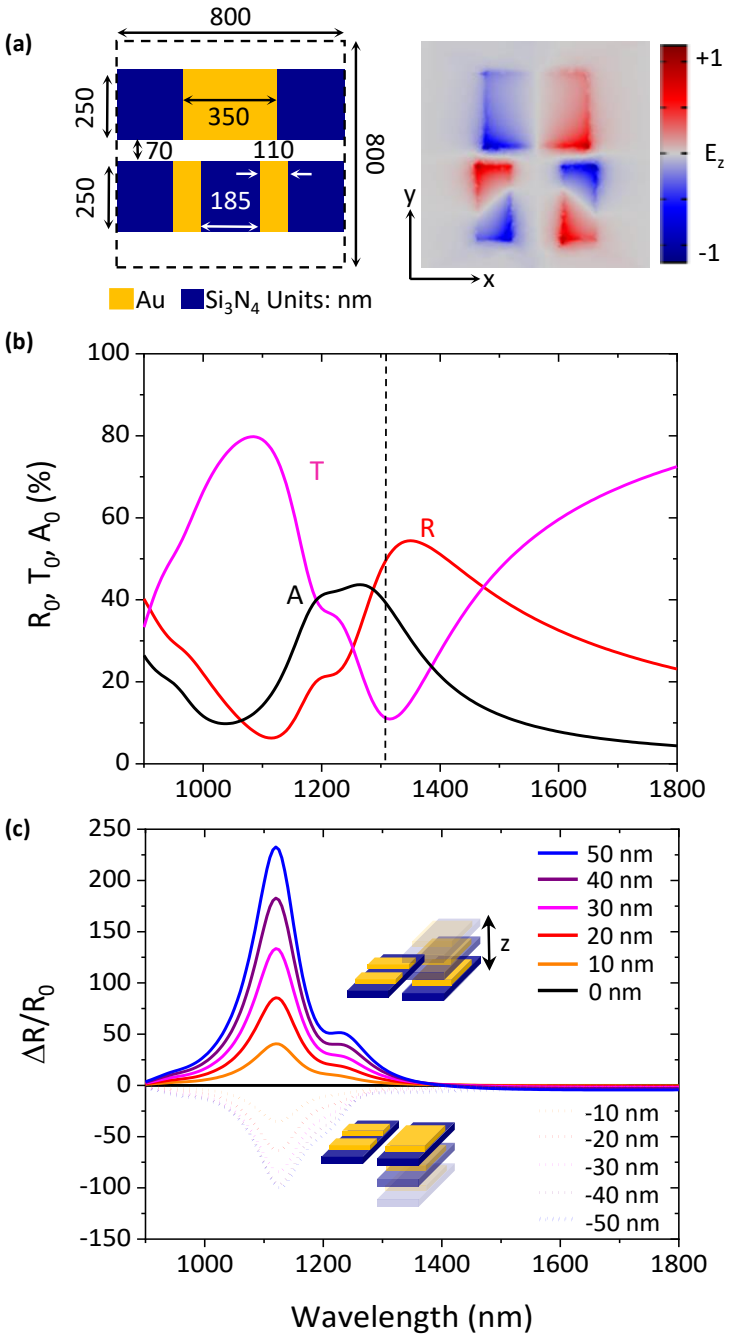

Figure 4.2 Optical properties of the double beam optical nano-mechanical system. (a) Left panel: Schematic of the unit cell dimensions. Right panel: E_z field distribution 10 nm above the gold bars at the measurement wavelength of 1310 nm for incident light polarized parallel to the Si_3N_4 beams. (b) Simulated optical properties of the structure for light polarized parallel to the Si_3N_4 beams. (c) Relative reflectivity modulation for relative displacement of neighbouring beams along z at different levels of displacement. All simulations consider a 2D period array containing many beams. Positive displacement corresponds to movement of the single dipole beams along *+z*, relative to wider beams.

4.3 Sample and effective material parameters

As demonstrated in Section 3.3 differential motion of the beams of a nanomechanical metamaterial array leads to the emergence of a number of peaks in the PSD spectra upon illumination, making it challenging to identify and link them to particular mechanical resonators. To overcome this, a simpler, two beam system was fabricated allowing accurate detection and

characterization of the mechanical characteristics of the system. Together, the two silicon nitride beams support a row of 14 optical resonators. The beams are 16 micrometres long and were fabricated by focused ion beam milling of a 50 nm thick, low stress (< 250 MPa) silicon nitride membrane coated with a thermally evaporated layer of 50 nm thick gold (Figure 4.3 (a)). For more details on fabrication see Section 3.2 and Appendix A. Since our structure consists of beams with varied cross-sections, we perform finite element method simulations to calculate the mechanical eigenfrequencies and effective mechanical parameters of the strings (COMSOL 5.3a). Without initial tensile stress, the simulated mechanical eigenfrequencies of the fundamental out-of-plane mode of the single and double dipole beams are f_1 =1.481 and 1.647 MHz, respectively.

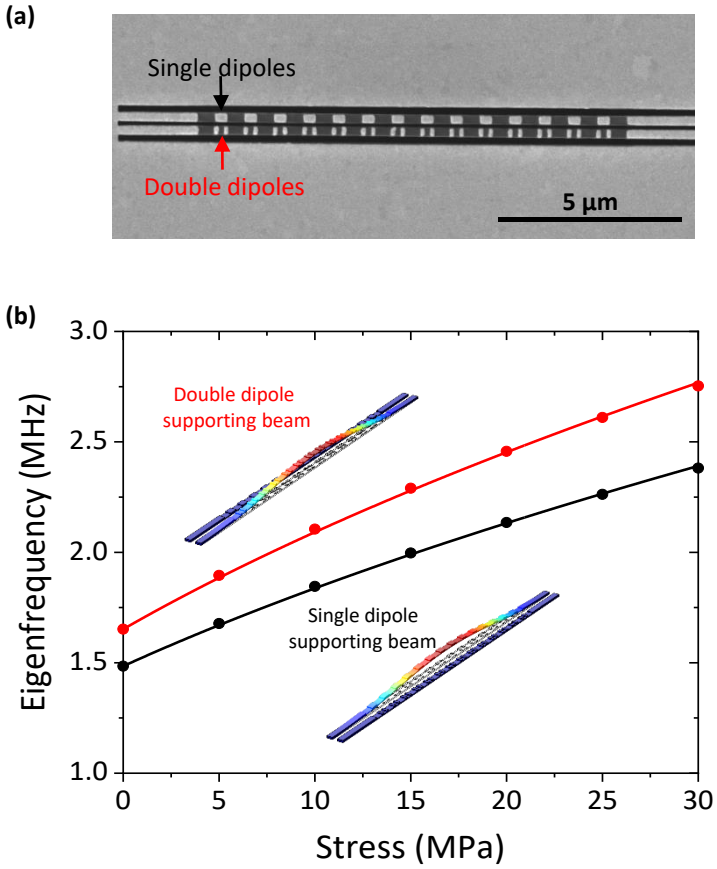

Figure 4.3 Stress-tuning of nanomechanical beam resonators. (a) SEM image of the fabricated two beam nano-optomechanical system. (b) Simulated mechanical eigenfrequencies of two silicon nitride beams that jointly support 14 plasmonic unit cells, for different values of tensile stress (dots). Lines represent fittings with the stress dependent mechanical eigenfrequency according to Equation (4.2). Insets show finite element method simulations of the respective mechanical modes.

Tensile stress increases the mechanical resonance frequencies of the beams, as illustrated by Figure 4.3 (b) for tensile stress up to 30 MPa. In order to describe the stress-dependent mechanical eigenfrequencies of the structure analytically, we take each beam's thickness to be its average thickness and fit the simulations with Equation (4.2), arriving at the effective beam parameters (E_{eff}, ρ_{eff} and t_{eff}) given by Table 4.2. The average thickness was calculated based on the

percentage of gold coverage of each beam which was extracted from the SEM image. For the single dipole beam and gold coverage of 57.8%, an effective thickness of 79 nm was calculated while for the double dipole beam the gold coverage was 46.4% resulting in a lower effective thickness of 73 nm. The effective thermal expansion coefficient α_{eff} of each beam was calculated as follows. For a bilayer beam consisting of equal parts Si_3N_4 and Au, its effective thermal expansion coefficient $\alpha_{eff,bilayer}$ is given by

$$\alpha_{eff,bilayer} = \frac{\alpha_{SiN}E_{SiN}+\alpha_{Au}E_{Au}}{E_{SiN}+E_{Au}} = 5.4 \times 10^{-6}\ \mathrm{K}^{-1} \quad (4.11)$$

where $\alpha_{SiN} = 2.8 \times 10^{-6}\ \mathrm{K}^{-1}$ and $\alpha_{Au} = 14.2 \times 10^{-6}\ \mathrm{K}^{-1}$ (Table 4.1). Taking the weighted average, the effective thermal expansion coefficient of each beam is calculated (Table 4.2).

Table 4.1 Thermal properties of silicon nitride and gold. [39, 123]

Material	Thermal expansion coeff. ($\boldsymbol{a}$)	Thermal conductivity ($\boldsymbol{\kappa}$)	Volumetric heat capacity ($\boldsymbol{c}$)
Si_3N_4	2.8 x 10^{-6} K^{-1}	2.5 $Wm^{-1}K^{-1}$	2.1 J cm^{-3} K^{-1}.
Au	14.2 x 10^{-6} K^{-1}	146 $Wm^{-1}K^{-1}$	2.5 J cm^{-3} K^{-1}

Table 4.2 Effective Young's modulus E_{eff}, density ρ_{eff}, thickness t_{eff}, thermal expansion coefficient α_{eff} and mass m_{eff} of the two metamaterial beams.

Parameters	Single dipole beam	Double dipole beam
$\boldsymbol{E}_{eff}$ (GPa)	227	235
$\boldsymbol{\rho}_{eff}$ (kg/m^3)	10410	7415
$\boldsymbol{t}_{eff}$ (nm)	79	73
$\boldsymbol{\alpha}_{eff}$ (1/K)	4.3 × 10^{-6}	4.0 × 10^{-6}
$\mathbf{m}_{eff}$ (pg)	0.82	0.58

4.4 Tuning of mechanical resonances of metamaterial beams with light

The two beams oscillate at their natural frequencies due to thermal energy. These mechanical vibrations were characterized in a vacuum chamber at a pressure of 4 x 10^{-3} mbar by measuring the resulting modulation of reflected light. Similarly to the optical measurement setup described in Section 3.1, a 1310 nm wavelength CW laser beam polarized parallel to the silicon nitride beams was focused on the sample with an objective of 0.40 numerical aperture and the

reflected light was collected and guided to a photodiode (Figure 3.1). The full width at half maximum (FWHM) of the laser spot was 5 µm and the total optical power incident on the sample was varied between 3.5-70 µW. Considering the spot size and the 800 nm width of the unit cell that contains two beams, about 10% of the total incident power illuminates an individual metamaterial beam. The laser wavelength is close to the structure's plasmonic resonance (Figure 4.2 (b)), ensuring strong absorption for thermo-optical control of the fundamental resonances of the micro-beams. A spectrum analyser was used to record the optomechanically transduced signal. Measurements were taken at the centre of the structure and two peaks were detected around 1.5 MHz (single dipole beam) and 2 MHz (double dipole beams) at a few microwatts of laser power incident on each metamaterial beam (Figure 4.4). The measurements show the power spectral density of the reflected light as a function of frequency and laser power incident on each beam.

By fitting the experimental power spectral density curves with Equation (2.29) and following the procedure outlined in Section 2.3.1, we extract experimental RMS displacements (assuming room temperature) of 269 and 249 pm, at 7 µW illumination power per beam for the single and double dipole beams, respectively. These experimental RMS displacements are comparable to the theoretically expected room temperature RMS displacements of 274 and 255 pm according to Equation (3.6), based on the observed resonance frequencies and effective masses according to eigenmode simulations (Table 4.2). This confirms that the detected signal indeed arises from oscillations of the two micro-beams. Comparison of the observed PSD peaks to the background level indicates that the displacement sensitivity our experiments is about 2 pm/Hz$^{-1/2}$ at the highest incident laser power.

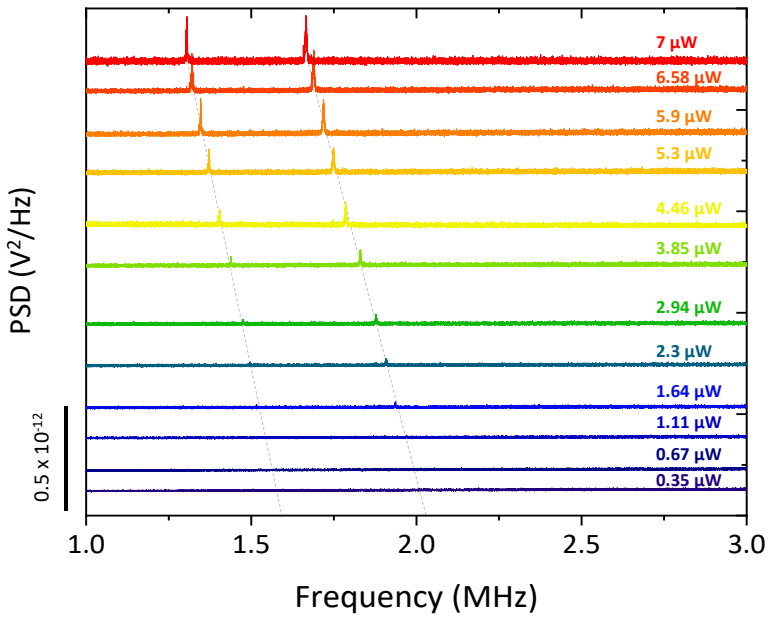

Figure 4.4 Power dependence of thermal vibrations of the metamaterial beam pair. (b) Thermomechanical spectra (power spectral density, PSD) of light reflected by the centre of the two beams for different levels of CW laser power. Inset values indicate the power incident on each nanomechanical beam.

For both mechanical resonances, increased incident power decreases the resonance frequency. This is an expected consequence of optical heating of the beams, leading to a stress reduction according to Equation (4.1) and a resonance frequency shift according to Equation (4.2). Figure 4.5 (a) shows the detected resonance frequencies of both beams as a function of incident laser power. The frequency positions were extracted from measured PSD curves for two cycles of optical heating and cooling of the sample. The observed power-dependence of the resonance frequency shift is linear. By performing a linear fit, we determine the resonant frequency, $f_1(\sigma_0)$, of the measured beams in the absence of thermal softening (stress reduction) due to laser illumination, at 0 µW incident laser power. Then, using Equation (4.2) and the effective beam parameters of Table 4.2, we calculate the tensile stress σ for different illumination power levels of the measured micro-beams (Figure 4.5 (b)). According to linear fits, the initial tensile stress σ_0 is 2.57 and 8.11 MPa for the single and double dipole beams, respectively. This analysis suggests that the stress in the single and double dipole beams becomes compressive above 2.8 and 6.5 µW of illumination power per beam, respectively. The thermo-optical shift of the resonance frequencies of the single and double dipole beams reaches δf = 16.8 and 19.5 % at 7 µW of incident laser power per beam, that is a shift of 2.4 and 2.8 %/µW, respectively.

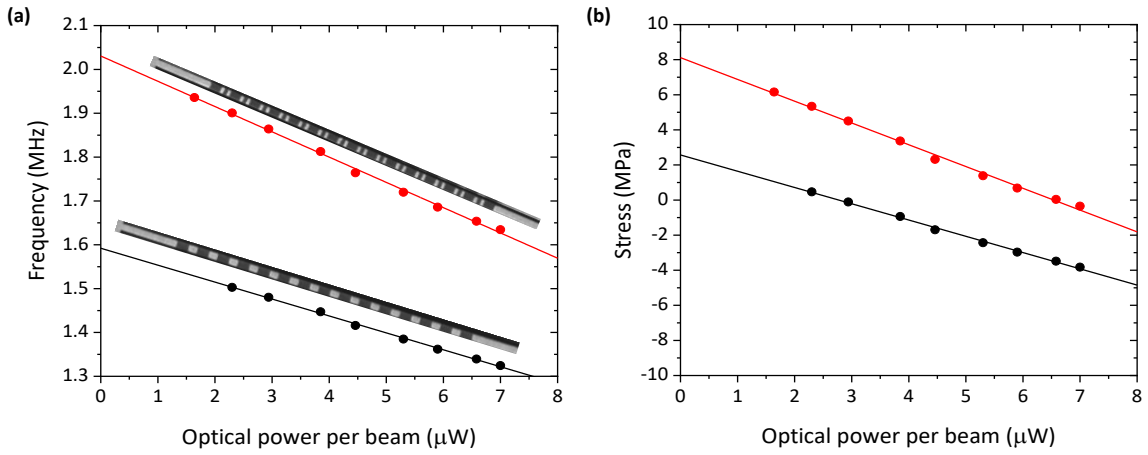

Figure 4.5 Optical control of mechanical resonances and stress. (a) Fundamental mechanical resonance frequencies as a function of optical power incident per beam. According to linear fits (lines), the mechanical eigenfrequencies without laser illumination are $f_0(\sigma_0)$ = 1.592 and 2.030 MHz for the single and double dipole beams. Insets show SEM images of the beams. (b) Calculated stress of the nanomechanical beams as a function of optical power incident per beam. Linear fits (lines) indicate the initial stress of σ_0= 2.57 and 8.11 MPa for the single and double dipole beams.

4.4.1 Temperature increase in the beams

The light-induced temperature increase of the beams is given by the observed eigenfrequency shift δf according to Equation (4.4). From here, we calculate the temperature increase in the beams for each level of incident optical power, see Figure 4.6 (a). Here, the effective thermal expansion coefficients of the beams are given by the weighted average of those for silicon

nitride and bilayer sections of the beams, see Table 4.2. According to this calculation, the natural frequencies of the single and double dipole beams shift by β = 2.3 and 1.9 $\%/\mathrm{K}$ and the beams reach average temperatures of $\langle \Delta T \rangle$ = 7.4 and 10.3 K above room temperature, respectively. The lower temperature of the single dipole beam is expected, as its more extensive gold coverage implies more efficient conductive cooling and thus a lower equilibrium temperature, see Equation (4.10).

Also, the spectral width of the resonances depends on the incident optical power. Figure 4.6 (b) shows the measured quality (Q) factors for both nanomechanical beams as a function of optical power where we observe Q-factor changes of up to 300%. The quality factors were calculated by fitting each peak with a Lorenz function to extract its position and FWHM. Increasing illumination levels leads to a decrease of the quality factor of the mechanical resonances from around 1000 at low power to 300-400 at 7 µW per beam. This may be due to dissipation dilution, where – at low intensity – the increased tensile stress in the nanomechanical resonators increases the stored vibrational energy relative to the structure's intrinsic losses, resulting in an increased quality factor [124-126]. Where a high quality factor is desired, the detrimental effect of high power laser illumination on the mechanical quality factors could be countered by using higher stress materials. Alternatively, further tuning of the internal stress could be achieved via mechanical stretching of the beams [127] or strain engineering [126]. Another approach that has been reported is tapering (reducing the width) of the edges of doubly-clamped beam resonators which leads to local stress enhancement and increased mechanical Q factors [128].

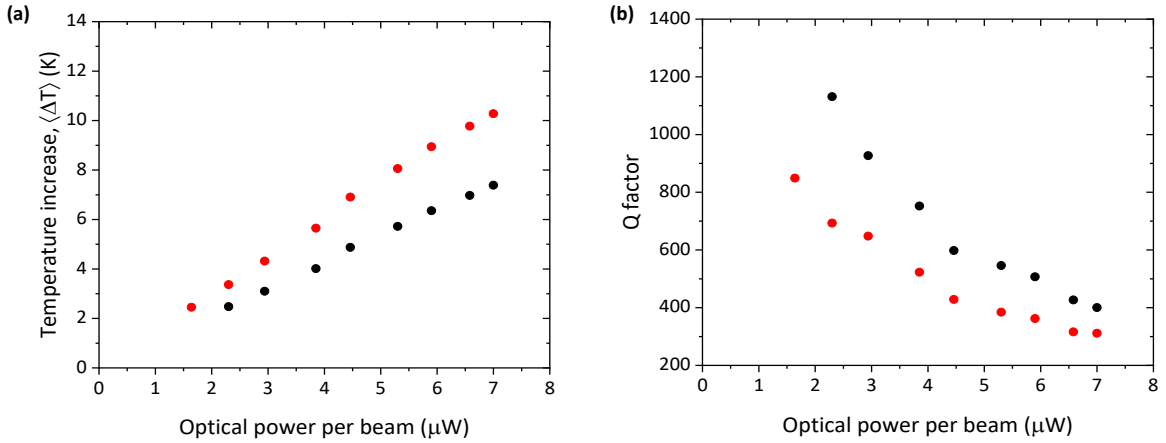

Figure 4.6 Temperature and quality factors of the metamaterial beams. (a) Average temperature increase and (b) mechanical Q factors of the fundamental nanomechanical resonances as a function of incident optical power.

Considering a quality factor of about 1000 at low power (Figure 4.6 (b)), a resonance shift of one resonance width arises from about 40 nW of optical power. Incident optical power can be determined from the resonance shift and given that the resonance frequency can be fitted with much less uncertainty than one peak width, this implies that the minimum detectable power is on

the order of a few nanowatts. The structure's use as a bolometer will be investigated further in Section 4.5.

4.4.2 Tuning of eigenfrequencies by ambient temperature changes

To further confirm the origin of the resonance frequency shift we performed thermomechanical measurements of the two beam system at fixed laser power and varying ambient temperature. Control of the ambient temperature is achieved through a heating stage placed inside a vacuum chamber. The temperature is increased from 20°C (room temperature) up to 120°C in steps of 10°C for fixed laser power incident per nanomechanical beam of 3.85 µW. Figure 4.7 shows that the resonance frequencies shift linearly with increasing temperature, up to 17% for the single dipole supporting beam at 110°C and 6% at 80°C for the double dipole supporting beam. Further increase of the ambient temperature results in a plateau for both resonators.

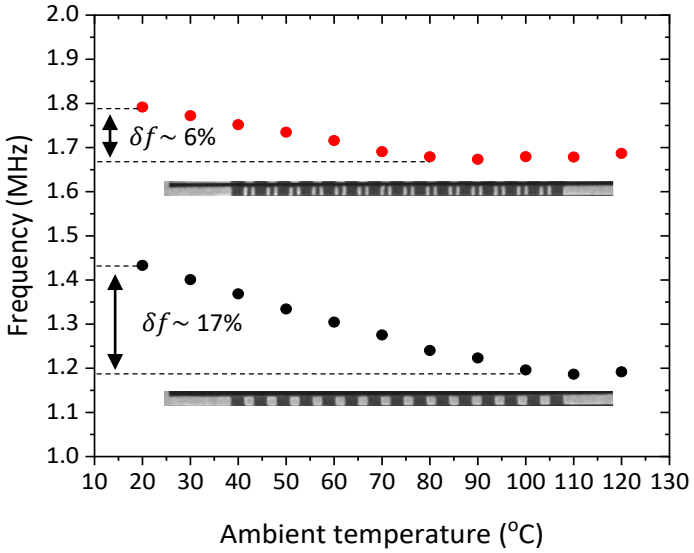

Figure 4.7 Ambient temperature control of mechanical resonances. Resonance frequencies of the single dipole (black) and double dipole (red) beams as a function of ambient temperature.

The observed decrease of resonance frequencies with increasing ambient temperature supports the conclusion that the observed frequency shift arises from temperature variations that modify the internal stress of the beam structures. Quantitative differences should be expected for the two different heating mechanisms. Laser irradiation (Figure 4.5 (a)) causes local heating of the beams at their centre, the thermal energy being conducted through the beams to the surrounding membrane. The local temperature increase modulates the internal stress while the membrane remains largely unaffected. Ambient heating (Figure 4.7) on the other hand, heats not only the beams but the supporting membrane as well, resulting in stress variations not only of the nanostructures but of its support too. In fact, for a resonator supported at the edges and subjected to ambient heating, its internal stress will be modified according to [78]

$$\sigma = \sigma_0 - E(\alpha - a_{sup})\langle \Delta T \rangle \tag{4.12}$$

where a_{sup} is the thermal expansion coefficient of the support material. However the case presented here is more complex. Not only the surrounding membrane will expand upon heating but additionally, the silicon frame supporting the membrane will also expand introducing further complexity in the thermal response of the structures.

4.5 Optomechanical metamaterial nanobolometer

The two beam system presented here essentially functions as a nanomechanical, metamaterial based bolometer. Bolometers detect radiation by measuring temperature increases due to radiation absorption. They consist of an absorber and a temperature sensor that are thermally insulated from their surroundings. The radiation-induced temperature change is normally detected electrically as change of electrical resistance [129], through the thermoelectric Seebeck effect [130] or through the pyroelectric effect [131]. Metamaterials have attracted interest as bolometer absorbers as they allow engineering of the polarization and spectral dependence of radiation absorption [132-137]. Strong temperature-dependence of mechanical resonances of micro- and nanostructures provides another readout opportunity for microbolometers, which has led to recent demonstrations of electromechanical [113-115] and optical [112] readout of nanomechanical microbolometers. The structure presented here can detect incident infrared radiation based on mechanical frequency shifts and is read optically. Moreover, it can provide radiation detection with spectral and polarization selectivity, see Figure 4.8.

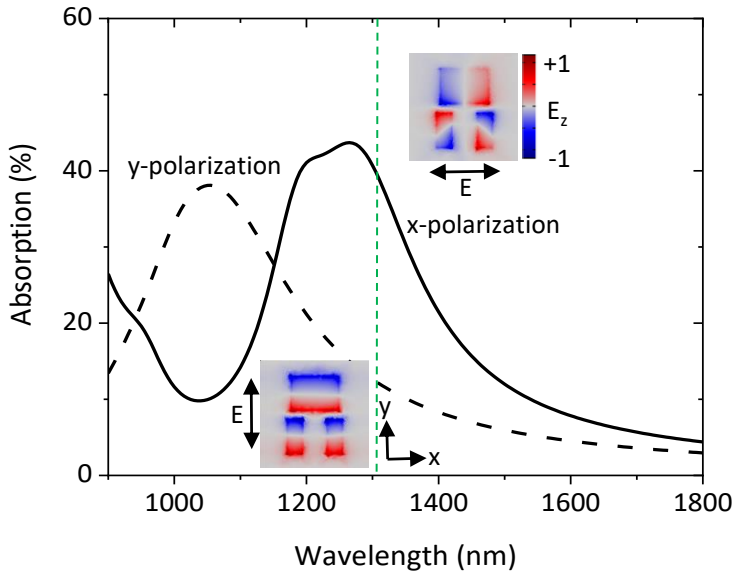

Figure 4.8 Polarization and spectral dependence of absorption of the metamaterial unit cell. Simulated absorption of the metamaterial array for normally incident light polarized parallel (x-polarized, continuous line) and orthogonal (y-polarized, dashed line) to the beams. Insets show the E_z field distribution 10 nm above the gold layer at the wavelength of 1310 nm, indicated by the green dashed line.

The main performance characteristics for a thermal detector are its responsivity, noise equivalent power (NEP) and its cooling timescale (or thermal time constant) [138]. According to the linear fits of resonance frequencies as a function of incident power per nano-beam (Figure 4.5 (a)), the resonance frequencies shift by -38 and -57 kHz/μW of laser power incident on each beam. These values correspond to the nanobolometer's responsivity. From the variation of detected resonance frequencies at fixed optical power, we determine a frequency noise of around 170 Hz/Hz$^{1/2}$, which corresponds to a noise equivalent power of 4.5 and 3 nW/Hz$^{1/2}$ respectively. The main sources of noise in the system are the instabilities of the incident laser and the thermal fluctuations of the structure. The temperature increase of the metamaterial mechanical resonators can also be described as $\Delta T = PA(\lambda)R_{\mathrm{th}}$ were P is the optical power incident on the resonator, $A(\lambda)$ is the absorption at the wavelength λ of the incident radiation and R_{th} is the structure's thermal resistance. Considering absorption of 37%, at 1310 nm and for x polarized light, the thermal resistance of the single and double dipole beams is $R_{\mathrm{th}} = 2.9$ and 4.0 $\mathrm{K/\mu W}$, respectively. With heat capacities of about 0.7 pJ/K, this implies cooling timescales on the order of 2-3 μs, corresponding to a few cycles of mechanical oscillation. While the cooling time of the nanomechanical system is only a few microseconds, in practice, the time required for nanobolometer readout will be determined by the measurement of the resonance frequency of a beam. Considering the Fourier transform of a time-domain signal, the measurement time required for achieving a frequency resolution that matches the resonance width Δf is $1/\Delta f$, which ranges from 190 to 750 μs in our nanobolometer. However, both higher accuracy and shorter measurement times may be achieved using frequency interpolation techniques.

In comparison to nanoelectromechanical [114, 139], metamaterial [135-137] and conventional [140, 141] microbolometer arrays, our optically-read nanobolometer structures offer smaller sensing elements (4 μm^2) with more than an order of magnitude higher spatial resolution (400 nm) and two orders of magnitude shorter thermal time constant. In contrast, single-pixel microbolometers [113, 115, 132, 133, 138], as well as nanobolometers fed by microscale or larger antennas [142, 143], do not offer nanoscale resolution.

It is interesting to consider how the nanobolometer device might be scaled to other wavelengths. For instance, scaling the lateral dimensions of the entire geometry by a factor s and keeping the thickness constant. The mechanical resonance frequency would scale proportionally to s^{-2} according to Equation (4.2) while the effective mass would scale proportionally to s^2. Therefore, the thermal RMS displacement according to Equation (2.20) would scale with s. As the optical resonance wavelength would also scale with s, this suggests that the magnitude of the RMS optical fluctuations would not change much, indicating that the mechanical resonance should remain observable optically. The spatial resolution would scale with s and remain the same fraction of the

wavelength. The thermal resistance R_{th} should not change, while the heat capacity, and therefore the cooling timescale, would scale with s^2. The time required to measure the mechanical resonance frequency of the nanowire scales with s^2, indicating that the readout of a significantly larger bolometer would be much slower.

The above results show a proof-of-principle demonstration of the bolometer concept, however, in practical sensor implementations, it would be desirable to use a stable CW laser for the optical readout of the sensor, to measure the power of another radiation signal. A readout wavelength closer to 1120 nm (Figure 4.2 (c)) would maximize the signal of noise ratio and allow readout power levels of less than 1 µW per metamaterial beam. The minimum detectable power of the sensor could be improved by increasing its thermal resistivity and reducing its heat capacity, which could be achieved by removing gold from the ends of the metamaterial beams [120]. The spectral and polarization sensitivity, as well as the transduction of thermal vibrations to modulation of light at the readout wavelength, can be engineered by the metamaterial design, and detailed mechanical characterization of such structures can be performed by hyperspectral motion visualization scanning electron microscopy (SEM) [144].

4.6 Frequency tuning in a metamaterial array

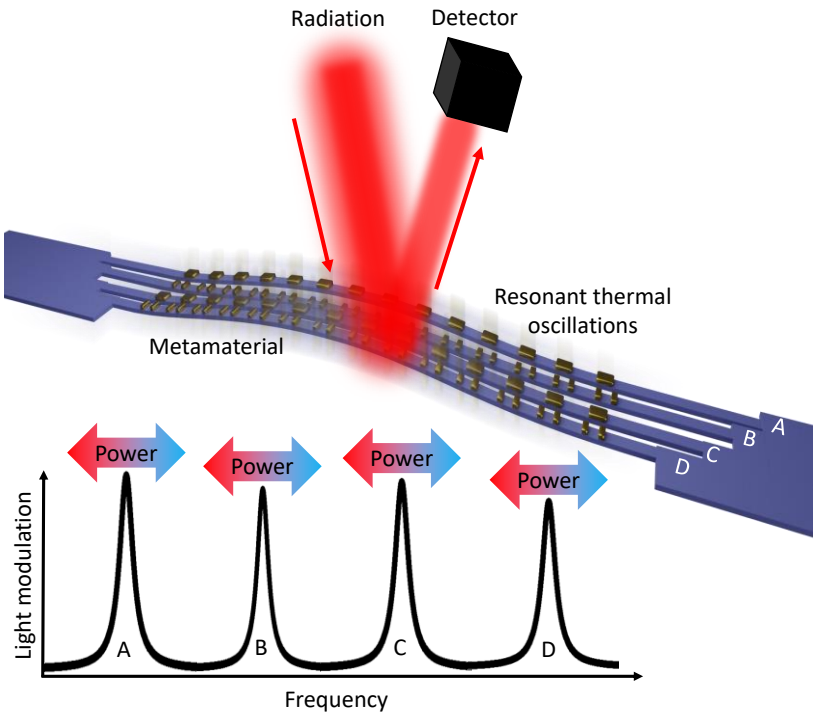

Figure 4.9 Concept of frequency tuning and bolometry in a metamaterial array. Optical heating causes frequency shifts of distinct mechanical resonances A-D of different metamaterial beams. For bolometry, they can be read individually based on the light modulation caused by their thermal motion. For actuation, they may be driven by light modulated at their individual resonance frequencies. Different metamaterial designs on different beams could be exploited for detection of (or control of different beams with) different polarizations and wavelengths.

A nanomechanical metamaterial consists of an array of metamaterial beams, where each beam can act as a nanobolometer. If these beams have sufficiently different mechanical resonance frequencies, due to different beam lengths or initial stress, then they can be read independently [70], providing a nanobolometer array with sub-micron spatial resolution, see Figure 4.9. This allows for optical sensing with sub-wavelength spatial resolution, or – in principle – polarimetry and spectroscopy based on parallel detection with beams supporting optical resonators that absorb different polarization and/or spectral components.

To demonstrate this concept an array of metamaterial beams was fabricated. Figure 4.10 (a) shows an SEM image of the fabricated plasmonic metamaterial where the length of the silicon nitride strings in the array was varied from 14 μm to 17 μm in steps of 1 μm. In total, the structure consists of 32 nanomechanical resonators and has an absorption peak close to the measurement wavelength of 1310 nm for x-polarized light (Figure 4.10 (b)), as expected from simulations (see Figure 4.8). Considering the 800 nm size of the unit cell that contains two beams segments, the structure can provide bolometry with a spatial resolution of about 400 nm, i.e. 0.3 λ. Thermomechanical measurements were taken at four different positions on the sample, each time focusing on beams of a different length. Figure 4.10 (c) shows the dependence of a resonance of each beam group on the illumination power. The natural frequency of a beam is inversely proportional to its length and therefore shorter metamaterial beams oscillate at higher frequencies. Taking into account that about 10% of the total incident power illuminates a typical metamaterial beam, we observe a responsivity of 1-2%/μW resonance frequency shift per power incident on a beam in the metamaterial. This is slightly lower than for the two beam nanobolometer, which may be due to higher initial stress in the metamaterial sample. Slightly larger responsivity for longer metamaterial beams can be attributed to an increased thermal resistance of the longer beams, causing optical heating to slightly higher temperatures.

The dependence of mechanical resonances of nanomechanical metamaterials on optical power also provides an opportunity for tuning of a number of optical effects such as electro-optic [43] and magneto-optic [45] phenomena. At natural resonances, mechanical oscillations of such nanostructures can be driven to big amplitudes, resulting in large modulation of their optical properties around the optical resonances of the metamaterial. Optical control of mechanical resonances therefore provides dynamic control over the natural frequencies at which efficient light modulation can be achieved.

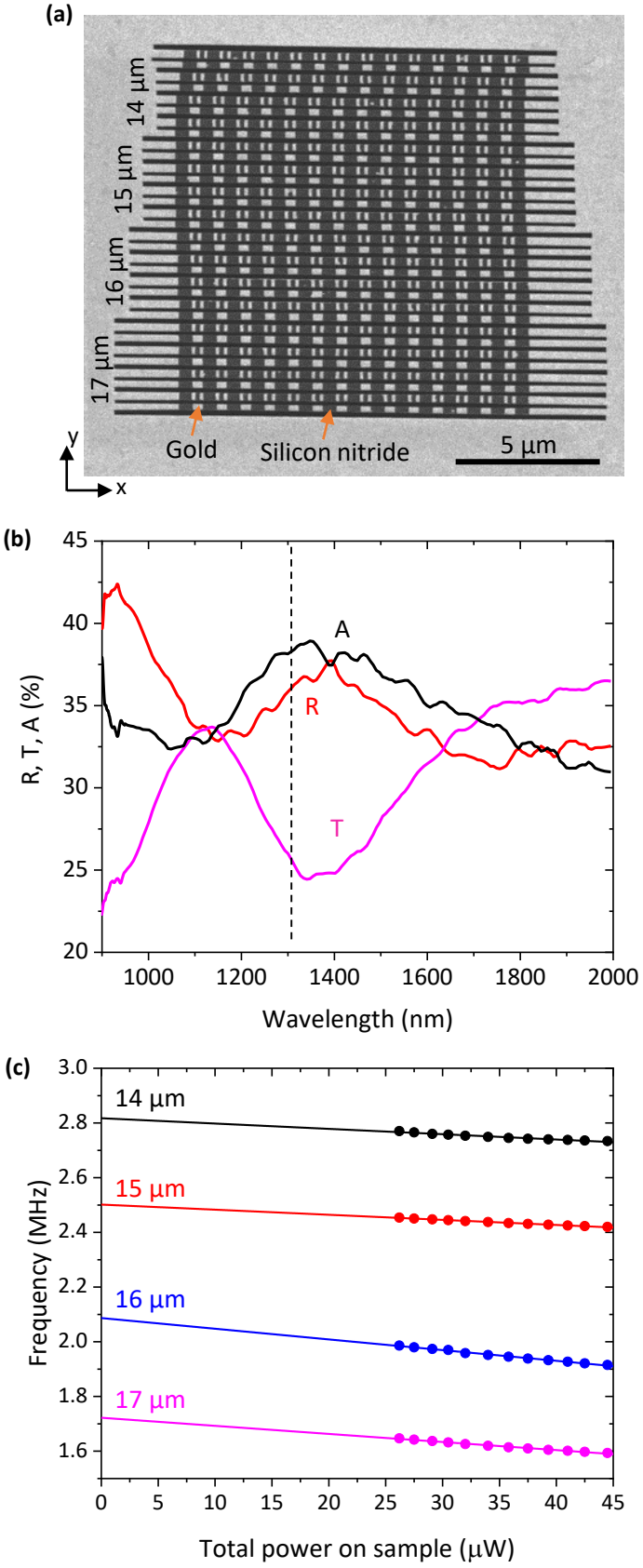

Figure 4.10 Nanomechanical metamaterial bolometer array.(a) SEM image of the metamaterial. (b) Measured transmission (T), reflection (R) and absorption (A) spectra of the metamaterial for x-polarized illumination. (c) Resonance frequencies, as a function of the total incident optical power, extracted from PSD spectra taken at different positions on the metamaterial sample, with linear fits.

4.7 Conclusions

In this chapter I studied the dependence of mechanical resonances of metamaterial beams on illumination by light. The ability to control mechanical resonances with light can be exploited for tuning of metamaterial functionalities, as well as detection of light.

It is shown that frequencies and quality factors of natural mechanical resonances of nanomechanical metamaterials can be continuously tuned by light induced heating affecting mechanical tension in the nanostructure. We observe frequency shifts of up to 20% and Q-factor changes of up to 300% at optical power levels of few microwatts per metamaterial beam. Such tuning may also be applied to nanomechanical metamaterials with addressable mechanical elements, for applications such as dynamic diffraction gratings [69], subwavelength spatial light modulators [70], and to the study of coupled mechanical systems [117] for light modulation, temperature sensing, spectroscopy and imaging applications.

Finally, the structure presented here can function as a nanobolometer with non-contact optical readout. The nanobolometer is based on detection of the modulation of optical properties caused by the fundamental sub-nanometre thermal oscillations of a nanomechanical metamaterial. The thermal motion of the metamaterial's mechanical oscillators modulates the relative position of the structure's coupled plasmonic resonators by 100s of picometers, causing detectable intensity modulation of light reflected by the nanostructure. Plasmonic absorption and thus heating of the structure results in internal tensile stress variations that modify the mechanical resonance frequencies of individual mechanical elements by 2-3%/μW of incident power. Such nanobolometers offer sub-micron spatial resolution, microsecond response times and nanowatt detection.

Chapter 5

Bistable nanomechanical metamaterials

Bistability manifests as two stable output states of a nonlinear system for the same input. Optical bistability is needed for memory functions in all-optical computing and routing in photonic circuits [145]. Generally, an optically bistable system consists of a nonlinear medium as well as an external [146, 147] or internal [148] feedback mechanism and exhibits hysteresis as a function of light intensity. The earliest examples of such systems consisted of a nonlinear material, such as sodium vapour [146], GaAs [147] or another semiconductor placed inside an optical cavity, where nonlinearity of the real and imaginary parts of the refractive index (Kerr effect and saturable absorption) leads to dispersive and absorptive bistability, respectively. Since then, optical bistability has been reported in systems such as photonic crystal microresonators [149-151], ring resonators [152-154] and lasers [155], where high-Q resonators enable low-power bistability at the cost of low optical bandwidth. In metamaterials, bistability has been reported only at microwave frequencies [156-159], where large nonlinearities are available. Thus, the challenge of weak optical nonlinearities has prevented practical, broadband, low-power solutions for bistability in the optical spectral range. In contrast, mechanical nonlinearities are easily accessible. In micro- and nanoelectromechanical systems (MEMS and NEMS), bistable cantilevers and beams can provide mechanical data storage and computing [50, 160-168]. For instance, two static mechanical buckling states [169] of nanostructures can serve as non-volatile mechanical memory [163, 164, 167] or quantum qubits [170] controlled by optical forces, electrostatically or using the magnetomotive technique.

Here, I propose the combination of optical metamaterials with nanomechanical elements i.e. hybrid nano-optomechanical metamaterials, to demonstrate bistable modulation of their optical properties as an alternative route to overcome material limitations. The origin of bistability is mechanical in nature however in metamaterials it translates into bistability of their optical properties. Section 5.1 introduces the fundamental description of the dynamic response of a doubly-clamped resonator driven to oscillate in the nonlinear regime while in Section 5.2 I describe the concept of a nanomechanical metamaterial exhibiting bistability due to its mechanical excitation by a piezoelectric element. Section 5.3 details the experimental procedures followed for the fabrication of the samples and their measurement. In Section 5.4 I present the experimental results for a pair of metamaterial beams that can exhibit bistable response which can be controlled either acoustically or optically. Finally, Section 5.5 deals with the mechanical excitation of a membrane-supported metamaterial array.

5.1 Bistability in MEMS/NEMS

In the fields of micro- and nanoelectromechanical systems (MEMS and NEMS), bistable behaviour of structures such as cantilevers and beams has been implemented to demonstrate functionalities such as mechanical data storage and computing [50, 160-168]. Switching between two stable mechanical states can be realized either in the static or in the dynamic operation regime.

In the static operation regime, mechanical buckling of nanostructures has been used to create non-volatile mechanical memory systems where the information is stored in one of the two static states of the structure [163, 164, 167, 171]. The switching between the two states can be achieved through optical forces, electrostatically or using the magnetomotive technique. Furthermore, such buckling systems have been proposed to implement quantum qubits [170] to realize quantum computing with electromechanical systems. Mechanical bistability of tethered membranes due to radiation pressure in optomechanical systems has also been observed recently [169].

In the dynamic operation regime, resonant structures driven at sufficiently high amplitudes will enter the nonlinear regime where they can also exhibit bistable response [172]. A well-studied example is that of a doubly clamped beam described by the nonlinear Duffing equation of motion [173]

$$m_{\text{eff}}\ddot{z} + \gamma_{\text{eff}}\dot{z} + m_{\text{eff}}\omega_0^2 z + \alpha_{\text{eff}} z^3 = F_0 cos(\omega t) \tag{5.1}$$

where $\gamma_{\text{eff}} = \frac{m_{\text{eff}}\omega_n}{Q_n}$ is the damping, k is the spring constant, α_{eff} is the coefficient of cubic nonlinearity, z is the oscillation amplitude and $F_0 cos(\omega t)$ the driving force. This nonlinearity is geometric in origin as it is dictated by increased compressive or tensile strain in the beam when driven at sufficiently high amplitudes, resulting in frequency pulling and the formation of a bistable region around the resonance frequency of the oscillator. The nonlinearity can be positive, making the resonator stiffer and increasing its resonance frequency or negative, making the resonator softer and decreasing its resonance frequency [172]. Systems operating in that regime have led to the demonstration of dynamic mechanical memories [161, 162, 165, 166] where access to each of the two stable states is dictated by excitation with increasing or decreasing frequency.

5.1.1 Bistability due to geometric nonlinearity

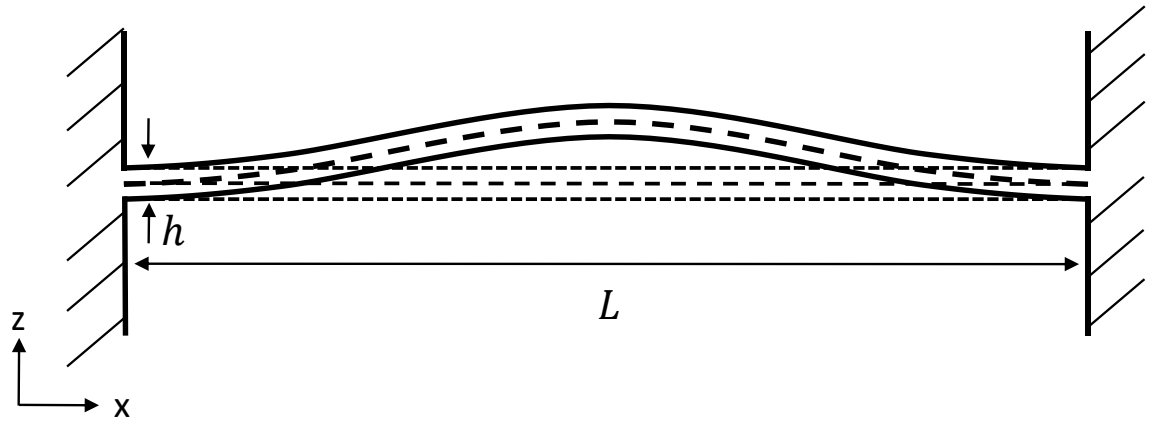

Figure 5.1 Schematic illustration of a bent, doubly-clamped beam. L: Length of the beam, h: thickness of the beam.

Nonlinearities in mechanical structures such as doubly-clamped beams can arise from geometric effects. Consider a structure such as the beam illustrated in Figure 5.1, which has clamped ends and therefore, upon bending vibrations the structure will stretch. The equation of motion, as described in Section 2.1.2, is given by

$$\rho A \frac{\partial^2 u(x,t)}{\partial t^2} + EI \frac{\partial^4 u(x,t)}{\partial x^4} - N \frac{\partial^2 u(x,t)}{\partial x^2} = 0 \tag{5.2}$$

For small amplitudes of motion (smaller than the thickness of the beam h) this stretching effect can be neglected. However, for structures of nanometer-scale thickness, amplitudes of motion larger than the structure's thickness can be easily achieved resulting in the build-up of longitudinal stress inside the beam which will result in changes of its eigenfrequency. This means that the beam is elongated by an amount ΔL and the tensile force is given by [78]

$$N = N_0 + EA\varepsilon \tag{5.3}$$

where $N_0 = \sigma A$ is the initial tensile stress, A is the beam's cross section, E is the Young's modulus and $\varepsilon = \Delta L/L$ is the longitudinal strain of the beam. The total length of the beam can be written as

$$L + \Delta L = \int_0^L dx \sqrt{1 + \left(\frac{\partial u}{\partial x}\right)^2} \cong L + \frac{1}{2}\int_0^L dx \left(\frac{\partial u}{\partial x}\right)^2 \tag{5.4}$$

and equation (5.3) becomes

$$N = N_0 + EA\varepsilon = \sigma A + EA\frac{1}{2L}\int_0^L \left(\frac{\partial u}{\partial x}\right)^2 dx \tag{5.5}$$

Inserting into Equation (5.2) together with a damping d and a driving force F results in

$$\rho A\frac{\partial^2 u(x,t)}{\partial t^2}+d\frac{\partial u(x,t)}{\partial t}+EI\frac{\partial^4 u(x,t)}{\partial x^4}-\left[\sigma A+EA\frac{1}{2L}\int_0^L\left(\frac{\partial u}{\partial x}\right)^2 dx\right]\frac{\partial^2 u(x,t)}{\partial x^2}=F(x,t) \tag{5.6}$$

From Equation (5.6) taking the intrinsic tensile stress to be zero, since the displacement of a resonator can be expressed as $u(x,t)=\sum_n z_n(t)U_n(x)$ and following the Galerkin method as can be found in [78], the lumped model equation of motion is retrieved

$$m_{\mathrm{eff},n}\ddot{z}_n(t)+\gamma_{eff,n}\dot{z}_n(t)+k_{\mathrm{eff},n}z_n(t)+a_{\mathrm{eff},n}z_n^3(t)=F(t) \tag{5.7}$$

This can be written as

$$\ddot{z}_n(t)+\frac{\omega_0}{Q_n}\dot{z}_n(t)+\omega_0^2 z_n(t)+\frac{a_{\mathrm{eff},n}}{m_{eff,n}}z_n^3(t)=\frac{F(t)}{m_{\mathrm{eff},n}} \tag{5.8}$$

where $k_{eff,n}=m_{eff,n}\omega_0^2$ and $Q_n=\frac{m_{\mathrm{eff},n}\omega_{0,n}}{\gamma_{\mathrm{eff},n}}$

This equation can be solved by assuming that the nonlinearity is a small perturbation to the linear case, detailed derivations can be found in [78, 172]. Solving for the amplitude of motion gives

$$z_0^2=\frac{\left(\frac{F}{2m_{\mathrm{eff}}\omega_0}\right)^2}{\left(\frac{\omega-\omega_0}{\omega_0}-\frac{3}{8}\frac{a_{\mathrm{eff}}}{m_{eff}\omega_0^2}z_0^2\right)^2+\left(\frac{1}{2Q_n}\right)^2} \tag{5.9}$$

This shows that for small driving amplitudes the response of the resonator follows a Lorentzian line shape. An increase of the oscillation amplitude however, will lead to asymmetric resonant curves. The frequencies for which the response will be maximum can be found by imposing $\frac{dz_0^2}{d\omega}=0$. This gives

$$\omega_{max,0}=\omega_0+\frac{3}{8}\frac{a_{eff}}{m_{\mathrm{eff}}\omega_0}(z_0^2)_{max} \tag{5.10}$$

The critical amplitude z_c, the threshold at which the resonator motion starts being nonlinear, is given by

$$z_c=\sqrt{\frac{8}{3\sqrt{3}}}\frac{1}{\sqrt{Q}}\sqrt{\frac{m_{eff}\omega_0^2}{a_{\mathrm{eff}}}} \tag{5.11}$$

and is found by imposing $\frac{d\omega}{dz_n^2}=0$ and $\frac{d^2\omega}{(dz_n^2)^2}=0$. From here it can be seen that the nonlinear regime is more easily accessible for low mass structures with high quality factor resonances.

5.2 Concept of bistable metamaterial

Optical metamaterials combined with nanomechanical elements such as beams have been shown to provide light modulation, through a variety of actuation mechanisms. Recently, such structures in combination with phase change materials have also been shown to provide memory effects in the static regime [40]. Here, we aim to demonstrate memory effects in the dynamic operation regime utilizing a plasmonic nanomechanical system similar to the one described in the previous chapters. The metamaterial design consists of silicon nitride doubly-clamped beams with resonances in the MHz range, that support plasmonic, optically resonant structures sensitive to relative beam displacement. The metamaterial sample was placed on top of a piezoelectric actuator whose displacement due to AC voltage application leads to out of plane oscillations of the metamaterial beams, see Figure 5.2 (a). Optical modulation is detected due to out-of-plane displacement of the metamaterial beams when oscillating at their mechanical resonances resulting from modulation of the electromagnetic coupling between the supported optical resonators.

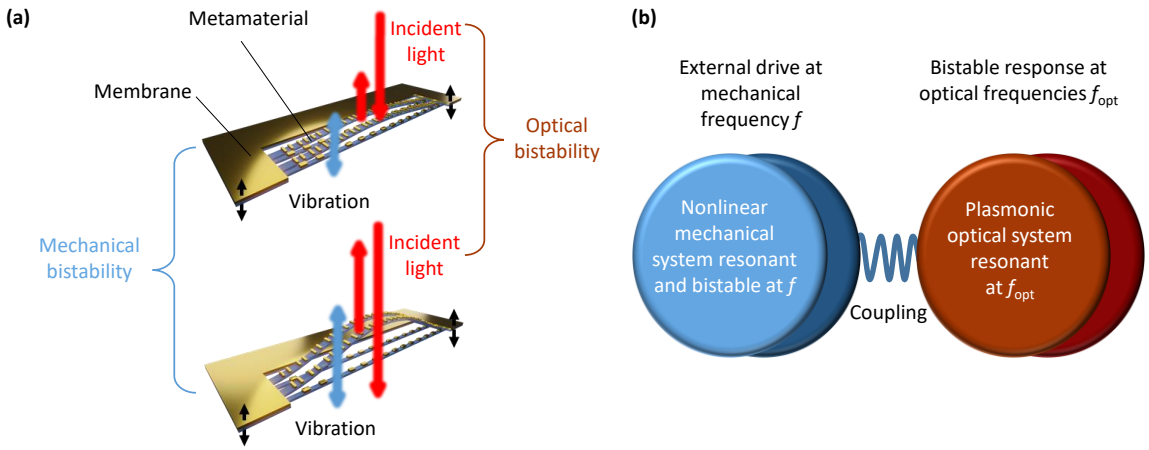

Figure 5.2 Membrane-based nanomechanical metamaterial for mechanical memory. (a) The metamaterial consists of doubly clamped beams supporting optical resonators which are forced to oscillate in the out-of-plane direction by means of a piezoelectric element. Driving the system at the resonance frequencies of the metamaterial beams results in modulation of the reflected and transmitted light. The response of the structure is detected optically and light modulation arises from modulation of electromagnetic coupling between the supported optical resonators. (b) At specific frequencies associated with the beams' mechanical resonances, the optomechanical system oscillates in the nonlinear regime resulting in two mechanical states accessed by approaching the resonance from lower or higher frequencies. Mechanically exciting the structure at such resonances results in two vibrational amplitude states for the same mechanical drive at frequency f. The vibrations modulate the coupling between the plasmonic resonators translating the mechanical bistability into bistability of the optical properties of the metamaterial at frequencies f_{opt}.

If the mechanical oscillations enter the nonlinear regime, a bistable resonant response of the structure is expected, depending on the direction of frequency excitation, which would manifest as hysteretic modulation of the structure's optical properties. This process is illustrated in Figure 5.2 (b). The mechanical system is driven in the nonlinear regime at a mechanical frequency f where it becomes bistable. The bistable states are selected by approaching the mechanical frequency f from

either lower or higher frequencies of mechanical excitation. The supported plasmonic system has an optical resonance at frequency f_{opt}=230 THz (wavelength of 1310 nm). This configuration translates the mechanical bistability of the nanomechanical metamaterial system into bistability of the metamaterial's optical properties near its resonant wavelengths.

5.3 Experimental details

5.3.1 Metamaterial excitation and experimental setup

In order to induce large amplitude oscillations of nanomechanical metamaterial beams, excitation of the structure by means of a piezoelectric element was selected. Piezoelectric actuation of nanostructures is a simple scheme commonly employed to study the mechanical response of structures such as beams [174], cantilevers [165] and membranes [175-177] due to easy integration and large excitation amplitudes that can be achieved, however, prior to this work, it had not been applied to actuation of nanomechanical metamaterials, yet. A commercially available piezoelectric chip (Thorlabs Inc., model number: PA4FEH3W) was selected for the experiments consisting of multiple Lead Zirconate Titanate (PZT) layers with a specified resonance frequency around 600 kHz. The chip measures 5x5 mm^2, with a height of 2 mm and has a 2 mm through-hole at its centre and was mounted on a brass base of one inch diameter, also with a through-hole at its centre to allow transmission measurements (Figure 5.3 (a)). As the base is much heavier than the membrane-supporting frame, it will remain stationary during vibrations, resulting in the vibrations being transferred to the membrane frame only. The silicon frames supporting the membranes were mounted centered on top of the piezoelectric chip, using double-sided tape, see for example Figure 5.3 (b), to allow out-of-plane oscillations of the metamaterial structures. The brass disk was then loaded inside a vacuum chamber equipped with electrical connections to drive the piezoelectric chip supporting the membrane/metamaterial structure.

The experimental setup used for the measurements can be seen in Figure 5.4 (a). This is identical to the one described in Section 3.1 with the difference that a transmission collection objective (N.A. 0.4) was added to the bottom part of the microscope allowing collection of the light transmitted through the metamaterial. The transmitted light was collected and directed via a fibre to a second fibre-coupled photodetector. As described in Chapter 3 and Chapter 4 , a spectrum analyser was initially used to detect the mechanical resonances of the structure by measuring the signal arising from fluctuations of its reflectivity. This is illustrated in Figure 5.4 (b). For the mechanical excitation of the structure, a frequency response analyser (Moku:Lab) was used to drive the piezoelectric with a sinusoidal signal and record the signal arising from reflected and transmitted light modulated by the vibrating metamaterial, see Figure 5.4 (c).

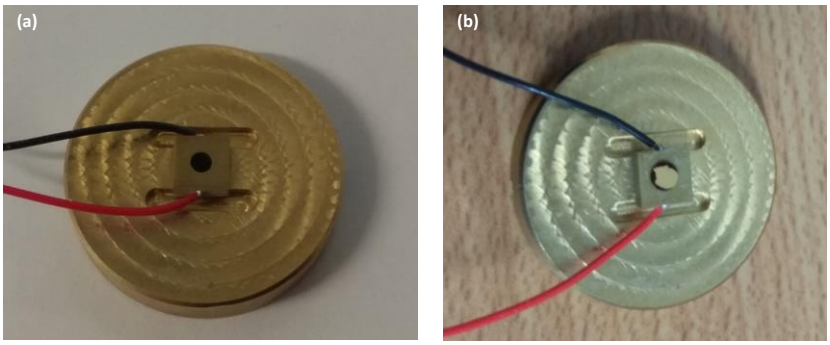

Figure 5.3 The piezoelectric chip used to drive the nanomechanical metamaterial. (a) The piezoelectric chip was mounted on a brass disk with grooves for electrical isolation and a hole for transmission illumination of membrane samples. (b) The membrane supporting frames are placed on top of the piezoelectric.

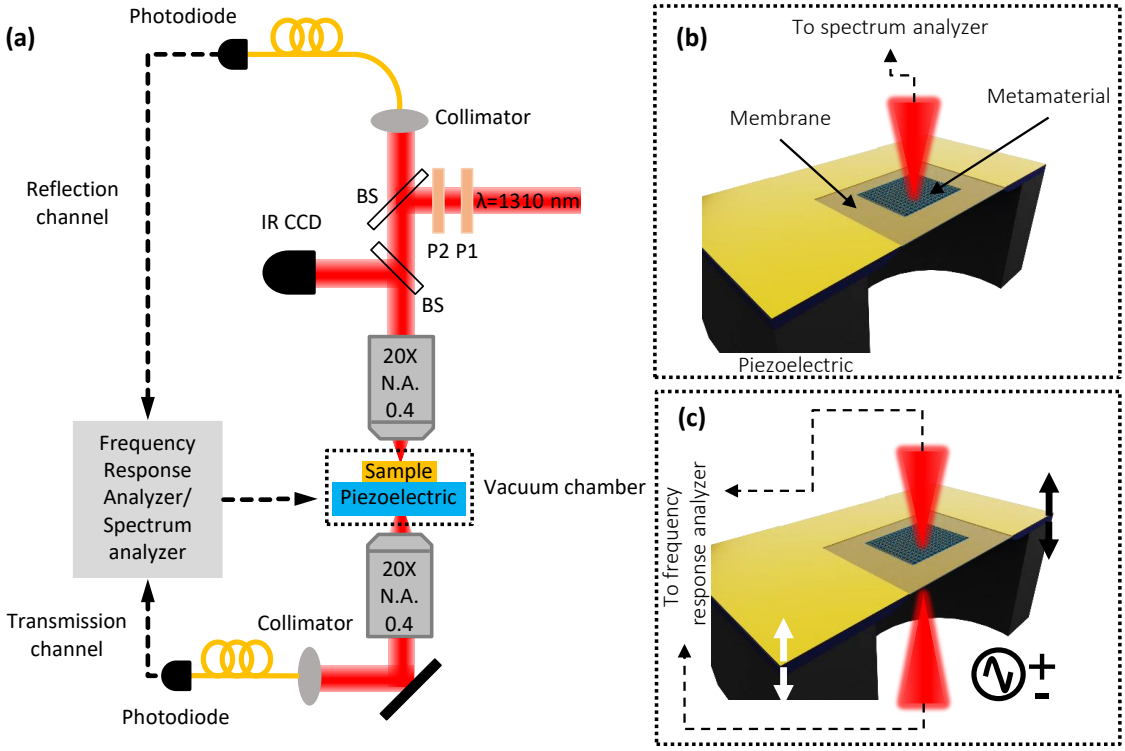

Figure 5.4 Experimental setup for bistability measurements. (a) Schematic of the setup. (b) Detection of mechanical resonances due to thermal motion. Detection of the resonances is performed by a spectrum analyser. (c) Excitation of the structure by application of an AC signal to the piezoelectric. The modulated signal is detected by a frequency response analyser.

5.3.2 Design of freestanding membranes for nonlinear metamaterials

Since the structures fabricated so far are surrounded by a much larger freestanding membrane, excitation of the whole system via the piezoelectric element will inevitably lead to oscillations of the supporting membrane, imposing challenges on the identification of the resonances arising from oscillation of the metamaterial beams. To address this challenge, new membrane windows were designed to allow clamping of the metamaterial beams on the

supporting silicon frame during FIB milling. The new, custom membrane windows were designed by me and Eric Plum and were fabricated by Norcada Inc. They consist of rectangular slits 400 microns long. Each silicon frame supports 8 slits with varying width from 75 µm to 10 µm as can be seen in Figure 5.5. The membranes consist of 50 nm thick, low stress (<250 MPa) silicon nitride. Figure 5.6 shows a photograph of one of the fabricated chips along with a microscope transmission image of one of its membrane windows.

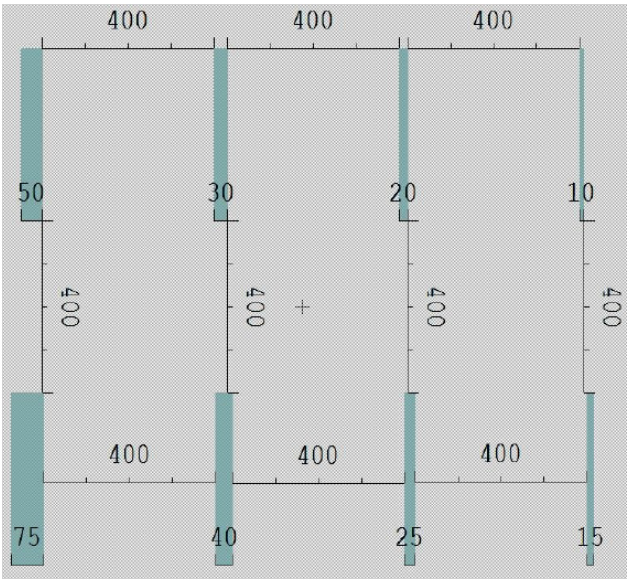

Figure 5.5 Finalized Norcada design for rectangular membrane windows. Units: µm

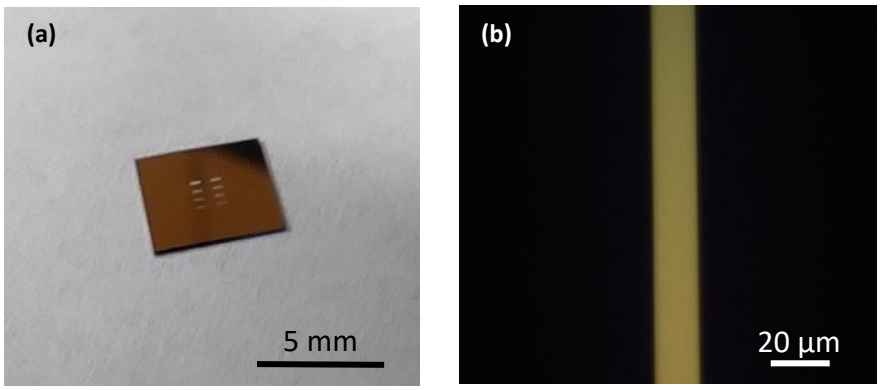

Figure 5.6 Silicon frame supporting rectangular silicon nitride membranes. (a) Photograph of an entire chip. (b) Microscope image of a fragment of an individual membrane.

The nanomechanical beams were FIB milled parallel and across the entire width of the membrane window. The goal of using membrane windows of such shape is twofold. First, to realize true fixed boundary conditions for the beams as their ends end up being supported by the membrane-supporting silicon frame. This allows the tensile stress in the beam structures to increase upon oscillation, leading to the emergence of the cubic nonlinear term in Equation (5.1). Second, it isolates the beams from the rest of the membrane ensuring that membrane resonances do not affect the beams' driven response. Figure 5.7 summarizes some of the fabrication results on

rectangular membranes of around 16 µm width. The structure presented in Figure 5.7 (b) was selected for the experiments, since having a pair of oscillating metamaterial beams allows the identification of the detected mechanical resonances as already demonstrated in Chapter 4. Attempts to mill the surrounding bilayer membrane around such structures (as seen in Figure 5.7 (c)) led to deposition of material around the sides of the beams, see Figure 5.7 (d) and such samples were thus discarded.

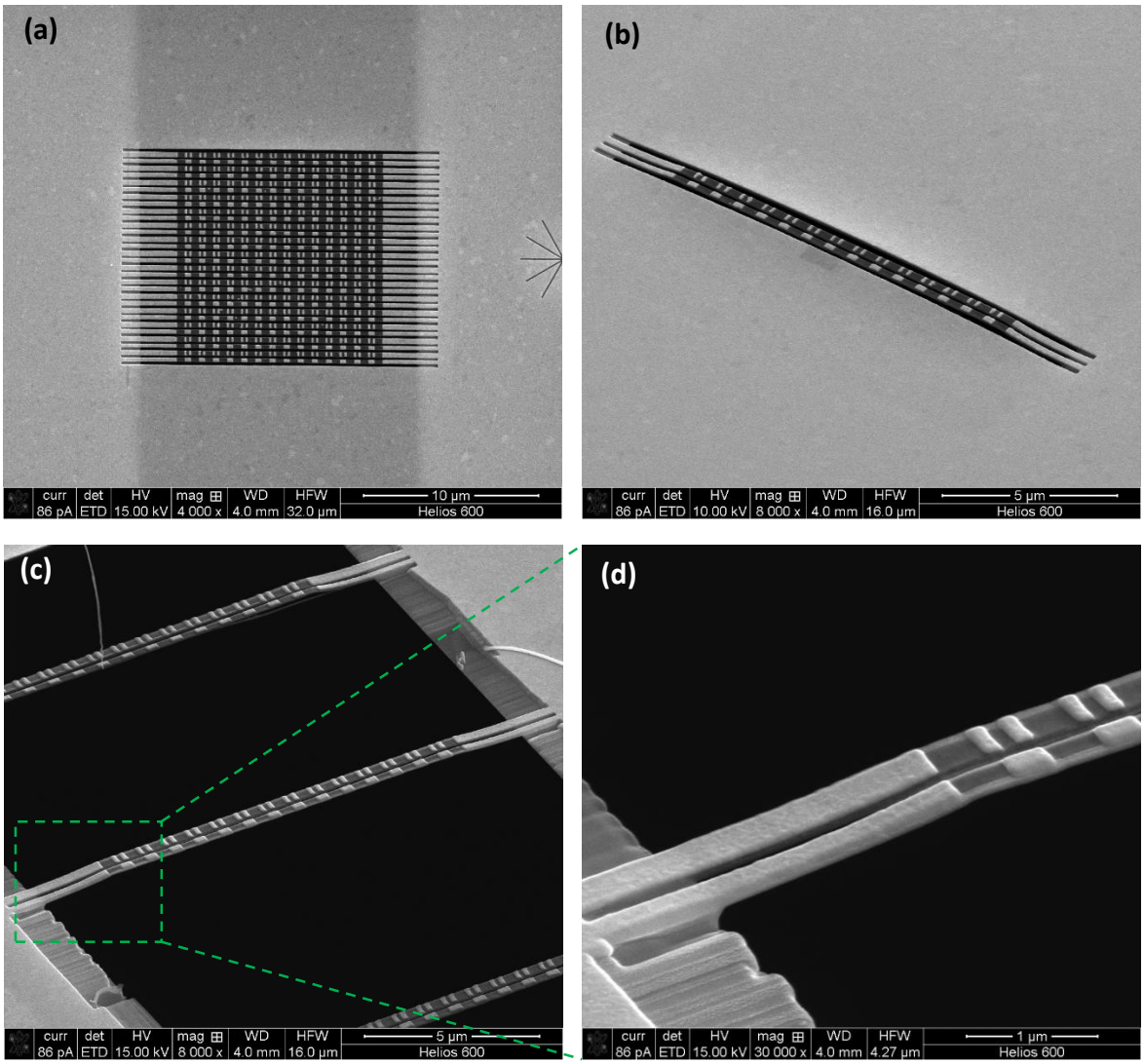

Figure 5.7 Fabrication results on rectangular membrane windows. (a) SEM image of a fabricated metamaterial array. The membrane measures around 16 µm in width. (b) Image of the metamaterial beam pair used in the experimental detection of bistability, taken at an angle of 52°. (c), (d) Images of beam pairs having the surrounding membrane removed, taken at an angle of 52°.

5.4 Bistability in nanomechanical metamaterials

Figure 5.8 (a) shows the geometric details of the unit cell of the fabricated structure consisting of a narrow beam with a width of 230 nm and a wider one that is 280 nm wide. The fabricated structure presented in Figure 5.7 (b) and Figure 5.8 (b) measures 15.8 µm in length supporting 14 plasmonic

oscillators. In order to identify the structure's mechanical resonances, the power spectral density of the back scattered light was measured using a spectrum analyser. Figure 5.8 (c) shows the spectrum obtained for 52.2 µW total incident laser power (1310 nm wavelength) focused on the centre of the two beams. Two peaks, corresponding to thermal motion of the two nanomechanical beams at their mechanical resonances, are detected. This signal originates from relative motion of the beams, which modulates the coupling between the plasmonic metamolecules resulting in modulation of the back scattered light at the structures' resonance frequencies. The mechanical resonance of the narrow beam is located around 1.56 MHz and that of the wide beam around 1.99 MHz.

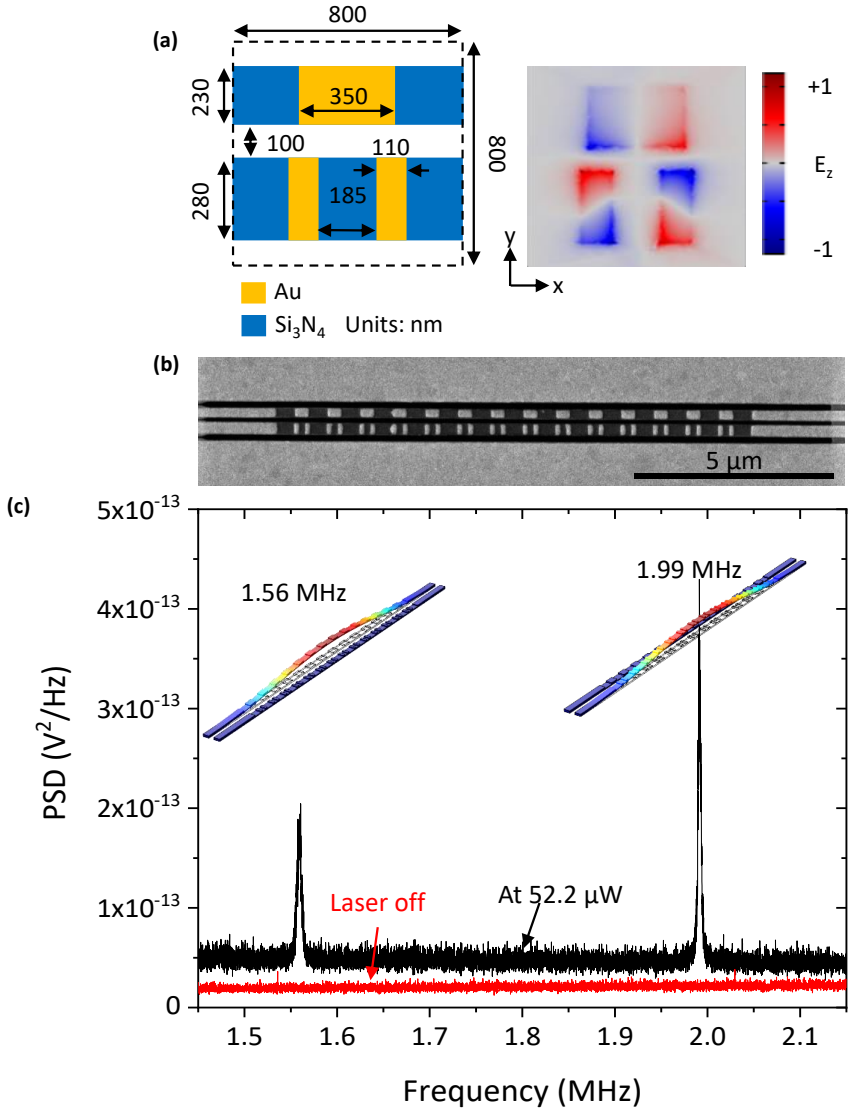

Figure 5.8 Metamaterial based nanomechanical system for detection of nonlinear and bistable response. (a) Unit cell dimensions (left) and simulated E_z field distribution 10 nm above the plasmonic structure (right) for 1310 nm normally incident radiation polarized parallel to the silicon nitride beams and periodic boundary conditions. (b) SEM image of the fabricated, two beam sample (c) The power spectral density of light back scattered by the two beam system identifies the mechanical resonances of the plasmo-mechanical structure in the MHz range. Insets show FEM simulations of the respective mechanical modes of oscillation.

5.4.1 Acoustically controlled bistability

The next step is to mechanically excite the structure by application of a sinusoidal voltage to the piezoelectric element on which the membrane frame is placed. A frequency response analyser is used to drive the piezoelectric with a sinusoidal signal and detect the signal arising from modulation of the structure's optical properties. An example of such a measurement and the calibration procedure followed are presented in Figure 5.9. Here, the sample is illuminated with a laser beam of total power of 52.2 µW. Figure 5.9 (a) shows oscilloscope traces of the photodetector voltage in response to the light back scattered by the sample. The voltage difference between illumination at 52.2 µW (-0.03423 V, black line) and zero illumination (-0.11663 V, red line) is 0.0824 V and corresponds to 100% modulation. This value is used to calibrate the recorded voltage values obtained when the sample is excited and illuminated at 52.2 µW, since mechanical oscillations of the sample would result in a sinusoidal modulation of the recorded voltage around the DC value of -0.034 V . A calibrated result can be seen in Figure 5.9 (b), where the sample is illuminated with 52.2 µW of optical power and a sinusoidal voltage of 0.1 V_{p-p} amplitude is applied to the piezoelectric. The left vertical axis shows the recorded voltage from the photodetector (in peak-to-peak values). Dividing the data by 0.0824 V yields the corresponding back scattered modulation (right y-axis). The same procedure is followed for calibration of the transmission data. In the following sections, all data are presented in terms of scattered light (back or forward) modulation in %.

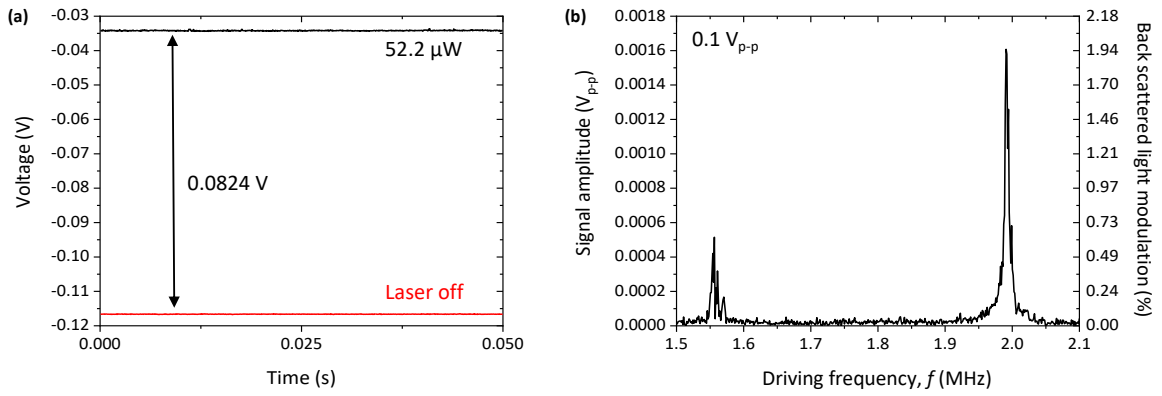

Figure 5.9 Calibration procedure for optical property modulation measurements. (a) DC voltage oscilloscope traces of the photodetector signal arising from light back scattered by the sample when illuminated by a laser beam of total optical power of 52.2 µW (black line) and when the laser is switched off (red line). (b) Modulation as a function of frequency when the piezoelectric is driven by a sinusoidal signal of 0.1 V_{p-p} amplitude.

Figure 5.10 (a) shows the back scattered light modulation depth of the two-beam structure for increasing driving amplitude from 0.05 V_{p-p} up to 0.6 V_{p-p} for total incident laser power of 52.2 µW. From the graph it is clear that above 0.3 V_{p-p} the resonant response of at least the wider beam becomes asymmetric, indicating that the structure starts oscillating in the nonlinear regime reaching a maximum modulation of around 15% for 0.6 V_{p-p} driving voltage. To demonstrate

bistable operation of the nanomechanical system we study its response by reversing the direction of frequency excitation. Figure 5.10 (b),(c) show the relative back and forward scattered light modulation for increasing (black line) and decreasing (red line) driving frequency. From these graphs it can be seen that the peak has a relatively symmetric line shape for an excitation amplitude of 0.2 V_{p-p} and is located at 1.995 MHz as indicated by the dashed blue line. However, increase of the driving amplitude leads to the peak shifting towards higher frequencies while at the same time becoming asymmetric. This can be seen in the graphs for driving amplitudes of 0.3 and 0.4 V_{p-p}. For 0.5 and 0.6 V_{p-p} a hysteresis loop appears when reversing the frequency sweep direction showing that the plasmo-mechanical system translates its mechanical bistability into bistability of its optical properties.

The resonance peak arising from oscillations of the wide beam for 0.6 V_{p-p} and increasing driving frequency is located at 2.004 MHz (15.4% back and 9% forward scattered light modulation) while for decreasing driving frequency the peak is located at 1.999 MHz (12.3% back and 7.4% forward scattered light modulation). Notably, for 0.6 V_{p-p} driving voltage and increasing driving frequency, 15.4% (9%) back (forward) scattered light modulation is detected at 2.004 MHz while only 1.5% (0.9%) modulation is observed at the same frequency when the driving frequency is decreasing corresponding to 10x optical contrast between the two states. It should be noted that although the modulation is expected to originate from differential motion of the two beams, diffraction effects arising from the gaps and membrane around the outer edges of the beams also contribute.

In this particular measurement, the response of the narrow beam does not reach the nonlinear state observed for the wider beam oscillations. This can be attributed to the excitation by the piezoelectric at these particular frequencies. In fact the response of the piezoelectric element is not flat across the frequency range of excitation. Figure 5.11 shows the measured real part of the piezoelectric's impedance for increasing and decreasing frequency excitation when excited by a sinusoidal signal of 1 V_{p-p} amplitude. No differences are observed when reversing the sweep direction, however, it can be seen that the response varies significantly in the 1.5-1.7 MHz range. Moreover, the resonance frequency of the nanomechanical beams depends on the illumination power incident on them. Therefore, variations of the optical power will lead to mechanical excitations of the structure at different frequencies which will result in varying degrees of modulation achieved for the same excitation voltage amplitude. This is illustrated in Figure 5.12. It shows that the response of the structure depends on the incident optical power as the resonances shift to higher frequencies with decreasing laser power due to internal stress variations in the beams, as discussed in Chapter 4. It is also evident that the achieved modulation amplitude differs with optical power.

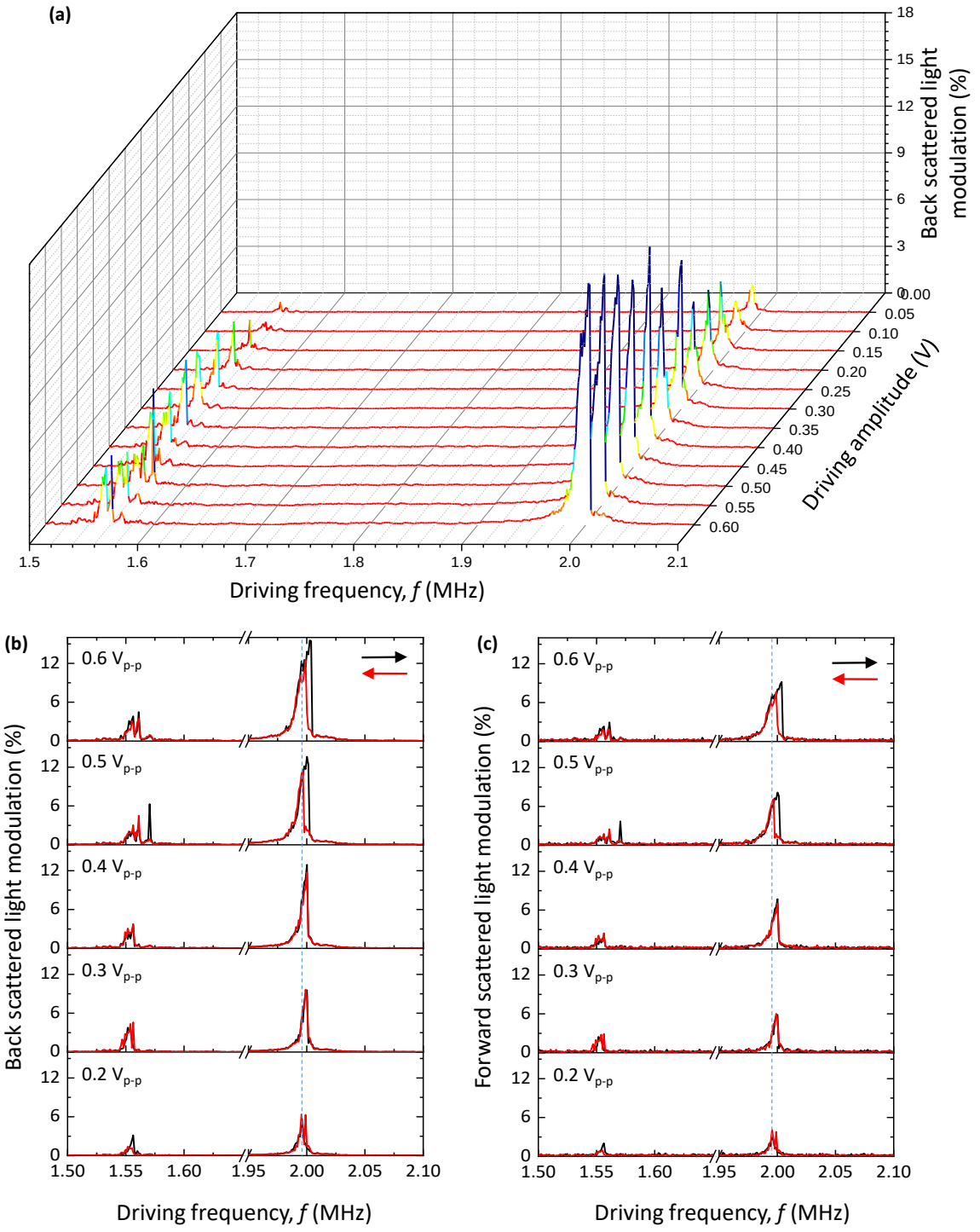

Figure 5.10 Nonlinearity and acoustically controlled bistability of light scattered by the metamaterial beams. (a) Back scattered light modulation of the two beam system measured as a function of increasing driving frequency *f* for different driving amplitudes and incident laser power of 52.2 µW. (b) Back and (c) forward scattered light modulation for increasing (black lines) and decreasing (red lines) excitation frequencies at different excitation amplitudes. Dashed light blue lines indicate the position of the peak for 0.2 V_{p-p} driving voltage at 1.995 MHz.

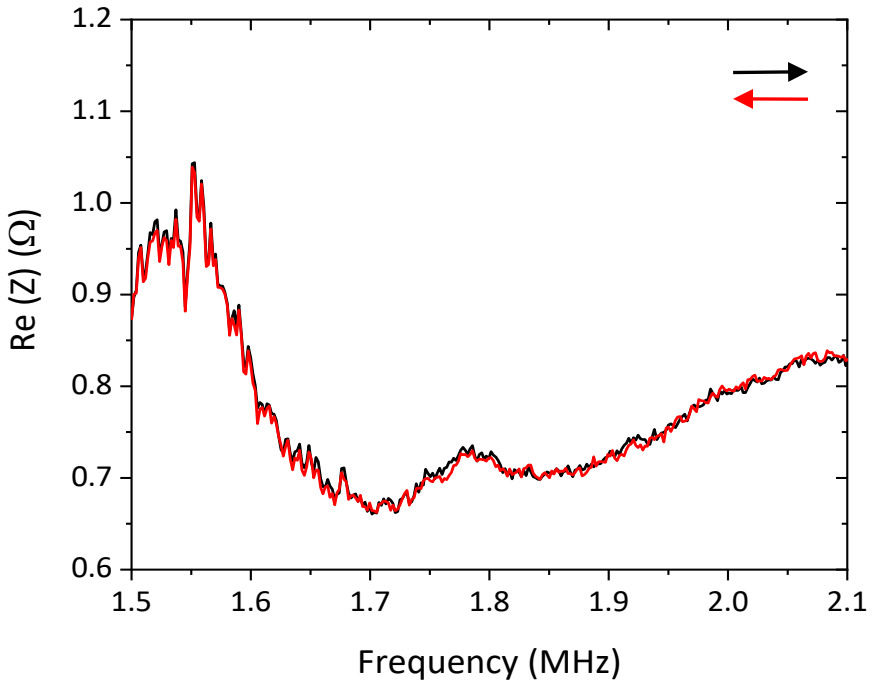

Figure 5.11 Impedance measurement of the piezoelectric element. Measurements as a function of increasing (black) and decreasing (red) frequency are in close agreement.

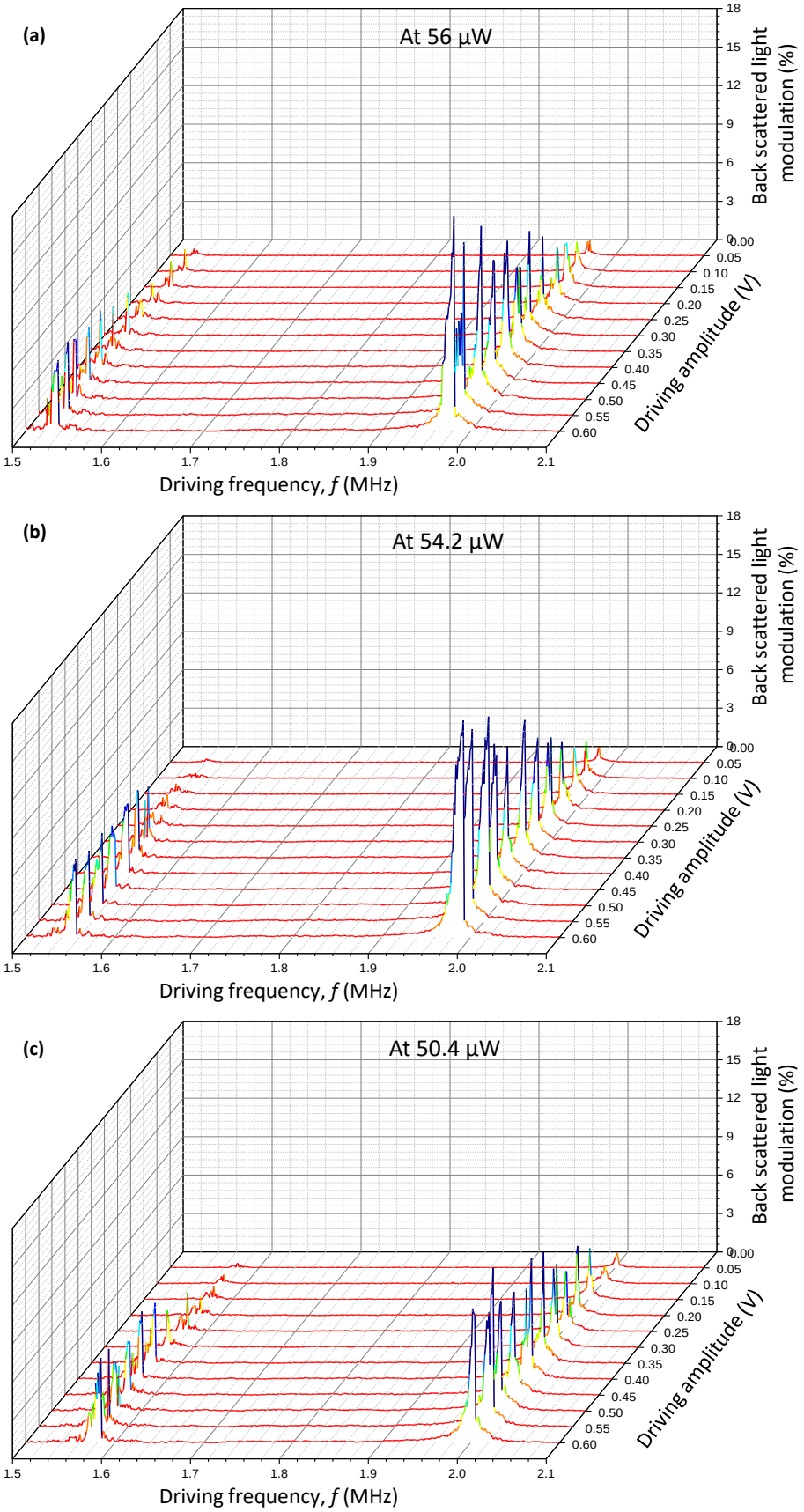

Figure 5.12 Light modulation by metamaterial beams at different illumination power levels. Back scattered light modulation with increasing driving frequency for different driving amplitudes and illumination power levels of (a) 56 µW, (b) 54.2 µW and (c) 50.4 µW.

5.4.2 Optically controlled bistability

The dependence of the resonant response of the beams on the illumination power, implies that the bistable response of the nanomechanical system can be controlled optically. This principle is detailed in Figure 5.13. As seen in Figure 5.13 (a) a hysteresis loop can be obtained when the wider nanomechanical beam oscillates in the nonlinear regime driven via the piezoelectric element by a sinusoidal signal of 0.6 V_{p-p} in amplitude. The total optical power of the incident laser beam was 56 μW. To optically induce the hysteretic response, the driving signal was fixed at a mechanical frequency of 2 MHz (Figure 5.13 (b)) and the optical power was triangularly modulated from 0 μW up to 60 μW with a frequency of 1 Hz, see Figure 5.13 (c), (d). This results in the mechanical resonance being swept across the frequency space (due to internal stress modulation), moving towards lower (higher) frequencies for increasing (decreasing) optical power, while the structure undergoes forced oscillations at the fixed driving frequency. Therefore, by increasing the optical power the modulation follows the upper branch of the hysteresis loop (black line in Figure 5.13 (a)) while by decreasing the optical power it follows the lower branch (red line in Figure 5.13 (a)).

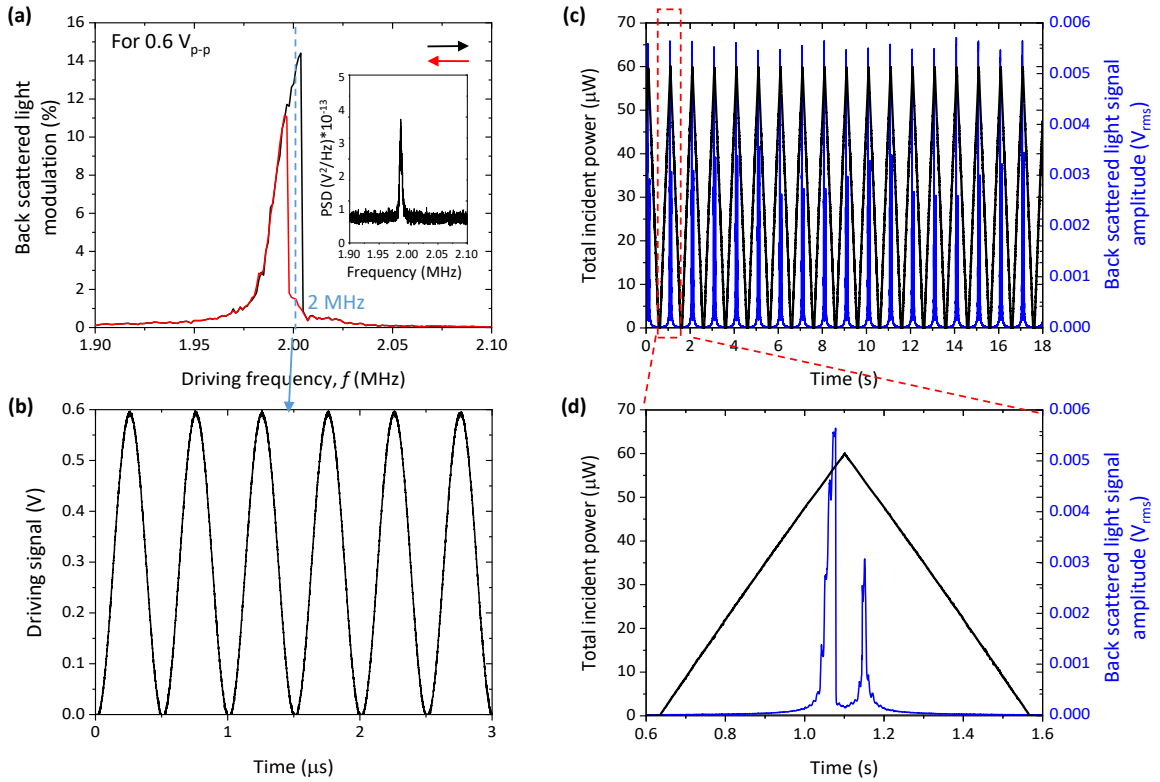

Figure 5.13 Optical control of the hysteresis cycle. (a) Hysteresis loop of the resonance corresponding to the wider nanomechanical beam for forward and reverse frequency sweep excitation by a sinusoidal signal with an amplitude of 0.6 V_{p-p} and 56 μW of incident optical power. The dashed blue line indicates the frequency of 2 MHz. Inset shows the recorded PSD spectrum of light backscattered by the beam when no voltage is applied to the piezoelectric. (b) Driving sinusoidal signal of 0.6 V_{p-p} amplitude with a frequency of 2 MHz. (c) Triangular modulation of the total optical power of the incident laser beam with a frequency of 1 Hz plotted by the black line. The blue line shows the recorded signal arising from modulation of the structure's back scattering. (d) Same as (c) for a period of one second.

The resulting back scattered light signal amplitude over one cycle of laser power modulation is shown clearly by the blue line in Figure 5.13 (d). Two maxima are recorded as the optical power

is modulated, corresponding to the two mechanical states seen in Figure 5.13 (a) for increasing and decreasing mechanical frequency excitation.

Figure 5.14 (a) shows the frequency of the mechanical resonance of the wider nanomechanical beam as a function of the total optical power incident on the sample, where the frequencies were extracted from PSD curves. As already demonstrated in Chapter 4 the peak position shows a linear dependence on optical power due to the temperature-dependent internal tensile stress of the nanomechanical beam. The stress variation with incident total optical power can be seen in Figure 5.14 (b). Figure 5.14 (c) and (d) show the optically induced hysteresis loops of the back and forward scattered light modulation signal respectively. The data plotted here come from modulation results obtained from the 18 cycles of laser modulation shown in Figure 5.13 (c). A close up view of the optically induced hysteresis curves, where the recorded signal is converted to modulation depth, can be seen in Figure 5.15, with arrows indicating the increase and decrease of the laser beam's optical power.

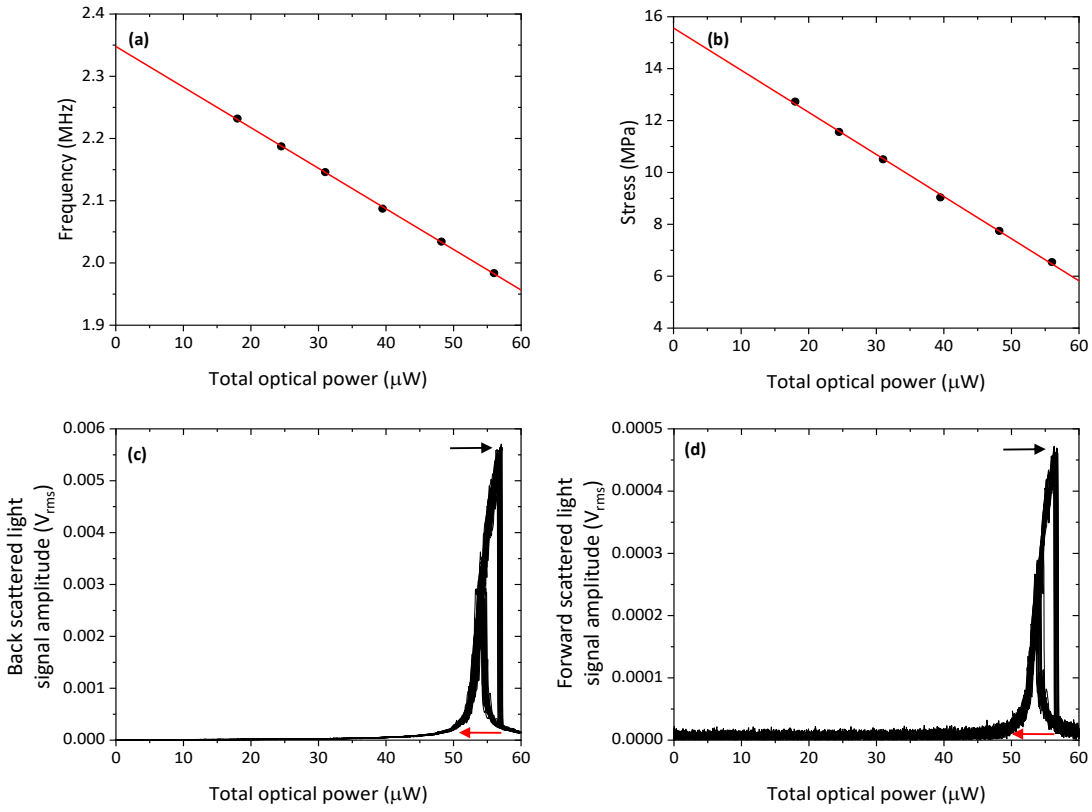

Figure 5.14 Optically induced nanomechanical bistability. (a) Dependence of the mechanical resonance frequency on the optical power of the incident laser beams. The frequencies were extracted from PSD curves. According to a linear fit (line), the mechanical eigenfrequency without laser illumination is $f_0(\sigma_0)$ = 2.348 MHz. (b) Calculated stress of the nanomechanical beam as a function of the total optical power incident on the sample. The linear fit (line) indicates the initial stress of σ_0= 15.6 MPa. (c) Back and (d) forward scattered light hysteresis curves obtained from 18 cycles of laser power modulation. The wavelength of the incident light is 1310 nm and the sample is driven by a piezoelectric element with 0.6 $V_{p\text{-}p}$ amplitude at 2 MHz.

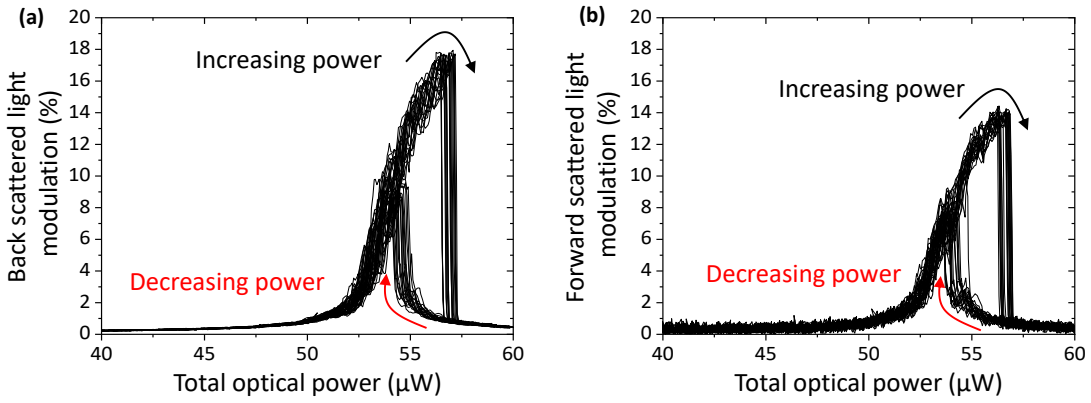

Figure 5.15 Back and forward scattered light hysteresis curves. Dependence of the modulation depth of (a) back and (b) forward scattered light on the total optical power incident on the sample under the same experimental conditions as Figure 5.14.

At $f = 2\ \mathrm{MHz}$ and $0.6\ \mathrm{V_{p-p}}$, the electrical power dissipated by the piezoelectric element is 42 mW based on an impedance of $Z = (0.79 + i1.39)\Omega$, however, only a tiny fraction of this power is transferred to a nano-beam, which is more than 11 orders of magnitude lighter than the piezoelectric element and the beam-supporting silicon frame. Using the PSD signal arising from back scattered light fluctuations a calibration of the displacement amplitude of the nanomechanical resonator upon piezo excitation can be performed. From the PSD curve shown in the inset of Figure 5.13, an RMS displacement amplitude of 198 pm is calculated which corresponds to 0.05% RMS modulation of the collected back scattered radiation. Upon excitation with a 0.6 $V_{p\text{-}p}$ amplitude signal and increasing driving frequency the beam reaches a maximum peak-to-peak displacement of around $z_0 = 57\ nm$ (corresponding to 14.4% back scattered light modulation). Considering a spring constant of $k = m_{\mathrm{eff}}\omega_0^2 = 0.10\ \mathrm{N\ m^{-1}}$ based on the beam effective mass of $m_{\mathrm{eff}} = 0.65\ \mathrm{pg}$ and the observed resonance frequency, this displacement corresponds to an energy of $E = \frac{1}{2}k\left(\frac{z_0}{2}\right)^2 = 42\ \mathrm{aJ}$, and mechanical power dissipation of $\frac{\omega_0 E}{Q} = 0.8\ \mathrm{pW}$ based on a quality factor of 620.

Such displacement amplitudes are expected to force the beam to oscillate in the nonlinear regime since the critical amplitude where nonlinearity comes into play, for a doubly-clamped beam, is directly proportional to the beam's thickness and given by $z_c \approx 1.46\, h/\sqrt{Q}$ [78, 172, 174]. For the nanomechanical beam measured here, assuming 100 nm thickness, this translates to roughly 12 nm peak-to-peak displacement.

Considering that the nanomechanical beam pair under illumination has a unit cell width of 800 nm, the widths of the nanomechanical beams (Figure 5.8 (a)) and the FWHM of the laser spot diameter of around 5 μm, the total optical power incident on the beam will be around 9.2 times lower than the total incident optical power. This means that just 6 μW of optical power on the nano-beam are enough to switch between the two mechanical states, which is orders of magnitude lower

than the power level requirements of integrated bistable systems. In such systems bistability is usually achieved by silicon micro-rings structures, taking advantage of nonlinear processes of silicon such as the thermo-optic effect [152] and carrier generation [178, 179] that usually require mW levels of input optical power, although thermal isolation of the ring structure can decrease the power required down to tens of μW [153]. Another way of introducing bistability in such integrated systems is through optically induced mechanical deformations. Optomechanical ring structures that exhibit bistability when driven by optical forces [46, 50, 51, 154, 180], usually require input power levels in the hundreds of μW range. The lowest reported power levels have been achieved by the use of high Q factor, low volume photonic crystal nanocavities [151]. Generally, such structures rely on high-Q optical resonances to achieve bistability at low power, implying that their operation is confined to a narrow wavelength range. In contrast, the bistability reported here offers large optical bandwidth. As the optical bistability arises from mechanical nonlinearity, it can be achieved with low Q factor optical resonators, which control the absorption spectrum of the structure. A direct consequence of this is that the structure can operate on a broad range of optical wavelengths around its absorption resonance

5.4.3 Dynamics of optical switching

Both the optical contrast between the bistable states and the optical power required to engage the bistability can be controlled through the acoustic driving amplitude and frequency (Figure 5.14 (a)). Figure 5.16 illustrates measurements taken at various acoustic frequencies close to 2 MHz and shows that the optical bistability occurs at lower power for higher driving frequencies. The collapse of the hysteresis response while moving away from 2 MHz is attributed at the response of the piezo chip. Alternative excitation schemes such as electrostatic actuation could be employed to prevent this.

Increasing the modulation frequency of the incident laser power indicates that the hysteresis loop can be traced at frequencies of up to about 100 Hz, see Figure 5.17. While conductive cooling estimates indicate a thermal response time of a few μs, a resonant system with quality factor Q requires Q cycles to respond to changes, with $Q \approx 620$ for the linear regime this corresponds to about 100 μs. While the system needs to respond to many changes to trace the loop, which takes milliseconds, it is expected that halving the range of power modulation allows the loop to be traced twice as fast. Indeed, it is observed that a reduced range of power modulation around the hysteresis loop at 50 μW allows the hysteresis cycle to be traced faster (Figure 5.17).

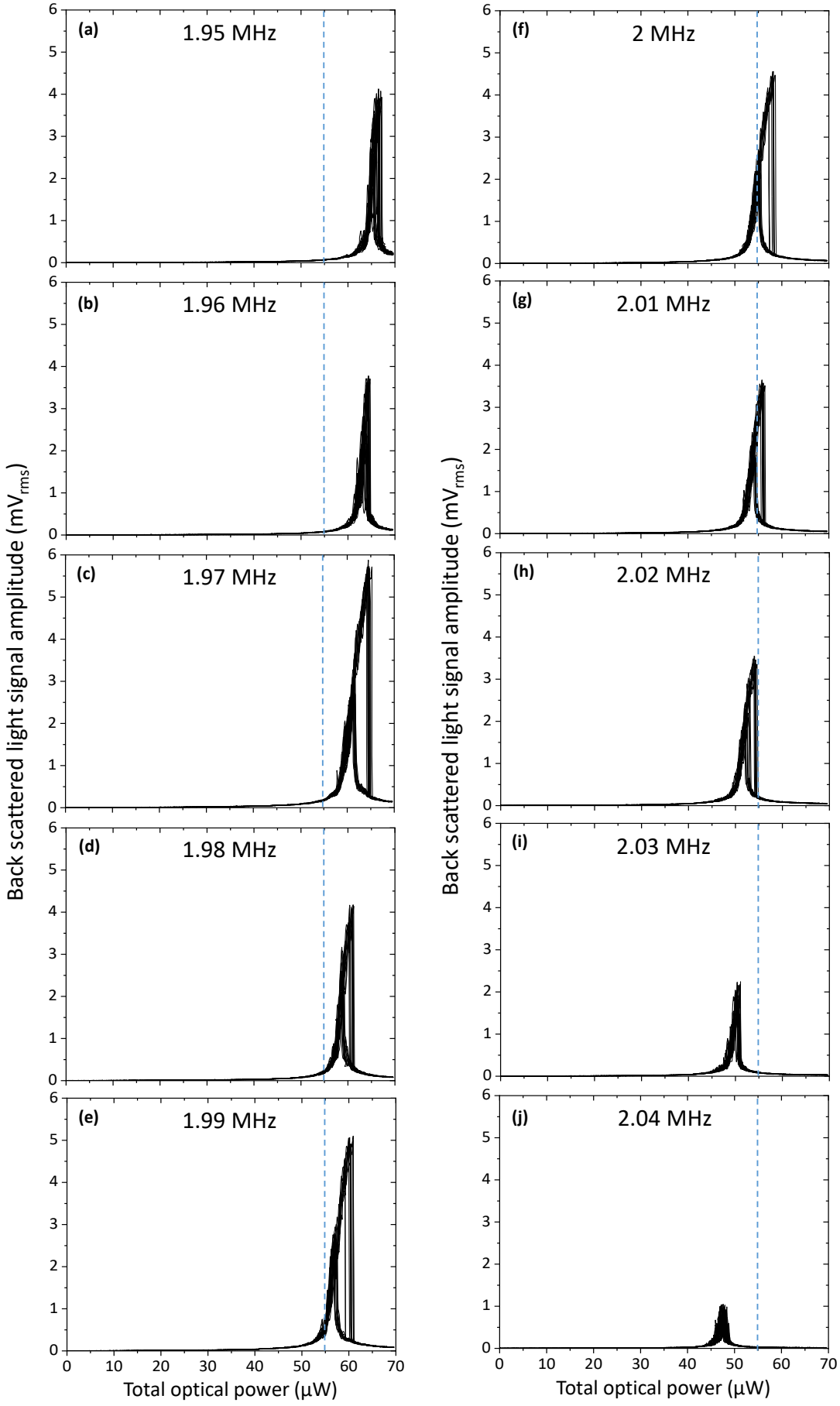

Figure 5.16 Back scattered light hysteresis cycles obtained at different fixed acoustic frequencies. Dashed blue line indicates the total optical power of 55 µW.

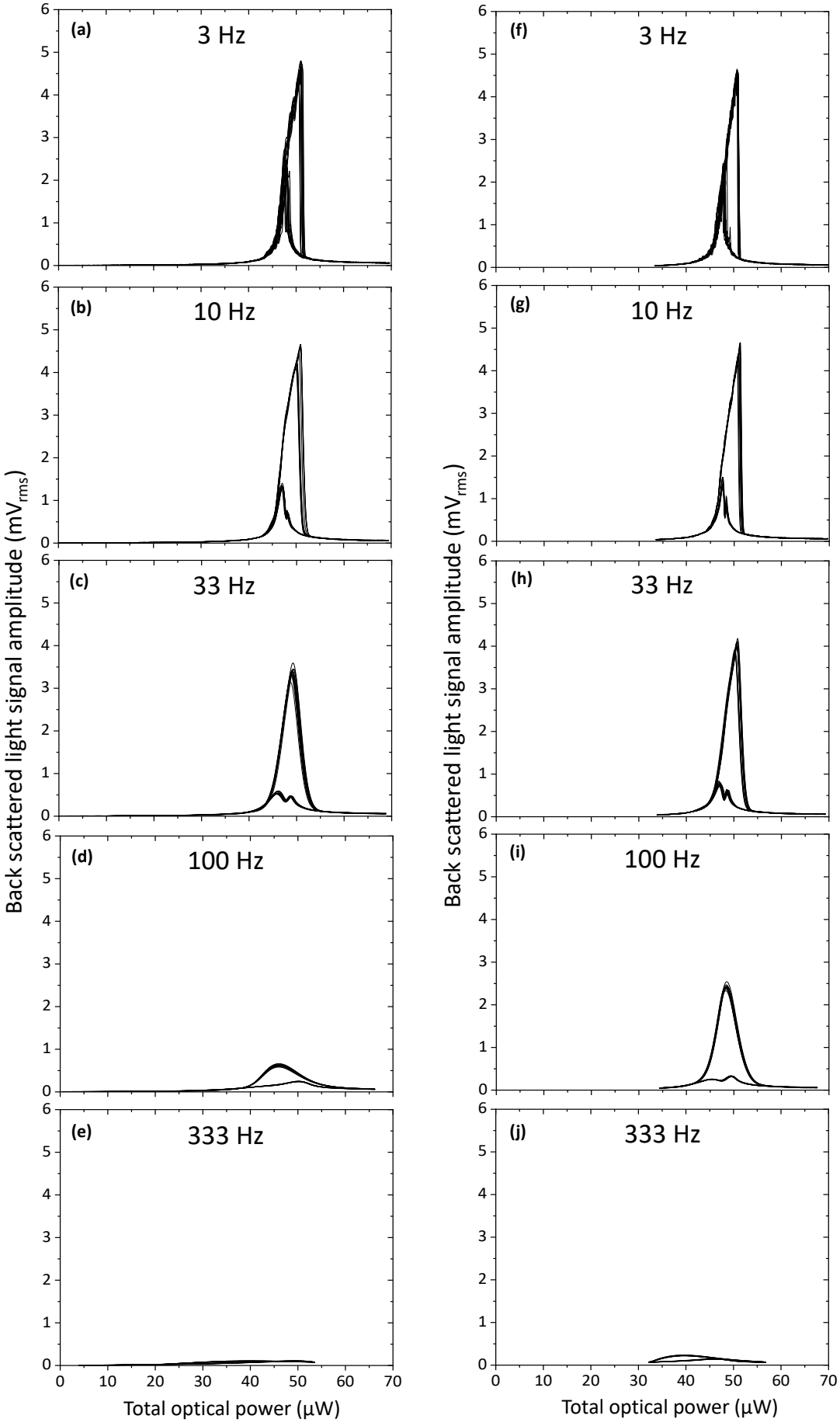

Figure 5.17 Back scattered light hysteresis cycles obtained for fixed acoustic frequency of 2 MHz and increasing laser modulation frequency. The total incident optical power is swept from (a)-(e) 0-69.5 µW and (f)-(j) 33.6-69.5 µW.

5.5 Membrane-based bistability

In the previous section, it was demonstrated that it is possible to obtain a bistable response in doubly-clamped, metamaterial beams when the structures are excited at sufficiently high amplitudes to engage the mechanical nonlinearities arising from increasing tensile stress in them. In this section I present results for mechanical excitation of a metamaterial array fabricated out of a typical 100 µm x 100 µm membrane. The nanomechanical metamaterial was milled out of a 50 nm thick, 100 µm x 100 µm gold-covered (also 50 nm thick), low stress (< 250 MPa) silicon nitride membrane. The membrane is supported by a 3 mm x 3 mm silicon frame. The frame supports 9 such membrane windows, each 100 µm x 100 µm in size. The small membrane window size here was selected in order to minimize the amplitude of membrane oscillations upon excitation of the sample. An SEM image of the fabricated metamaterial can be seen in Figure 5.18 (a). It consists of 30 silicon nitride beams, 15.8 µm long and supporting rows of 14 optical resonators, see Figure 5.18 (b). The optical properties of the fabricated structure can be seen in Figure 5.18 (c). The silicon supporting frame was placed on a different piezoelectric element with the same specifications and similarly placed in the vacuum chamber and pumped to a pressure of around 4 x 10^{-3} mbar.

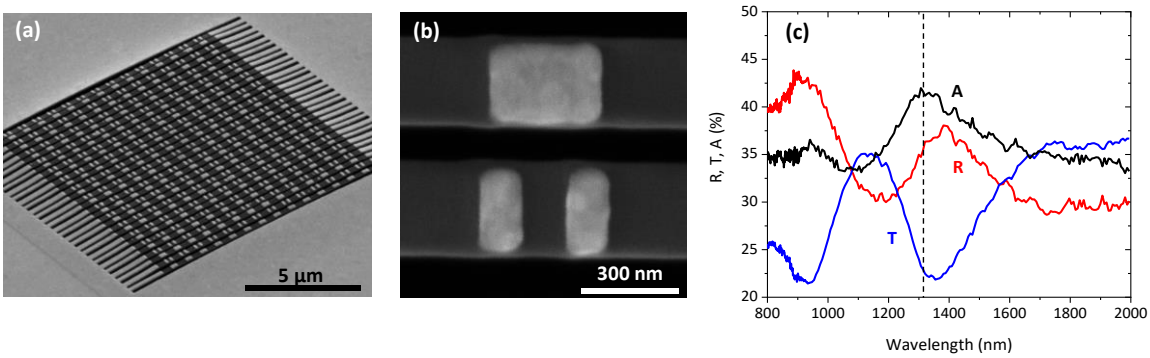

Figure 5.18 Metamaterial array for bistability experiments. (a) SEM image of the fabricated sample taken at an angle of 52°. (b) A unit cell of the structure. (c) Measured reflection (R), transmission (T) and absorption (A) spectra of the sample.

In order to locate the structure's mechanical resonances the power spectral density of the reflected light was measured using a spectrum analyser (Zurich Instruments, HF2LI). Figure 5.19 (a) shows the spectrum obtained for incident laser power of 71 µW and the laser beam focused on the centre of the metamaterial array. The result indicates the existence of mechanical resonances spread over a very wide frequency range. A group of low amplitude peaks is detected in the 1.5-2 MHz range while at the same time a much larger amplitude resonance around 2.4 MHz can be seen. Since the amplitude of the beams' thermal motion should be largest at the beams' resonance frequencies, the high amplitude peak should originate from the mechanical resonances of the metamaterial. To confirm this the incident laser power was varied and the two regions studied more closely. Figure 5.19 (b) and (c) show the evolution of the spectrum for two frequency ranges,

for varying incident laser power from 12 up to 71 μW. For the resonances in the 1.4-1.8 MHz range, no significant shift of the peaks is detected. On the contrary, the peaks detected in the 2.2-3 MHz range shift greatly with reduced incident optical power as expected for the resonances of the tensile stressed nano-beams constituting the metamaterial array. Therefore, it is possible that the resonances detected in the 1.4-1.8 MHz range originate from oscillations of the supporting membrane detected through the metamaterial structure.

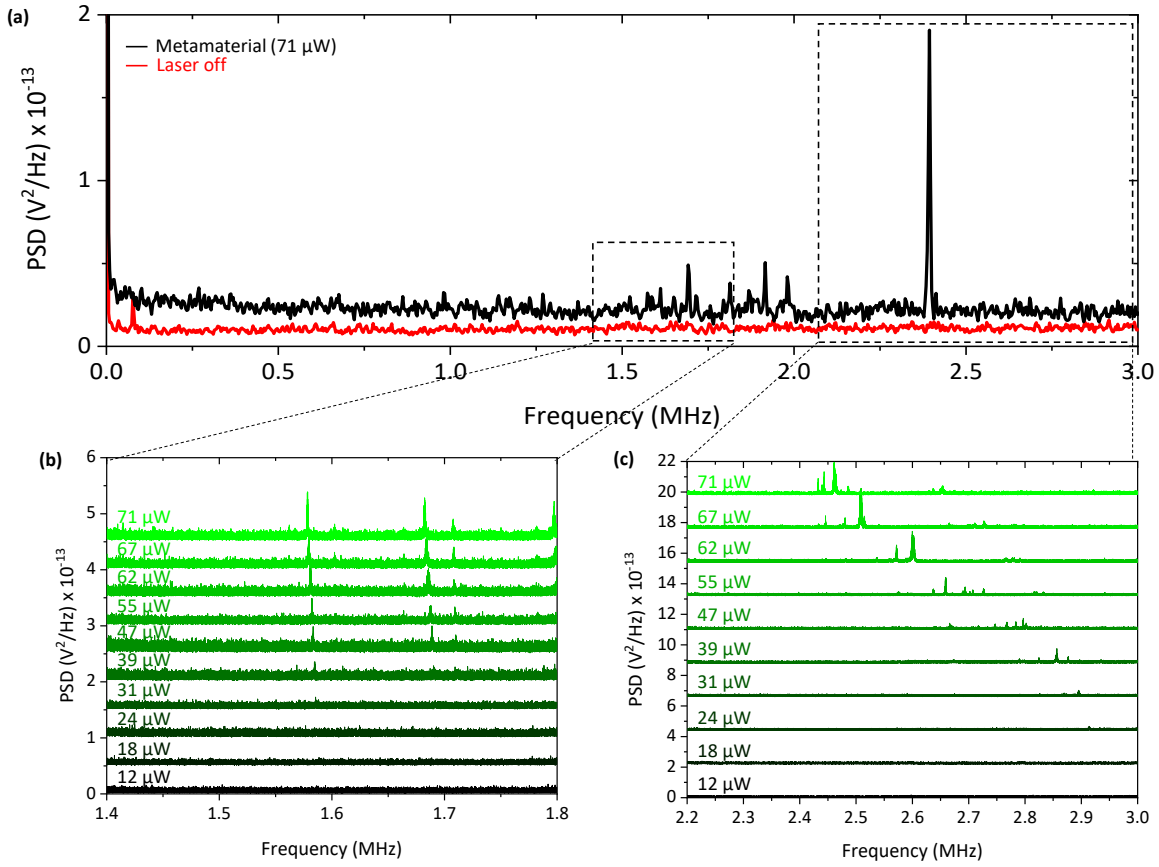

Figure 5.19 Optical detection of the metamaterial array's mechanical resonances. (a) Modulation of reflected light as a function of frequency measured at the centre of the metamaterial structure. (b) and (c) Dependence on incident laser power for selected frequency ranges.

The mechanical eigenfrequencies of a membrane structure are given by [78]

$$f_{i,j} = \sqrt{\frac{(i^2 + j^2)\sigma}{4\rho L^2}} \tag{5.11}$$

where i, j are the mode indices representing the number of anti-nodes along the two dimensions of the membrane, σ is the tensile stress, ρ is the density and L is the side length. Assuming the deposited gold layer has zero stress and taking the average stress of the bilayer to be 125 MPa and the average density of Si_3N_4 and Au to be 11200 Kg/m^3 the mechanical modes of the bilayer membrane structure can be calculated. The results for the first six vibrational modes can be seen in Table 5.1. The structure has its fundamental vibrational mode around 740 kHz and four higher

order modes in the frequency range between 1-2 MHz. Although such a rudimentary calculation does not take into account possible compressive stresses formed after the deposition of the gold layer or the fact that after milling the metamaterial structures the membrane is no longer a continuous structure, it provides an estimation of the frequency range where higher order vibrational modes of the membrane might appear. It is therefore concluded that the peaks shown in Figure 5.19 (b) are very likely to originate from thermal vibrations of the bilayer membrane supporting the metamaterial structure although it was not possible to precisely identify the membrane modes.

Table 5.1 Calculated mechanical eigenfrequencies of a 100 μm x 100 μm membrane consisting of a 50 nm-thick silicon nitride coated with 50 nm-thick gold.

Vibrational mode (i, j)	Eigenfrequency (MHz)
(1,1)	0.74
(1,2) and (2,1)	1.18
(2,2)	1.49
(1,3) and (3,1)	1.67
(2,3) and (3,2)	1.9
(1,4) and (4,1)	2.18

Next, the reflectivity and transmission modulation of the structure is measured upon driving the piezoelectric element with an AC sinusoidal signal. First, the frequency range associated with the mechanical resonances of the silicon nitride beams constituting the metamaterial is examined. Figure 5.20 (a) shows the reflectivity and transmission modulation depth when a sinusoidal signal of 0.6 $V_{p\text{-}p}$ amplitude is applied to the piezoelectric for two sweeping directions (forward and backward) of the driving frequency and for incident optical power of 71 μW. Apart from slight variations in the modulation amplitude of the resonances, no significant differences are seen for reversing the sweep direction of the driving frequency. For the forward sweeping direction a maximum reflectivity modulation of around 9.3% is recorded at 2.43 MHz accompanied by transmission modulation of 2%. In contrast, when the sample is excited at mechanical frequencies associated with the supporting membrane (Figure 5.20 (b)) for the same driving amplitude, the resulting reflectivity modulation is more than doubled with a maximum of approximately 27% around 1.58 MHz. More importantly, reversing the frequency sweep results in a significantly reduced modulation depth and a shift of the resonance peak to lower frequencies. This is particularly pronounced for the peak located at around 1.62 MHz where 21.3% reflectivity modulation is recorded in the forward sweeping direction. Reference reflectivity measurements

taken right next to the metamaterial structure on the unpatterned membrane show negligible modulation (blue line in Figure 5.20 (b))

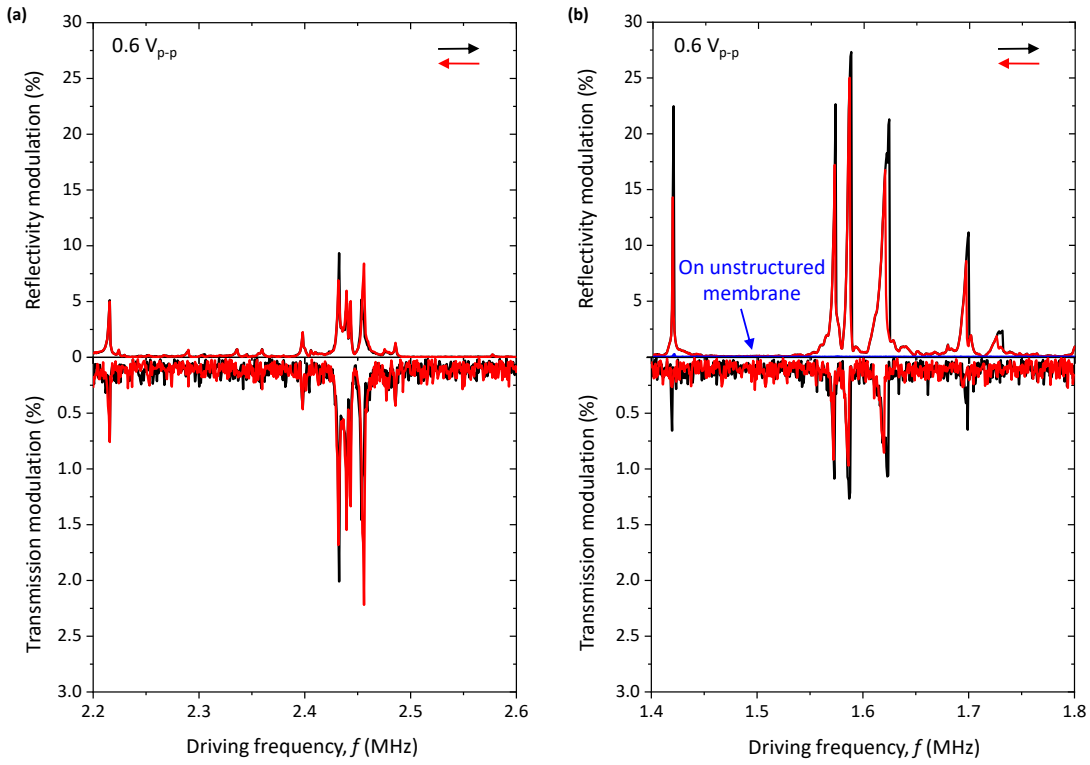

Figure 5.20 Modulation of optical properties of the membrane-metamaterial system under piezoelectric drive. Reflectivity and transmission modulation of the system when driven at the resonance frequencies of the (a) metamaterial beams and (b) membrane for increasing (black) and decreasing (red) frequency scanning directions when a 0.6 V_{p-p} sinusoidal signal drives the piezoelectric. Arrows indicate the frequency sweep direction.

To examine the response of the membrane-metamaterial system at these frequencies, the amplitude of the driving signal was varied from 0.02 V_{p-p} up to the maximum of 0.6 V_{p-p}. Figure 5.21 shows the response of the structure in the frequency range of 1.6-1.64 MHz together with the phase of the signal for various driving amplitudes. For low driving voltages of 0.02 and 0.04 V_{p-p} the response is linear and does not change when reversing the frequency sweep direction. For 0.06 V_{pp} the resonance loses its symmetric shape and starts shifting from the initial position at 1.6168 MHz towards higher frequencies as mechanical nonlinearities of the system due to stiffening come into play. At 0.08 V_{p-p}, a hysteresis loop starts forming when the direction of the driving frequency is reversed which becomes more pronounced with increasing driving voltage. The resonance peak for 0.6 V_{p-p} and increasing driving frequency is located at 1.6238 MHz (21% reflectivity modulation) while for decreasing driving frequency the peak is located at 1.6199 MHz (16.8% reflectivity modulation). Ultimately, for 0.6 V_{p-p} driving voltage and increasing driving frequency, 21.3% reflectivity modulation is detected at 1.6238 MHz while only 1.8% modulation is observed at the same frequency when the frequency scanning direction is reversed, corresponding to 12x optical contrast between the two bistable states.

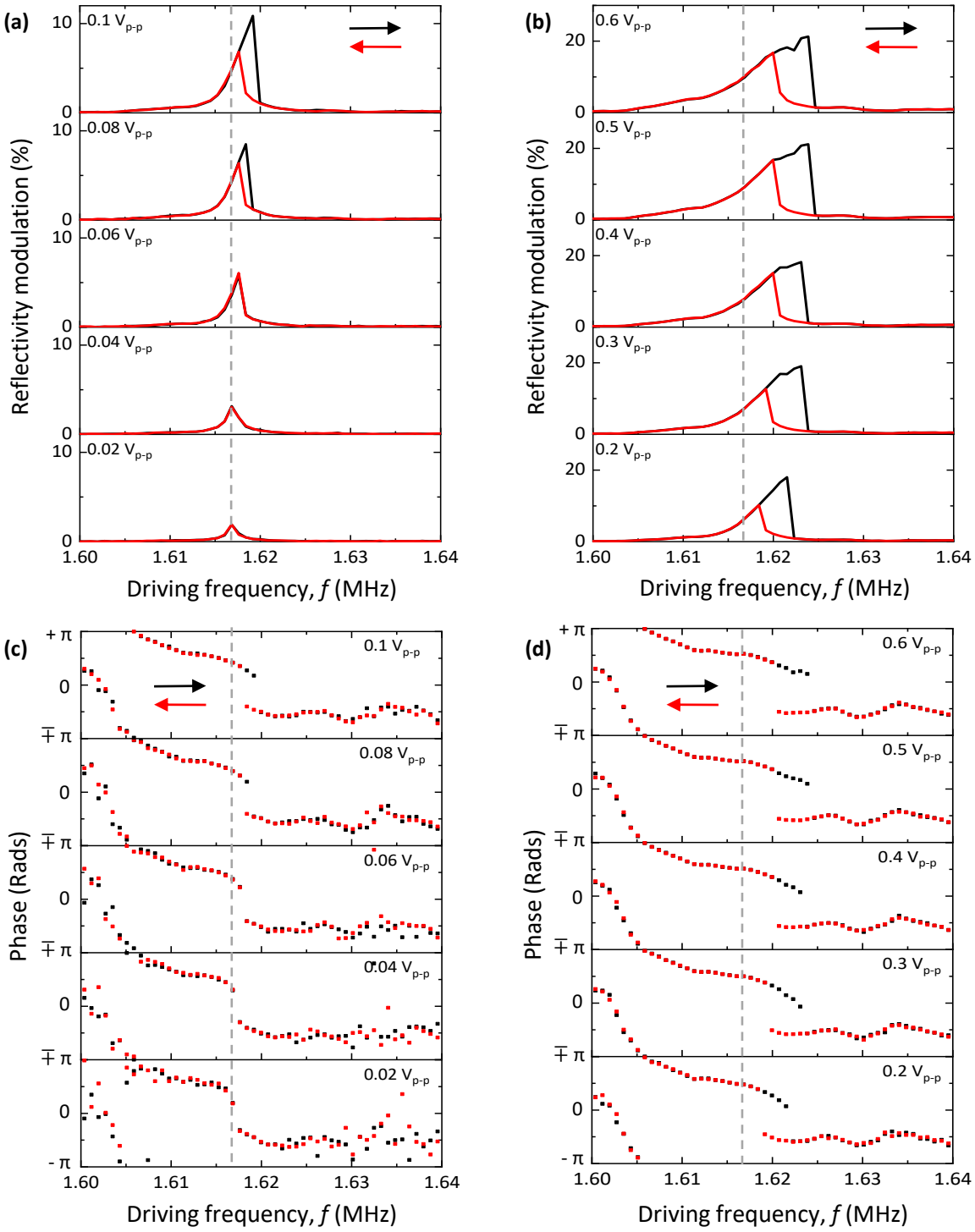

Figure 5.21 Nonlinear response and bistability of the membrane-metamaterial system. (a) Reflectivity modulation detected at a membrane resonance for different amplitudes of the sinusoidal signal driving the piezoelectric, from 0.02 $V_{p\text{-}p}$ up to 0.1 $V_{p\text{-}p}$ in steps of 0.02 $V_{p\text{-}p}$ and (b) from 0.2 $V_{p\text{-}p}$ up to 0.6 $V_{p\text{-}p}$ in steps of 0.1 $V_{p\text{-}p}$. (c) and (d) show the corresponding phase. Dashed lines indicate the frequency of the resonance for an excitation voltage of 0.02 $V_{p\text{-}p}$. Arrows indicate the frequency sweep direction.

The above results show that nonlinear oscillations and a bistable response of free-standing membranes can be detected through a supported nanomechanical metamaterial structure. Similarly to doubly-clamped beams, membranes under tensile stress are also expected to enter a nonlinear oscillation regime upon increasing vibrational amplitude [181], and this is what we observe here. However, we did not detect such behaviour for the resonances of the membrane-

supported metamaterial beams. This can be due to a number of reasons. First of all, it could be possible for the metamaterial beams to enter the nonlinear oscillation regime if higher voltage amplitudes were applied. The experiment was limited to a maximum driving voltage of 0.6 V_{p-p} in order to avoid stiction of the metamaterial beams that could occur at vibrational modes of the membrane. Second, as already demonstrated in Section 5.4, the oscillation amplitude of the structure depends on the response of the piezoelectric element. Driving of the system when illuminated at different power levels (and therefore excited at different mechanical frequencies) could result in the beams entering the nonlinear regime for voltage amplitudes of 0.6 V_{p-p} or less.

The result presented in Figure 5.20 (a) suggests that the piezoelectric actuation scheme employed here can achieve large modulation depths and has certain advantages over modulation of metamaterial optical properties by field application methods. For instance, in the case of electrostatic actuation of metamaterials exceeding a voltage threshold, causes irreversible step-like switching of the devices due to attractive electrostatic and van der Waals forces [39]. Similarly, in the case of magnetic actuation, passing a current through the wires of an array, leads to Joule heating and thermal damage of the devices above a certain threshold [45]. In the case of optical reconfiguration, thermal damage caused by the power levels of the pump beam restricts the modulation depth [56]. Here, the achieved reflectivity (transmission) modulation depth reaches around 9% (2%) at 1310 nm which is limited due to the optical response of the structure which is not optimized to provide maximum modulation at this wavelength. This could be further improved by adjusting the optical resonators to provide maximum modulation around 1310 nm.

5.6 Conclusions

In conclusion, it is demonstrated that, for sufficiently strong resonant mechanical excitation, the oscillation of metamaterial beams becomes nonlinear and bistable. In the bistable regime, the amplitude of resonant mechanical oscillation becomes dependent on both the structure's history of previous mechanical excitation and its history of previous optical illumination, and is observed as hysteretic modulation of the structure's optical properties. Thus, the mechanical bistability of metamaterial beams yields optical bistability, i.e. optically-controlled switching between states with different optical properties that are stable under identical conditions.

A structure consisting of 2 nanomechanical metamaterial beams has driven to oscillate in the nonlinear regime by a piezoelectric actuator achieving acoustically controlled hysteretic behaviour of its optical properties at pW levels of mechanical power. Optical switching between the bistable states is possible with only a few μW of optical power and the bistability is inherently optically broadband.

The results indicate that nanomechanical metamaterials may offer all-optical solutions for switching and memory in photonic systems, as well as optical detection of increase/decrease of vibration frequencies (chirp) and optical power.

Moreover, reflection and transmission modulation of a membrane-supported metamaterial array is demonstrated when driven by a piezoelectric actuator, achieving up to 9% reflectivity modulation accompanied by 2% transmission modulation when driven across its resonance frequencies. Finally, when the metamaterial array is driven to oscillate at the mechanical resonances of the supporting membrane, the nonlinear response of the membrane is translated to bistability of the metamaterial's optical properties resulting, again, in the emergence of two stable mechanical states.

Chapter 6

Conclusions

6.1 Summary

The hybridization of nanomechanical with optical systems has given rise to nanomechanical photonic metamaterials, a fascinating area of research that, so far, has yielded a number of concept devices providing a wide range of light modulation functionalities in structures of nanoscale thickness. A number of such examples were outlined in Chapter 1 and these provide either tuning or modulation of optical properties and usually consist of beams or cantilevers supporting arrays of optically resonant unit cells. Although tuning of such systems is usually straightforward, mechanically resonating elements introduce additional challenges in a system especially if it consists of multiple resonators as is the case of a nanomechanical metamaterial array. An overlooked aspect of dynamically controlled nanomechanical metamaterials is their mechanical characterization, i.e. the identification of their mechanical eigenfrequencies in order to identify the frequencies at which they can be efficiently driven. This becomes particularly important when the excitation scheme employed engages surrounding elements such as the supporting membrane as demonstrated in Chapter 5.

Detection of fluctuations of a nanomechanical metamaterial's optical properties due to thermomechanical motion is a straightforward approach to accurately pinpoint the mechanical resonance frequencies of its components. Thermomechanical oscillations of the beams constituting the metamaterial lead to modulation of the electromagnetic coupling between the supported optical resonators. The first detection of reflectivity fluctuations of a plasmonic nanomechanical metamaterial is reported in Chapter 3. This is not limited to metal-based optical resonators but also applies in dielectric nanomechanical metamaterials as shown by my collaborator Jinxiang Li.

In Chapter 4, I reported the first demonstration of tuning of mechanical resonances of plasmonic nanomechanical metamaterials via light illumination. This is based on internal stress modulation in the resonating elements that modifies their mechanical resonance frequencies. Photothermal tuning of nanomechanical metamaterials could be exploited in various applications such as temperature sensing, light detection, spectroscopy and in imaging applications. Here, I demonstrated detection of temperature changes due to illumination and I outlined the use of a nanomechanical metamaterial as a bolometer with an optical readout and sub-micron spatial resolution for the first time.

In Chapter 5, I demonstrated excitation of nanomechanical metamaterials in the nonlinear regime. This resulted in the first observation of mechanically bistable oscillations of nanomechanical metamaterial beams allowing both electric and optical switching between the two bistable states. This indicates that mechanically nonlinear, optically resonant structures could serve as low power memory elements in photonic systems.

6.2 Outlook

It is expected that future work will focus on addressing some of the challenges presented here while improving on the proof of concept demonstrations of Chapter 4 and Chapter 5. For instance, in all experimental work outlined in this Thesis it became apparent that the mechanical response of the membrane-based nanomechanical structures will depend largely on their internal stress. It was demonstrated that in arrays consisting of a large number of mechanical oscillators their mechanical resonances are spread over a wide frequency range making identification of the detected resonances challenging. For this reason, simpler systems such as the beam pairs demonstrated in Chapter 4 and Chapter 5 were selected. Such stress variations in the nanomechanical beams induced during the FIB milling raise the issue of appropriate fabrication methods. Although FIB prototyping is fast and involves a minimal number of steps, point by point milling introduces large stress variations in the free-standing membrane. Lithographic processes such as e-beam lithography could result in more uniform stress leading to a more consistent mechanical response across the metamaterial array.

Significant improvements could be made in the nanomechanical micro-bolometer presented in Chapter 4. Ideally, optical readout would be performed by a dedicated readout laser at a wavelength that provides optimal sensitivity of optical properties to displacement. Another idea would be the use of nanomechanical arrays supporting rows of optical elements of gradually changing orientation or size to allow polarimetry or spectroscopy of incident light. A metamaterial based polarimeter has been proposed in [132] but not experimentally demonstrated so far.

In Chapter 5, I demonstrated that excitation of nanomechanical metamaterials via a piezoelectric element not only has the potential for inducing large amplitude light modulation but can also drive the structures in the nonlinear regime where they can operate as mechanical memory elements. However, an issue that was encountered was variations in the response of the piezoelectric across the frequency range of excitation. Therefore, the excitation scheme could be improved by integration of thin piezoelectric films in the nanomechanical framework to provide a more homogeneous response across the frequency range of excitation while at the same time leading to a significant reduction in the overall dimensions of the device. Such an approach would

allow optical as well as electronic readout and moreover, could be employed to study coupling effects between the resonating elements. A basis for such an approach can be found in [182].

Another possible route to excite optically resonant nanomechanical structures could be the use of surface acoustic waves. Such waves can be generated by interdigitated electrodes on piezoelectric substrates and have been used to modulate light propagating in optical waveguides and ring resonators [183]. Phonons in the form of elastic SAWs have been proposed as carriers of quantum information after interaction with a qubit in analogy with photons in quantum optics [184]. More recently, such elastic waves have been used to study coupling interactions between pillar-shaped mechanical resonators [185] and a similar scheme has been proposed as a means of achieving dynamic control of surface phonons by confining elastic energy in subwavelength microstructures [186]. In photonic metamaterials, SAWs could be utilized to mechanically excite arrays of optically resonant nano-pillars consisting of metal or dielectric materials to modulate the optical properties of such arrays at frequencies of 100s of MHz.

Appendix A

Focused ion beam milling

In this work, a dual beam FIB-SEM system (Helios 600 Nanolab) was used for the fabrication of the metamaterial structures. Such a system utilizes two columns, one for FIB milling and an SEM column for sample imaging and process monitoring. Imaging of the sample can be achieved using the SEM column, minimizing Ga^+ ion implantation upon inspection of the milled pattern. In such a dual platform instrument the e-beam column is mounted vertically, and the ion column is mounted at an oblique angle of 52^o. Adjusting the sample stage height at the point where the electron and ion beams coincide (eucentric point) allows for milling and inspection processes to be carried out simultaneously [187].

An FIB microscope generally consists of an ion source, a series of electrostatic and magnetic lenses to shape the ion beam and a scan generator to scan the beam across the sample [187]. The basic operating principle of FIB is the following: high energy ions are directed towards the surface of the sample. Upon collision with the surface, they lose kinetic energy through interactions with the sample electrons (inelastic interactions) and atoms (elastic interactions). These interactions lead to a number of different processes such as: sputtering of sample atoms, electron emission, damage to the sample and sample heating. Inelastic interactions lead to ionization of the sample and electron emission, while elastic interactions lead to displacement of atoms [89, 90].

The ion beam is generated by a liquid-metal ion source from a needle tip by application of a strong electric field. The most typical liquid-metal source used is Ga due to its low melting temperature of 30 ^oC, low volatility and vapour pressure. The extracted ions are then accelerated and focused on the sample by a system of electrostatic lenses. The current of the ion beam is adjusted using apertures. If the energy of a Ga^+ ion (5-30 keV) exceeds the displacement energy of the atom it collides with, this atom will be displaced from its initial position creating a vacancy in the lattice. It is possible that this atom can have enough energy to further dislocate atoms in the lattice leading to the creation of a volume where atoms have excess kinetic energy. If the interaction occurs near the surface of the sample, the displaced atom may be sputtered from the surface (Figure A. 1 (a)) [90].

Similarly to SEM imaging, a focused ion beam can be used to generate images of samples. As the ion beam is raster scanned over the substrate, ion-induced secondary electrons and/or secondary ions that leave the sample are collected on a biased detector (Figure A. 1 (b)). These secondary electrons originate from the top atomic layers of the sample where the incident Ga ions

impact the solid and therefore the emission of such electrons is very sensitive to the surface morphology of the sample. However, imaging with an ion beam will always result in ion implantation and sputtering of the sample surface [90].

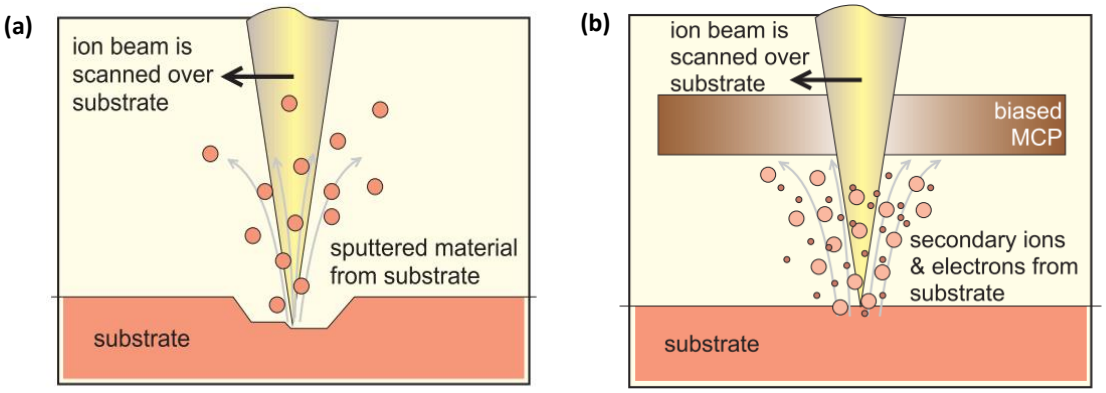

Figure A. 1 Operation principle of focused ion beam. (a) milling. (b) Imaging. (MCP: Multi-channel plate) [89]

Appendix B

Microspectrophotometer

A microspectrophotometer is used to record transmission and reflection spectra of the fabricated metamaterial samples. A microspectrophotometer is essentially a combination of an optical microscope with a spectrophotometer. In our case, the spectrometer can operate in the ultraviolet, visible and near-infrared. Depending on the configuration it can be used to measure reflection, transmission, absorption and fluorescence of μm-sized sample areas [188].

The operation principles of a microspectrophotometer in reflection and transmission mode are described in Figure B. 1. For the reflection mode, white light is emitted from a light source (halogen lamp) and is focused on the sample by the microscope objective. The light reflected from the sample is collected by the objective and directed towards a mirrored aperture. Most of the light is reflected towards an imaging system while the light that passes through the aperture enters the spectrometer. There, an optical grating diffracts the light beam into its spectral components, each one impinging on a pixel of a CCD detector. Thus the intensity of light is plotted as a function of wavelength. The operation in transmission mode is similar, with the difference that the white light is introduced from the bottom of the sample and focused on the sample with a condenser lens. Then, the microscope objective collects the transmitted light.

In this work, a CRAIC microspectrophotometer with an objective numerical aperture of 0.28 (15x objective) was used to record the reflection and transmission spectra of the fabricated free-standing metamaterial arrays. The absorption of the samples was calculated using the relation A = 1-(R+T). The system is equipped with two photodetectors operating at 400-900 nm and 900-2000 nm. A polarizer, positioned after the light source, was used to polarize the incident light during the measurements. A perfect black (Surrey NanoSystems, Vantablack) and a mirror reference are used for calibration of 0% and 100% reflectivity. Blocking of the light path and use of an aperture is used for calibration of 0% and 100% transmission respectively.

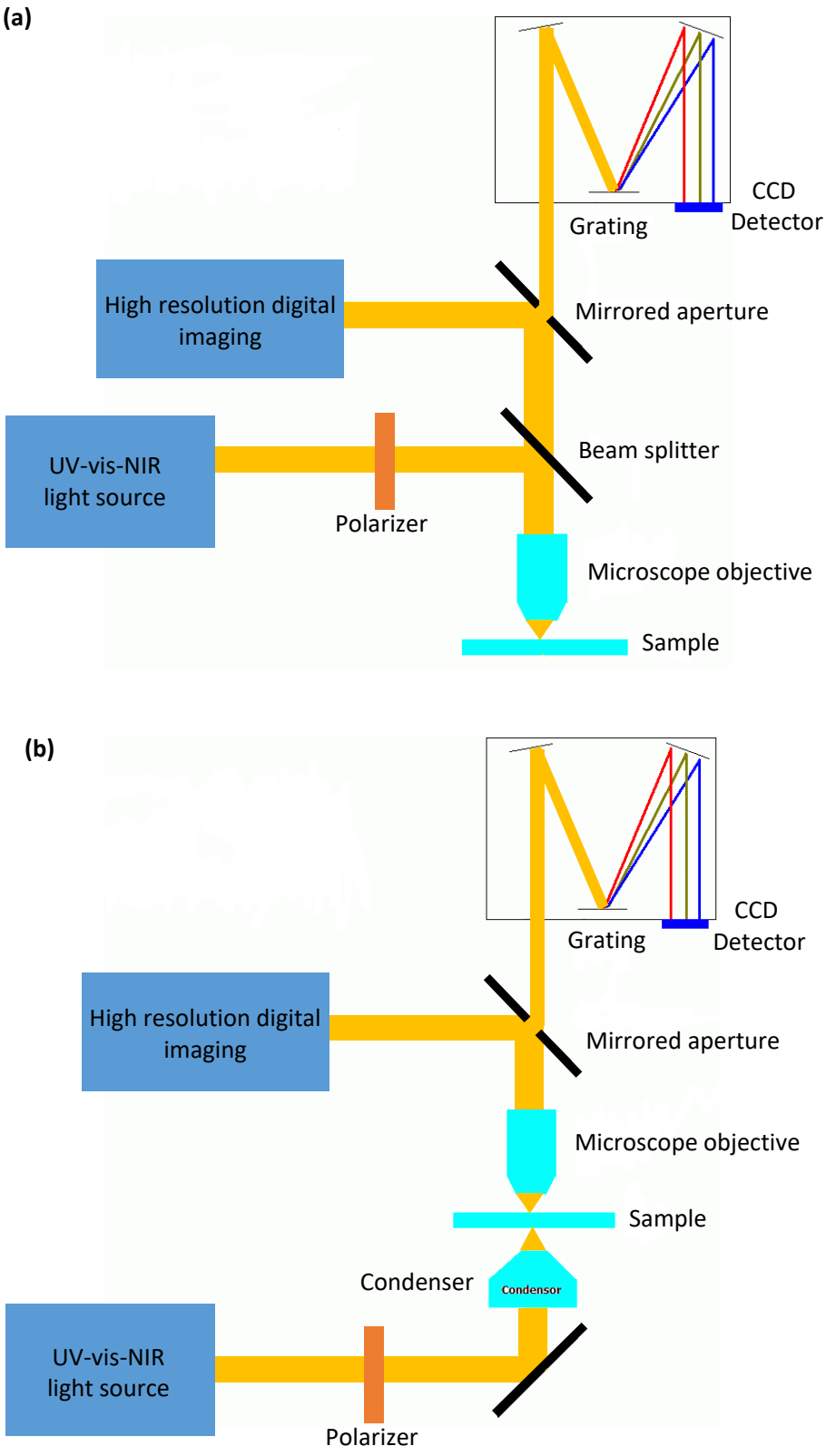

Figure B. 1 Operation principle of a microspectrophotometer. (a) Reflection mode. (b) Transmission mode. [188]

Appendix C

Publications

Articles:

1. **Thermal fluctuations of the optical properties of nanomechanical photonic metamaterials**

J. Li, D. Papas, T. Liu, J. Y. Ou, K. F. MacDonald, E. Plum and N. I. Zheludev

Adv. Opt. Mater., 2101591, 2021

2. **Optomechanical metamaterial nanobolometer**

D. Papas, J. Y. Ou, E. Plum and N. I. Zheludev

APL Photonics, **6**, 126110, 2021

3. **Volatile optical bistability enabled by mechanical nonlinearity**

D. Papas, J. Y. Ou, E. Plum and N. I. Zheludev

arXiv: 2112.11087, 2021

Other articles:

Non-contact optical magnetic field sensor based on metamaterial nanomechanics

G. Lan, J. Y. Ou, D. Papas, N. I. Zheludev and E. Plum

APL Photonics, **7**, 036101, 2022

Conference Contributions:

In cases I am the presented author, my name is underlined

1. (invited) “Picophotonics”, C. Rendón-Barraza, E. A. Chan, J. Li, T. Liu, K. F. MacDonald, J.-Y. Ou, **D. Papas**, N. Papasimakis, E. Plum, T. Pu, G. Yuan, and N. I. Zheludev. 15th International Congress on Artificial Materials for Novel Wave Phenomena, Virtual Meeting, 20-26 Sept 2021

2. (invited) “Metamaterial Nanomachines driven by heat, sound, electric and magnetic fields, and light”, T. Liu, J. Li, **D. Papas**, J. Y. Ou, E. Plum, K. F. MacDonald, and N. I. Zheludev. SPIE Optics & Photonics 2021, Virtual Conference, 1 - 5 Aug 2021

3. (invited) “Dynamics of nanomechanical metamaterials: Pico-vibrometry with light and electron beams”, J. Y. Ou, T. Liu, J. Li, **D. Papas**, E. Plum, K. F. MacDonald, and N. I. Zheludev. META 2021, Virtual Conference, 20 - 23 July 2021

4. (invited) “Nanomechanical photonic metamaterials”, E. Plum, **D. Papas**, J. Li, T. Liu, J. Y. Ou, Q. Zhang, G. Lan, K. F. MacDonald, and N. I. Zheludev. Materials for Humanity (MH21), Virtual Conference, 6-9 July 2021

5. “Flat photonic devices based on nanomechanical metamaterials driven by light, sound, electric and magnetic signals”, J. Li, T. Liu, K. F. MacDonald, J. Y. Ou, **D. Papas**, E. Plum, and N. I. Zheludev. Optical Design and Fabrication Congress, Virtual Conference, 27 Jun - 1 Jul 2021

6. “Nanomechanical Bistability in Photonic Metamaterial”, **D. Papas**, J. Y. Ou, E. Plum and N. I. Zheludev. CLEO/Europe-EQEC 2021 Virtual Meeting, 21 - 25 June 2021

7. “Hybrid bistability in nano-opto-mechanical metamaterial”, **D. Papas**, J. Y. Ou, E. Plum, and N. I. Zheludev. CLEO 2021 Virtual Conference, 9 - 14 May 2021

8. (invited) “Nanomechanical Functionalities in Photonic Metamaterials”,K. F. MacDonald, **D. Papas**, J. Li, Q. Zhang, D. Piccinotti, J. Y. Ou, E. Plum, and N. I. Zheludev. Metamaterials 2020 (Virtual Conference), 28 Sept – 01 Oct 2020

9. “Exotic effects in nanomechanical metamaterials”, J. Y. Ou, **D. Papas**, J. Li, T. Liu, Q. Zhang, D. Piccinotti, E. Plum and K. F. MacDonald, and N. I. Zheludev. SPIE Optics & Photonics 2020, Digital Forum, 23 - 27 Aug 2020

10. (invited) “Functional nanomechanical metamaterials driven by light, electromagnetic forces and sound”, N. I. Zheludev, **D. Papas**, T. Liu, J. Li, Q. Zhang, J. Y. Ou, E. Plum, and K. F. MacDonald. CLEO 2020 Virtual Conference, 11-15 May 2020

11. “Optical metamaterial reconfigured with sound”, **D. Papas**, J. Y. Ou, E. Plum, and N. I. Zheludev. Metamaterials'2019, Rome, Italy, 16 - 21 Sep 2019

12. (invited) “Advances in nanomechanical metamaterials”, E. Plum, **D. Papas**, J. Y. Ou, A. Karvounis, K. F. MacDonald and N. I. Zheludev. META 2019, Lisbon, Portugal, 23-26 Jul 2019

13. (poster) “Acoustically driven photonic metamaterials”, **D. Papas**, J. Y. Ou, E. Plum, and N. I. Zheludev. Nanometa 2019, Seefeld, Austria, 3 - 6 Jan 2019

14. (invited) “Nano-optomechanical metamaterials”, J. Y. Ou, **D. Papas**, A. Karvounis, E. Plum, and N. I. Zheludev, Optics 2018, Annual Meeting of Taiwan Photonics Society, Taiwan, 6-8 Dec 2018

15. “Playing the metamaterial guitar with light and ultrasound”, J. Y. Ou, **D. Papas**, E. Plum, and N. I. Zheludev. Symposium on Acoustic Metamaterials, Xàtiva, Spain, 7-9 Nov 2018

Bibliography

1. A. Boardman, "Pioneers in metamaterials: John Pendry and Victor Veselago"*, Journal of Optics*, **13** (2), 020401, 2010.

2. V.M. Shalaev and W. Cai, "Optical metamaterials: Fundamentals and applications", Springer, 2010.

3. V.G. Veselago, "The electrodynamics of substances with simultaneously negative values of ε and μ"*, Soviet Physics Uspekhi*, **10** (4), 509, 1968.

4. D.R. Smith, W.J. Padilla, D.C. Vier, S.C. Nemat-Nasser and S. Schultz, "Composite medium with simultaneously negative permeability and permittivity"*, Physical Review Letters*, **84** (18), 4184-4187, 2000.

5. R.A. Shelby, D.R. Smith and S. Schultz, "Experimental verification of a negative index of refraction"*, Science*, **292** (5514), 77-79, 2001.

6. J.B. Pendry, "Negative refraction makes a perfect lens"*, Physical Review Letters*, **85** (18), 3966-3969, 2000.

7. J.B. Pendry, D. Schurig and D.R. Smith, "Controlling electromagnetic fields"*, Science*, **312** (5781), 1780, 2006.

8. J.B. Pendry, A.J. Holden, D.J. Robbins and W.J. Stewart, "Magnetism from conductors and enhanced nonlinear phenomena"*, IEEE Transactions on Microwave Theory and Techniques*, **47** (11), 2075-2084, 1999.

9. S. Linden, C. Enkrich, M. Wegener, J. Zhou, T. Koschny and C.M. Soukoulis, "Magnetic response of metamaterials at 100 terahertz"*, Science*, **306** (5700), 1351, 2004.

10. K. Yao and Y. Liu, "Plasmonic metamaterials"*, Nanotechnology Reviews*, **3** (2), 177-210, 2014.

11. S. Jahani and Z. Jacob, "All-dielectric metamaterials"*, Nature Nanotechnology*, **11** (1), 23-36, 2016.

12. A.I. Kuznetsov, A.E. Miroshnichenko, M.L. Brongersma, Y.S. Kivshar and B. Luk'yanchuk, "Optically resonant dielectric nanostructures"*, Science*, **354** (6314), aag2472, 2016.

13. V. Savinov and N.I. Zheludev, "High-quality metamaterial dispersive grating on the facet of an optical fiber"*, Applied Physics Letters*, **111** (9), 091106, 2017.

14. A.Q. Liu, W.M. Zhu, D.P. Tsai and N.I. Zheludev, "Micromachined tunable metamaterials: A review"*, Journal of Optics*, **14** (11), 114009, 2012.

15. I.V. Shadrivov, A.B. Kozyrev, D.v.d. Weide and Y.S. Kivshar, "Nonlinear magnetic metamaterials"*, Optics Express*, **16** (25), 20266-20271, 2008.

16. M.J. Dicken, K. Aydin, I.M. Pryce, L.A. Sweatlock, E.M. Boyd, S. Walavalkar, J. Ma and H.A. Atwater, "Frequency tunable near-infrared metamaterials based on VO_2 phase transition"*, Optics Express*, **17** (20), 18330-18339, 2009.

17. T. Driscoll, H.-T. Kim, B.-G. Chae, B.-J. Kim, Y.-W. Lee, N.M. Jokerst, S. Palit, D.R. Smith, M. Di Ventra and D.N. Basov, "Memory metamaterials"*, Science*, **325** (5947), 1518, 2009.

18. Z.L. Sámson, K.F. MacDonald, F. De Angelis, B. Gholipour, K. Knight, C.C. Huang, E. Di Fabrizio, D.W. Hewak and N.I. Zheludev, "Metamaterial electro-optic switch of nanoscale thickness"*, Applied Physics Letters*, **96** (14), 143105, 2010.

19. B. Gholipour, J. Zhang, K.F. MacDonald, D.W. Hewak and N.I. Zheludev, "An all-optical, non-volatile, bidirectional, phase-change meta-switch"*, Advanced Materials*, **25** (22), 3050-3054, 2013.

20. R.F. Waters, P.A. Hobson, K.F. MacDonald and N.I. Zheludev, "Optically switchable photonic metasurfaces"*, Applied Physics Letters*, **107** (8), 081102, 2015.

21. Q. Wang, E.T.F. Rogers, B. Gholipour, C.-M. Wang, G. Yuan, J. Teng and N.I. Zheludev, "Optically reconfigurable metasurfaces and photonic devices based on phase change materials"*, Nature Photonics*, **10** (1), 60-65, 2016.

22. A. Karvounis, B. Gholipour, K.F. MacDonald and N.I. Zheludev, "All-dielectric phase-change reconfigurable metasurface"*, Applied Physics Letters*, **109** (5), 051103, 2016.

23. Q. Zhao, L. Kang, B. Du, B. Li, J. Zhou, H. Tang, X. Liang and B. Zhang, "Electrically tunable negative permeability metamaterials based on nematic liquid crystals"*, Applied Physics Letters*, **90** (1), 011112, 2007.

24. D. Shrekenhamer, W.-C. Chen and W.J. Padilla, "Liquid crystal tunable metamaterial absorber"*, Physical Review Letters*, **110** (17), 177403, 2013.

25. O. Buchnev, J.Y. Ou, M. Kaczmarek, N.I. Zheludev and V.A. Fedotov, "Electro-optical control in a plasmonic metamaterial hybridised with a liquid-crystal cell"*, Optics Express*, **21** (2), 1633-1638, 2013.

26. M. Decker, C. Kremers, A. Minovich, I. Staude, A.E. Miroshnichenko, D. Chigrin, D.N. Neshev, C. Jagadish and Y.S. Kivshar, "Electro-optical switching by liquid-crystal controlled metasurfaces"*, Optics Express*, **21** (7), 8879-8885, 2013.

27. O. Buchnev, N. Podoliak, M. Kaczmarek, N.I. Zheludev and V.A. Fedotov, "Electrically controlled nanostructured metasurface loaded with liquid crystal: Toward multifunctional photonic switch"*, Advanced Optical Materials*, **3** (5), 674-679, 2015.

28. O. Buchnev, N. Podoliak and V.A. Fedotov, "Liquid crystal-filled meta-pixel with switchable asymmetric reflectance and transmittance"*, Journal of Molecular Liquids*, **267**, 411-414, 2018.

29. S.-Q. Li, X. Xu, R. Maruthiyodan Veetil, V. Valuckas, R. Paniagua-Domínguez and A.I. Kuznetsov, "Phase-only transmissive spatial light modulator based on tunable dielectric metasurface"*, Science*, **364** (6445), 1087, 2019.

30. O. Buchnev, N. Podoliak, K. Kaltenecker, M. Walther and V.A. Fedotov, "Metasurface-based optical liquid crystal cell as an ultrathin spatial phase modulator for THz applications"*, ACS Photonics*, **7** (11), 3199-3206, 2020.

31. R.E. Simpson, P. Fons, A.V. Kolobov, T. Fukaya, M. Krbal, T. Yagi and J. Tominaga, "Interfacial phase-change memory"*, Nature Nanotechnology*, **6** (8), 501-505, 2011.

32. N.I. Zheludev and Y.S. Kivshar, "From metamaterials to metadevices"*, Nat Mater*, **11** (11), 917-24, 2012.

33. M. Lapine, D. Powell, M. Gorkunov, I. Shadrivov, R. Marqués and Y. Kivshar, "Structural tunability in metamaterials"*, Applied Physics Letters*, **95** (8), 084105, 2009.

34. I.M. Pryce, K. Aydin, Y.A. Kelaita, R.M. Briggs and H.A. Atwater, "Highly strained compliant optical metamaterials with large frequency tunability", *Nano Letters*, **10** (10), 4222-4227, 2010.

35. S. Aksu, M. Huang, A. Artar, A.A. Yanik, S. Selvarasah, M.R. Dokmeci and H. Altug, "Flexible plasmonics on unconventional and nonplanar substrates", *Advanced Materials*, **23** (38), 4422-4430, 2011.

36. P. Gutruf, C. Zou, W. Withayachumnankul, M. Bhaskaran, S. Sriram and C. Fumeaux, "Mechanically tunable dielectric resonator metasurfaces at visible frequencies", *ACS Nano*, **10** (1), 133-141, 2016.

37. H.-S. Ee and R. Agarwal, "Tunable metasurface and flat optical zoom lens on a stretchable substrate", *Nano Letters*, **16** (4), 2818-2823, 2016.

38. H. Tao, A.C. Strikwerda, K. Fan, W.J. Padilla, X. Zhang and R.D. Averitt, "Reconfigurable terahertz metamaterials", *Phys Rev Lett*, **103** (14), 147401, 2009.

39. J.Y. Ou, E. Plum, L. Jiang and N.I. Zheludev, "Reconfigurable photonic metamaterials", *Nano Lett*, **11** (5), 2142-4, 2011.

40. Y. Nagasaki, B. Gholipour, J.-Y. Ou, M. Tsuruta, E. Plum, K.F. MacDonald, J. Takahara and N.I. Zheludev, "Optical bistability in shape-memory nanowire metamaterial array", *Applied Physics Letters*, **113** (2), 021105, 2018.

41. A. Karvounis, N. Aspiotis, I. Zeimpekis, J.-Y. Ou, C.-C. Huang, D. Hewak and N.I. Zheludev, "Mechanochromic reconfigurable metasurfaces", *Advanced Science*, **6** (21), 1900974, 2019.

42. J. Valente, J.-Y. Ou, E. Plum, I.J. Youngs and N.I. Zheludev, "Reconfiguring photonic metamaterials with currents and magnetic fields", *Applied Physics Letters*, **106** (11), 111905, 2015.

43. J.-Y. Ou, E. Plum, J. Zhang and N.I. Zheludev, "An electromechanically reconfigurable plasmonic metamaterial operating in the near-infrared", *Nature Nanotechnology*, **8** (4), 252-255, 2013.

44. A. Karvounis, B. Gholipour, K.F. MacDonald and N.I. Zheludev, "Giant electro-optical effect through electrostriction in a nanomechanical metamaterial", *Adv Mater*, **31** (1), e1804801, 2019.

45. J. Valente, J.-Y. Ou, E. Plum, I.J. Youngs and N.I. Zheludev, "A magneto-electro-optical effect in a plasmonic nanowire material", *Nature Communications*, **6** (1), 7021, 2015.

46. M. Li, W.H.P. Pernice, C. Xiong, T. Baehr-Jones, M. Hochberg and H.X. Tang, "Harnessing optical forces in integrated photonic circuits", *Nature*, **456** (7221), 480-484, 2008.

47. G.S. Wiederhecker, L. Chen, A. Gondarenko and M. Lipson, "Controlling photonic structures using optical forces", *Nature*, **462** (7273), 633-636, 2009.

48. P.B. Deotare, I. Bulu, I.W. Frank, Q. Quan, Y. Zhang, R. Ilic and M. Loncar, "All optical reconfiguration of optomechanical filters", *Nature Communications*, **3** (1), 846, 2012.

49. M. Bagheri, M. Poot, M. Li, W.P.H. Pernice and H.X. Tang, "Dynamic manipulation of nanomechanical resonators in the high-amplitude regime and non-volatile mechanical memory operation", *Nature Nanotechnology*, **6** (11), 726-732, 2011.

50. B. Dong, H. Cai, L.K. Chin, J.G. Huang, Z.C. Yang, Y.D. Gu, G.I. Ng, W. Ser, D.L. Kwong and A.Q. Liu, "A silicon-nanowire memory driven by optical gradient force induced bistability", *Applied Physics Letters*, **107** (26), 261111, 2015.

51. J.F. Tao, J. Wu, H. Cai, Q.X. Zhang, J.M. Tsai, J.T. Lin and A.Q. Liu, "A nanomachined optical logic gate driven by gradient optical force", *Applied Physics Letters*, **100** (11), 113104, 2012.

52. Y.Y. Tanaka, P. Albella, M. Rahmani, V. Giannini, S.A. Maier and T. Shimura, "Plasmonic linear nanomotor using lateral optical forces", *Science Advances*, **6** (45), eabc3726, 2020.

53. R. Zhao, P. Tassin, T. Koschny and C.M. Soukoulis, "Optical forces in nanowire pairs and metamaterials", *Optics Express*, **18** (25), 25665-25676, 2010.

54. J. Zhang, K.F. MacDonald and N.I. Zheludev, "Nonlinear dielectric optomechanical metamaterials", *Light: Science & Applications*, **2** (8), e96-e96, 2013.

55. J. Zhang, K.F. MacDonald and N.I. Zheludev, "Giant optical forces in planar dielectric photonic metamaterials", *Optics Letters*, **39** (16), 4883-4886, 2014.

56. J.-Y. Ou, E. Plum, J. Zhang and N.I. Zheludev, "Giant nonlinearity of an optically reconfigurable plasmonic metamaterial", *Advanced Materials*, **28** (4), 729-733, 2016.

57. S. Zhang, D.A. Genov, Y. Wang, M. Liu and X. Zhang, "Plasmon-induced transparency in metamaterials", *Physical Review Letters*, **101** (4), 047401, 2008.

58. N. Verellen, Y. Sonnefraud, H. Sobhani, F. Hao, V.V. Moshchalkov, P.V. Dorpe, P. Nordlander and S.A. Maier, "Fano resonances in individual coherent plasmonic nanocavities", *Nano Letters*, **9** (4), 1663-1667, 2009.

59. N. Liu, L. Langguth, T. Weiss, J. Kästel, M. Fleischhauer, T. Pfau and H. Giessen, "Plasmonic analogue of electromagnetically induced transparency at the Drude damping limit", *Nature Materials*, **8** (9), 758-762, 2009.

60. B. Luk'yanchuk, N.I. Zheludev, S.A. Maier, N.J. Halas, P. Nordlander, H. Giessen and C.T. Chong, "The Fano resonance in plasmonic nanostructures and metamaterials", *Nature Materials*, **9** (9), 707-715, 2010.

61. A. Karvounis, J.-Y. Ou, W. Wu, K.F. MacDonald and N.I. Zheludev, "Nano-optomechanical nonlinear dielectric metamaterials", *Applied Physics Letters*, **107** (19), 191110, 2015.

62. T. Shimura, T. Kinoshita, Y. Koto, N. Umeda and K. Iwami, "Birefringent reconfigurable metasurface at visible wavelengths by MEMS nanograting", *Applied Physics Letters*, **113** (17), 171905, 2018.

63. T. Kan, A. Isozaki, N. Kanda, N. Nemoto, K. Konishi, H. Takahashi, M. Kuwata-Gonokami, K. Matsumoto and I. Shimoyama, "Enantiomeric switching of chiral metamaterial for terahertz polarization modulation employing vertically deformable MEMS spirals", *Nature Communications*, **6** (1), 8422, 2015.

64. K. Yamaguchi, M. Fujii, T. Okamoto and M. Haraguchi, "Electrically driven plasmon chip: Active plasmon filter", *Applied Physics Express*, **7** (1), 012201, 2013.

65. T. Roy, S. Zhang, I.W. Jung, M. Troccoli, F. Capasso and D. Lopez, "Dynamic metasurface lens based on MEMS technology", *APL Photonics*, **3** (2), 021302, 2018.

66. N.I. Zheludev, "Obtaining optical properties on demand", *Science*, **348** (6238), 973, 2015.

67. W. Zhu, Q. Song, L. Yan, W. Zhang, P.-C. Wu, L.K. Chin, H. Cai, D.P. Tsai, Z.X. Shen, T.W. Deng, S.K. Ting, Y. Gu, G.Q. Lo, D.L. Kwong, Z.C. Yang, R. Huang, A.-Q. Liu, and N. Zheludev, "A flat lens with tunable phase gradient by using random access reconfigurable metamaterial", *Advanced Materials*, **27** (32), 4739-4743, 2015.

68. P. Cencillo-Abad, J.-Y. Ou, E. Plum, J. Valente and N.I. Zheludev, "Random access actuation of nanowire grid metamaterial", *Nanotechnology*, **27** (48), 485206, 2016.

69. P. Cencillo-Abad, E. Plum, E.T.F. Rogers and N.I. Zheludev, "Spatial optical phase-modulating metadevice with subwavelength pixelation", *Optics Express*, **24** (16), 18790-18798, 2016.

70. J.-Y. Ou, E. Plum and N.I. Zheludev, "Optical addressing of nanomechanical metamaterials with subwavelength resolution", *Applied Physics Letters*, **113** (8), 081104, 2018.

71. J.D. Thompson, B.M. Zwickl, A.M. Jayich, F. Marquardt, S.M. Girvin and J.G.E. Harris, "Strong dispersive coupling of a high-finesse cavity to a micromechanical membrane", *Nature*, **452** (7183), 72-75, 2008.

72. S. Stapfner, L. Ost, D. Hunger, J. Reichel, I. Favero and E.M. Weig, "Cavity-enhanced optical detection of carbon nanotube brownian motion", *Applied Physics Letters*, **102** (15), 151910, 2013.

73. M. Eichenfield, R. Camacho, J. Chan, K.J. Vahala and O. Painter, "A picogram- and nanometre-scale photonic-crystal optomechanical cavity", *Nature*, **459** (7246), 550-555, 2009.

74. M. Li, W.H.P. Pernice and H.X. Tang, "Broadband all-photonic transduction of nanocantilevers", *Nature Nanotechnology*, **4** (6), 377-382, 2009.

75. R. Thijssen, E. Verhagen, T.J. Kippenberg and A. Polman, "Plasmon nanomechanical coupling for nanoscale transduction", *Nano Letters*, **13** (7), 3293-3297, 2013.

76. R. Thijssen, T.J. Kippenberg, A. Polman and E. Verhagen, "Parallel transduction of nanomechanical motion using plasmonic resonators", *ACS Photonics*, **1** (11), 1181-1188, 2014.

77. R. Thijssen, T.J. Kippenberg, A. Polman and E. Verhagen, "Plasmomechanical resonators based on dimer nanoantennas", *Nano Letters*, **15** (6), 3971-3976, 2015.

78. S. Schmid, L.G. Villanueva and M.L. Roukes, *Fundamentals of nanomechanical resonators*. 2016, Cham: Springer International Publishing.

79. J. Lee, Z. Wang, K. He, J. Shan and P.X.L. Feng, "High frequency MoS_2 nanomechanical resonators", *ACS Nano*, **7** (7), 6086-6091, 2013.

80. M. Kumar and H. Bhaskaran, "Ultrasensitive room-temperature piezoresistive transduction in graphene-based nanoelectromechanical systems", *Nano Letters*, **15** (4), 2562-2567, 2015.

81. J.Y. Ou, *Reconfigurable photonic metamaterials*, University of Southampton, Doctoral thesis, 2014.

82. R. Thijssen, *Plasmonic nanomechanical transduction*, University of Amsterdam, Doctoral thesis, 2014.

83. B.D. Hauer, C. Doolin, K.S.D. Beach and J.P. Davis, "A general procedure for thermomechanical calibration of nano/micro-mechanical resonators", *Annals of Physics*, **339**, 181-207, 2013.

84. A.N. Cleland, *Foundations of nanomechanics*. 2003, Berlin, Heidelberg: Springer Berlin Heidelberg.

85. K.B. Gavan, *Dynamic characterization of silicon nitride cantilevers*, TU Delft, Doctoral thesis, 2009.

86. B.J. Roxworthy and V.A. Aksyuk, "Nanomechanical motion transduction with a scalable localized gap plasmon architecture", *Nature Communications*, **7** (1), 13746, 2016.

87. M. Aspelmeyer, T.J. Kippenberg and F. Marquardt, *Cavity optomechanics nano- and micromechanical resonators interacting with light*. 2014, Berlin: Springer-Verlag Gmb, H.

88. G. Meyer and N.M. Amer, "Novel optical approach to atomic force microscopy", *Applied Physics Letters*, **53** (12), 1045-1047, 1988.

89. S. Reyntjens and R. Puers, "A review of focused ion beam applications in microsystem technology", *Journal of Micromechanics and Microengineering*, **11** (4), 287-300, 2001.

90. C.A. Volkert and A.M. Minor, "Focused ion beam microscopy and micromachining", *MRS Bulletin*, **32** (5), 389-399, 2007.

91. P. Nagpal, N.C. Lindquist, S.-H. Oh and D.J. Norris, "Ultrasmooth patterned metals for plasmonics and metamaterials", *Science*, **325** (5940), 594, 2009.

92. Z. Liu, A. Boltasseva, R.H. Pedersen, R. Bakker, A.V. Kildishev, V.P. Drachev and V.M. Shalaev, "Plasmonic nanoantenna arrays for the visible", *Metamaterials*, **2** (1), 45-51, 2008.

93. P. Cencillo-Abad, J.-Y. Ou, E. Plum and N.I. Zheludev, "Electro-mechanical light modulator based on controlling the interaction of light with a metasurface", *Scientific Reports*, **7** (1), 5405, 2017.

94. N. Papasimakis and N.I. Zheludev, "Metamaterial-induced transparency: Sharp Fano resonances and slow light", *Optics and Photonics News*, **20** (10), 22-27, 2009.

95. Z.-G. Dong, H. Liu, M.-X. Xu, T. Li, S.-M. Wang, S.-N. Zhu and X. Zhang, "Plasmonically induced transparent magnetic resonance in a metallic metamaterial composed of asymmetric double bars", *Optics Express*, **18** (17), 18229-18234, 2010.

96. A.E. Miroshnichenko, S. Flach and Y.S. Kivshar, "Fano resonances in nanoscale structures", *Reviews of Modern Physics*, **82** (3), 2257-2298, 2010.

97. J. Zhao, J. Zhang, Z. Zhu, X. Yuan and S. Qin, "Fano resonances and strong field enhancements in arrays of asymmetric plasmonic gap-antennas", *Journal of Optics*, **17** (8), 085002, 2015.

98. Y. Moritake, Y. Kanamori and K. Hane, "Experimental demonstration of sharp Fano resonance in optical metamaterials composed of asymmetric double bars", *Optics Letters*, **39** (13), 4057-4060, 2014.

99. K.L. Ekinci, Y.T. Yang and M.L. Roukes, "Ultimate limits to inertial mass sensing based upon nanoelectromechanical systems", *Journal of Applied Physics*, **95** (5), 2682-2689, 2004.

100. Y.T. Yang, C. Callegari, X.L. Feng, K.L. Ekinci and M.L. Roukes, "Zeptogram-scale nanomechanical mass sensing", *Nano Letters*, **6** (4), 583-586, 2006.

101. H.-Y. Chiu, P. Hung, H.W.C. Postma and M. Bockrath, "Atomic-scale mass sensing using carbon nanotube resonators", *Nano Letters*, **8** (12), 4342-4346, 2008.

102. J. Chaste, A. Eichler, J. Moser, G. Ceballos, R. Rurali and A. Bachtold, "A nanomechanical mass sensor with yoctogram resolution", *Nature Nanotechnology*, **7** (5), 301-304, 2012.

103. A.K. Naik, M.S. Hanay, W.K. Hiebert, X.L. Feng and M.L. Roukes, "Towards single-molecule nanomechanical mass spectrometry", *Nature Nanotechnology*, **4** (7), 445-450, 2009.

104. M.S. Hanay, S. Kelber, A.K. Naik, D. Chi, S. Hentz, E.C. Bullard, E. Colinet, L. Duraffourg and M.L. Roukes, "Single-protein nanomechanical mass spectrometry in real time", *Nature Nanotechnology*, **7** (9), 602-608, 2012.

105. S. Yamada, S. Schmid, T. Larsen, O. Hansen and A. Boisen, "Photothermal infrared spectroscopy of airborne samples with mechanical string resonators", *Analytical Chemistry*, **85** (21), 10531-10535, 2013.

106. T. Kenny, "Nanometer-scale force sensing with mems devices", *IEEE Sensors Journal*, **1** (2), 148, 2001.

107. E. Gavartin, P. Verlot and T.J. Kippenberg, "A hybrid on-chip optomechanical transducer for ultrasensitive force measurements", *Nature Nanotechnology*, **7** (8), 509-514, 2012.

108. J. Moser, J. Güttinger, A. Eichler, M.J. Esplandiu, D.E. Liu, M.I. Dykman and A. Bachtold, "Ultrasensitive force detection with a nanotube mechanical resonator", *Nature Nanotechnology*, **8** (7), 493-496, 2013.

109. A.K. Pandey, O. Gottlieb, O. Shtempluck and E. Buks, "Performance of an AuPd micromechanical resonator as a temperature sensor", *Applied Physics Letters*, **96** (20), 203105, 2010.

110. T. Larsen, S. Schmid, L. Grönberg, A.O. Niskanen, J. Hassel, S. Dohn and A. Boisen, "Ultrasensitive string-based temperature sensors", *Applied Physics Letters*, **98** (12), 121901, 2011.

111. T. Larsen, S. Schmid and A. Boisen, "Micro string resonators as temperature sensors", *AIP Conference Proceedings*, **1552** (1), 931-936, 2013.

112. X.C. Zhang, E.B. Myers, J.E. Sader and M.L. Roukes, "Nanomechanical torsional resonators for frequency-shift infrared thermal sensing", *Nano Letters*, **13** (4), 1528-1534, 2013.

113. Y. Hui, J.S. Gomez-Diaz, Z. Qian, A. Alù and M. Rinaldi, "Plasmonic piezoelectric nanomechanical resonator for spectrally selective infrared sensing", *Nature Communications*, **7** (1), 11249, 2016.

114. L. Laurent, J.-J. Yon, J.-S. Moulet, M. Roukes and L. Duraffourg, "12 µm-pitch electromechanical resonator for thermal sensing", *Physical Review Applied*, **9** (2), 024016, 2018.

115. A. Blaikie, D. Miller and B.J. Alemán, "A fast and sensitive room-temperature graphene nanomechanical bolometer", *Nature Communications*, **10** (1), 4726, 2019.

116. M.H. Matheny, L.G. Villanueva, R.B. Karabalin, J.E. Sader and M.L. Roukes, "Nonlinear mode-coupling in nanomechanical systems", *Nano Letters*, **13** (4), 1622-1626, 2013.

117. H. Okamoto, R. Schilling, H. Schütz, V. Sudhir, D.J. Wilson, H. Yamaguchi and T.J. Kippenberg, "A strongly coupled Λ-type micromechanical system", *Applied Physics Letters*, **108** (15), 153105, 2016.

118. L. Zhang, T. Tian, P. Huang, S. Lin and J. Du, "Coherent transfer of excitation in a nanomechanical artificial lattice*", *Chinese Physics Letters*, **37** (1), 014501, 2020.

119. S.C. Jun, X.M.H. Huang, M. Manolidis, C.A. Zorman, M. Mehregany and J. Hone, "Electrothermal tuning of Al–SiC nanomechanical resonators", *Nanotechnology*, **17** (5), 1506-1511, 2006.

120. S. Schmid, K. Wu, P.E. Larsen, T. Rindzevicius and A. Boisen, "Low-power photothermal probing of single plasmonic nanostructures with nanomechanical string resonators", *Nano Letters*, **14** (5), 2318-2321, 2014.

121. B.J. Roxworthy, S. Vangara and V.A. Aksyuk, "Subdiffraction spatial mapping of nanomechanical modes using a plasmomechanical system", *ACS Photonics*, **5** (9), 3658-3665, 2018.

122. V.P. Rangacharya, K. Wu, P.E. Larsen, L.H.E. Thamdrup, O. Ilchenko, E.-T. Hwu, T. Rindzevicius and A. Boisen, "Quantifying optical absorption of single plasmonic nanoparticles and nanoparticle dimers using microstring resonators", *ACS Sensors*, **5** (7), 2067-2075, 2020.

123. H. Ftouni, C. Blanc, D. Tainoff, A.D. Fefferman, M. Defoort, K.J. Lulla, J. Richard, E. Collin and O. Bourgeois, "Thermal conductivity of silicon nitride membranes is not sensitive to stress", *Physical Review B*, **92** (12), 125439, 2015.

124. P.L. Yu, T.P. Purdy and C.A. Regal, "Control of material damping in high-Q membrane microresonators", *Physical Review Letters*, **108** (8), 083603, 2012.

125. A.H. Ghadimi, S.A. Fedorov, N.J. Engelsen, M.J. Bereyhi, R. Schilling, D.J. Wilson and T.J. Kippenberg, "Elastic strain engineering for ultralow mechanical dissipation", *Science*, **360** (6390), 764, 2018.

126. S.A. Fedorov, N.J. Engelsen, A.H. Ghadimi, M.J. Bereyhi, R. Schilling, D.J. Wilson and T.J. Kippenberg, "Generalized dissipation dilution in strained mechanical resonators", *Physical Review B*, **99** (5), 054107, 2019.

127. S.S. Verbridge, D.F. Shapiro, H.G. Craighead and J.M. Parpia, "Macroscopic tuning of nanomechanics: Substrate bending for reversible control of frequency and quality factor of nanostring resonators", *Nano Letters*, **7** (6), 1728-1735, 2007.

128. M.J. Bereyhi, A. Beccari, S.A. Fedorov, A.H. Ghadimi, R. Schilling, D.J. Wilson, N.J. Engelsen and T.J. Kippenberg, "Clamp-tapering increases the quality factor of stressed nanobeams", *Nano Letters*, **19** (4), 2329-2333, 2019.

129. P.L. Richards, "Bolometers for infrared and millimeter waves", *Journal of Applied Physics*, **76** (1), 1-24, 1994.

130. A. Varpula, K. Tappura, J. Tiira, K. Grigoras, O.-P. Kilpi, K. Sovanto, J. Ahopelto and M. Prunnila, "Nano-thermoelectric infrared bolometers", *APL Photonics*, **6** (3), 036111, 2021.

131. U. Sassi, R. Parret, S. Nanot, M. Bruna, S. Borini, D. De Fazio, Z. Zhao, E. Lidorikis, F.H.L. Koppens, A.C. Ferrari, and A. Colli, "Graphene-based mid-infrared room-temperature pyroelectric bolometers with ultrahigh temperature coefficient of resistance", *Nature Communications*, **8** (1), 14311, 2017.

132. F.B.P. Niesler, J.K. Gansel, S. Fischbach and M. Wegener, "Metamaterial metal-based bolometers", *Appl. Phys. Lett.*, **100**, 203508, 2012.

133. Y. Kim, D. Kim, S.-H. Lee, M. Seo, H.J. Jung, B. Kang, S.-M. Lee and H.-J. Lee "Single-layer metamaterial bolometer for sensitive detection of low-power terahertz waves at room temperature"*, Opt. Express*, **28** (12), 17143, 2020.

134. V. Savinov, V.A. Fedotov, P.A.J. de Groot and N.I. Zheludev, "Radiation-harvesting resonant superconducting sub-THz metamaterial bolometer"*, Supercond. Sci. Technol.*, **26**, 084001, 2013.

135. I.E. Carranza, J. Grant, J. Gough and D.R.S. Cumming, "Metamaterial-based terahertz imaging"*, IEEE Transactions on Terahertz Science and Technology*, **5** (6), 892, 2015.

136. J. Grant, I. Escorcia Carranza, C. Li, I. McCrindle and D. Cumming, "A monolithic resonant terahertz sensor element comprising a metamaterial absorber and micro-bolometer"*, Laser and Photonics Reviews*, **7** (6), 1043, 2013.

137. H. Tao, E.A. Kadlec, A.C. Strikwerda, K. Fan, W.J. Padilla, R.D. Averitt, E.A. Shaner and X. Zhang, "Microwave and terahertz wave sensing with metamaterials"*, Optics Express*, **19** (22), 21620-21626, 2011.

138. Z. Qian, V. Rajaram, S. Kang and M. Rinaldi, "High figure-of-merit NEMS thermal detectors based on 50-nm thick AlN nano-plate resonators"*, Applied Physics Letters*, **115** (26), 261102, 2019.

139. F. Niklaus, C. Vieider and H. Jakobsen, “MEMS-based uncooled infrared bolometer arrays: A review”, *Photonics asia* 2007, **6836**, 2008: SPIE.

140. G. Skidmore, C.J. Han and C. Li, “Uncooled microbolometers at DRS and elsewhere through 2013”, *Spie sensing technology + applications*, **9100**, 2014: SPIE.

141. M.Y. Tanrikulu, Y. Ç, A.K. Okyay, O. Akar, A. Saraç and T. Akin, "Realization of single layer microbolometer detector pixel using ZnO material"*, IEEE Sensors Journal*, **20** (17), 9677-9684, 2020.

142. R. Kokkoniemi, J. Govenius, V. Vesterinen, R.E. Lake, A.M. Gunyhó, K.Y. Tan, S. Simbierowicz, L. Grönberg, J. Lehtinen, M. Prunnila, J. Hassel, A. Lamminen, O.-P. Saira, and M. Möttönen, "Nanobolometer with ultralow noise equivalent power"*, Communications Physics*, **2** (1), 124, 2019.

143. H.-H. Yang and G.M. Rebeiz, "Sub-10 pw/hz$^{0.5}$ room temperature Ni nano-bolometer"*, Applied Physics Letters*, **108** (5), 053106, 2016.

144. T. Liu, J.-Y. Ou, E. Plum, K.F. MacDonald and N.I. Zheludev, "Visualization of subatomic movements in nanostructures"*, Nano Letters*, **21** (18), 7746-7752, 2021.

145. H.M. Gibbs, *Optical bistability: Controlling light with light*. 1985: Academic Press, Inc.,Orlando, FL.

146. H.M. Gibbs, S.L. McCall and T.N.C. Venkatesan, "Differential gain and bistability using a sodium-filled fabry-perot interferometer"*, Physical Review Letters*, **36** (19), 1135-1138, 1976.

147. H.M. Gibbs, S.L. McCall, T.N.C. Venkatesan, A.C. Gossard, A. Passner and W. Wiegmann, "Optical bistability in semiconductors"*, Applied Physics Letters*, **35** (6), 451-453, 1979.

148. J.A. Goldstone and E. Garmire, "Intrinsic optical bistability in nonlinear media"*, Physical Review Letters*, **53** (9), 910-913, 1984.

149. T. Tanabe, M. Notomi, S. Mitsugi, A. Shinya and E. Kuramochi, "Fast bistable all-optical switch and memory on a silicon photonic crystal on-chip", *Optics Letters*, **30** (19), 2575-2577, 2005.

150. E. Weidner, S. Combrié, A.d. Rossi, N.-V.-Q. Tran and S. Cassette, "Nonlinear and bistable behavior of an ultrahigh-q GaAs photonic crystal nanocavity", *Applied Physics Letters*, **90** (10), 101118, 2007.

151. L.-D. Haret, T. Tanabe, E. Kuramochi and M. Notomi, "Extremely low power optical bistability in silicon demonstrated using 1D photonic crystal nanocavity", *Optics Express*, **17** (23), 21108-21117, 2009.

152. V.R. Almeida and M. Lipson, "Optical bistability on a silicon chip", *Optics Letters*, **29** (20), 2387-2389, 2004.

153. P. Sun and R.M. Reano, "Low-power optical bistability in a free-standing silicon ring resonator", *Optics Letters*, **35** (8), 1124-1126, 2010.

154. Y.F. Yu, J.B. Zhang, T. Bourouina and A.Q. Liu, "Optical-force-induced bistability in nanomachined ring resonator systems", *Applied Physics Letters*, **100** (9), 093108, 2012.

155. G. Pobegalov, P. Agruzov, I. Ilichev and A. Shamray, "Low-power optical bistability and hysteresis in the laser system with absorbing nanosuspension", *Optics Letters*, **39** (9), 2819-2822, 2014.

156. B. Wang, J. Zhou, T. Koschny and C.M. Soukoulis, "Nonlinear properties of split-ring resonators", *Optics Express*, **16** (20), 16058-16063, 2008.

157. I.V. Shadrivov, V.A. Fedotov, D.A. Powell, Y.S. Kivshar and N.I. Zheludev, "Electromagnetic wave analogue of an electronic diode", *New Journal of Physics*, **13** (3), 033025, 2011.

158. Y. Ding, C. Xue, Y. Sun, H. Jiang, Y. Li, H. Li and H. Chen, "Subwavelength electromagnetic switch: Bistable wave transmission of side-coupling nonlinear meta-atom", *Optics Express*, **20** (22), 24813-24818, 2012.

159. H. Wu, J. Zhou, C. Lan, Y. Guo and K. Bi, "Microwave memristive-like nonlinearity in a dielectric metamaterial", *Scientific Reports*, **4** (1), 5499, 2014.

160. T. Rueckes, K. Kim, E. Joselevich, G.Y. Tseng, C.-L. Cheung and C.M. Lieber, "Carbon nanotube-based nonvolatile random access memory for molecular computing", *Science*, **289** (5476), 94, 2000.

161. R.L. Badzey, G. Zolfagharkhani, A. Gaidarzhy and P. Mohanty, "A controllable nanomechanical memory element", *Applied Physics Letters*, **85** (16), 3587-3589, 2004.

162. I. Mahboob and H. Yamaguchi, "Bit storage and bit flip operations in an electromechanical oscillator", *Nature Nanotechnology*, **3** (5), 275-279, 2008.

163. B. Charlot, W. Sun, K. Yamashita, H. Fujita and H. Toshiyoshi, "Bistable nanowire for micromechanical memory", *Journal of Micromechanics and Microengineering*, **18** (4), 045005, 2008.

164. D. Roodenburg, J.W. Spronck, H.S.J. van der Zant and W.J. Venstra, "Buckling beam micromechanical memory with on-chip readout", *Applied Physics Letters*, **94** (18), 183501, 2009.

165. W.J. Venstra, H.J.R. Westra and H.S.J. van der Zant, "Mechanical stiffening, bistability, and bit operations in a microcantilever", *Applied Physics Letters*, **97** (19), 193107, 2010.

166. H. Noh, S.-B. Shim, M. Jung, Z.G. Khim and J. Kim, "A mechanical memory with a dc modulation of nonlinear resonance"*, Applied Physics Letters*, **97** (3), 033116, 2010.

167. V. Intaraprasonk and S. Fan, "Nonvolatile bistable all-optical switch from mechanical buckling"*, Applied Physics Letters*, **98** (24), 241104, 2011.

168. A. Uranga, J. Verd, E. Marigó, J. Giner, J.L. Muñóz-Gamarra and N. Barniol, "Exploitation of non-linearities in CMOS-NEMS electrostatic resonators for mechanical memories"*, Sensors and Actuators A: Physical*, **197**, 88-95, 2013.

169. H. Xu, U. Kemiktarak, J. Fan, S. Ragole, J. Lawall and J.M. Taylor, "Observation of optomechanical buckling transitions"*, Nature Communications*, **8** (1), 14481, 2017.

170. S. Savel'ev, X. Hu and F. Nori, "Quantum electromechanics: Qubits from buckling nanobars"*, New Journal of Physics*, **8** (6), 105-105, 2006.

171. S.O. Erbil, U. Hatipoglu, C. Yanik, M. Ghavami, A.B. Ari, M. Yuksel and M.S. Hanay, "Full electrostatic control of nanomechanical buckling"*, Physical Review Letters*, **124** (4), 046101, 2020.

172. R. Lifshitz and M.C. Cross, *Nonlinear dynamics of nanomechanical and micromechanical resonators*, in *Reviews of nonlinear dynamics and complexity*. 2008, Wiley. p. 1-52.

173. A.H. Nayfeh and D.T. Mook, *Nonlinear oscillations*. 1995, New York: Wiley.

174. L.L. Li, P.M. Polunin, S. Dou, O. Shoshani, B. Scott Strachan, J.S. Jensen, S.W. Shaw and K.L. Turner, "Tailoring the nonlinear response of MEMS resonators using shape optimization"*, Applied Physics Letters*, **110** (8), 081902, 2017.

175. A. Jöckel, M.T. Rakher, M. Korppi, S. Camerer, D. Hunger, M. Mader and P. Treutlein, "Spectroscopy of mechanical dissipation in micro-mechanical membranes"*, Applied Physics Letters*, **99** (14), 143109, 2011.

176. S. Wu, J. Sheng, X. Zhang, Y. Wu and H. Wu, "Parametric excitation of a SiN membrane via piezoelectricity"*, AIP Advances*, **8** (1), 015209, 2018.

177. S.S.P. Nathamgari, S. Dong, L. Medina, N. Moldovan, D. Rosenmann, R. Divan, D. Lopez, L.J. Lauhon and H.D. Espinosa, "Nonlinear mode coupling and one-to-one internal resonances in a monolayer WS_2 nanoresonator"*, Nano Letters*, **19** (6), 4052-4059, 2019.

178. Q. Xu and M. Lipson, "Carrier-induced optical bistability in silicon ring resonators"*, Optics Letters*, **31** (3), 341-343, 2006.

179. Q. Xu and M. Lipson, "All-optical logic based on silicon micro-ring resonators"*, Optics Express*, **15** (3), 924-929, 2007.

180. H. Cai, B. Dong, J.F. Tao, L. Ding, J.M. Tsai, G.Q. Lo, A.Q. Liu and D.L. Kwong, "A nanoelectromechanical systems optical switch driven by optical gradient force"*, Applied Physics Letters*, **102** (2), 023103, 2013.

181. B.M. Zwickl, W.E. Shanks, A.M. Jayich, C. Yang, A.C. Bleszynski Jayich, J.D. Thompson and J.G.E. Harris, "High quality mechanical and optical properties of commercial silicon nitride membranes"*, Applied Physics Letters*, **92** (10), 103125, 2008.

182. I. Mahboob, N. Perrissin, K. Nishiguchi, D. Hatanaka, Y. Okazaki, A. Fujiwara and H. Yamaguchi, "Dispersive and dissipative coupling in a micromechanical resonator embedded with a nanomechanical resonator"*, Nano Letters*, **15** (4), 2312-2317, 2015.

183. A.C. Poveda, D.D. Bühler, A.C. Sáez, P. V. Santos and M. M. de Lima Jr, "Semiconductor optical waveguide devices modulated by surface acoustic waves", *J. Phys. D: Appl. Phys.*, **52,** 253001, 2019.

184. M.V. Gustafsson, T. Aref, A.F. Kockum, M.K. Ekström, G. Johansson and P. Delsing, "Propagating phonons coupled to an artificial atom", *Science*, **346**, (6206), 207-211, 2014.

185. L. Raguin, O. Gaiffe, R. Salut, J.-M. Cote, V. Soumann, V. Laude, A. Khelif and S. Benchabane, "Dipole states and coherent interaction in surface-acoustic-wave coupled phononic resonators", *Nature Communications*, **10** (1), 4583, 2019.

186. S. Benchabane, R. Salut, O. Gaiffe, V. Soumann, M. Addouche, V. Laude, and A. Khelif, "Surface-wave coupling to single phononic subwavelength resonators", *Physical Review Applied,* **8**, 034016, 2017.

187. N. Bassim, K. Scott and L.A. Giannuzzi, "Recent advances in focused ion beam technology and applications", *MRS Bulletin*, **39** (4), 317-325, 2014.

188. http://www.microspectra.com